A Measurement of the τ Leptonic Branching Ratios at BaBar

Paul Stephen McGrath

Royal Holloway, University of London

September 2001

A thesis submitted in accordance with the regulations for the degree of Doctor of Philosophy in the University of London.

Abstract

A preliminary measurement of the τ leptonic branching ratios is presented from an analysis of data taken in 2000 by the BaBar experiment. A sample of 38027 τ pair events has been selected from the data through partial reconstruction of the $\tau \to \rho\nu_\tau$ channel and the branching ratios obtained are: $\mathcal{B}(\tau \to e\nu_e\nu_\tau)$ = 17.1 $\pm$ 0.2 (stat) $\pm$ 0.6 (syst) (%) and $\mathcal{B}(\tau \to \mu\nu_\mu\nu_\tau)$ = 18.3 $\pm$ 0.3 (stat) $\pm$ 0.9 (syst) (%). The potential of the BaBar experiment to make competitive measurements of the τ leptonic branching ratios is demonstrated. The systematic limitations to the measurements presented are described, and suggestions for improving on the precision are made.

An account of online software enabling operation of the calorimeter trigger within the context of the BaBar core data acquisition software is presented. Object oriented techniques have been used in the software design. The software implementation for an example diagnostics run for the calorimeter trigger is described to demonstrate the application of these techniques.

Contents

1 Introduction **14**

1.1 The Standard Model 14

1.2 The τ Lepton 16

1.2.1 Leptonic τ Decays 17

1.2.2 Lepton Universality 19

1.3 τ Physics at BaBar 19

1.4 Thesis Outline 21

2 The BaBar Experiment **22**

2.1 Introduction 22

2.2 The PEPII Asymmetric Storage Ring 22

2.3 The BaBar Detector 23

2.3.1 The Silicon Vertex Tracker 23

2.3.2 The Drift Chamber 27

2.3.3 The Detector of Internally Reflecting Cherenkov Light (DIRC) 28

2.3.4 The Electromagnetic Calorimeter 32

2.3.5 The Solenoidal Magnetic Field 34

2.3.6 The Instrumented Flux Return 34

2.3.7 The Trigger System 35

3 Online Software for the Calorimeter Trigger 39

3.1 Introduction 39

3.2 Object Oriented Software Design 39

3.2.1 Structure of Object Oriented Software 40

3.2.2 Concepts and Terminology 40

3.3 The BaBar Data Acquisition Software 41

3.3.1 The Finite State Machine Model 42

3.3.2 Data Transportation 42

3.4 Software for the Calorimeter Trigger 44

3.4.1 Common Transition Classes 44

3.4.2 Frameclash Test Software 46

3.4.2.1 Frameclash Definition 47

3.4.2.2 Frameclash Test 49

4 Selection of $\tau^+\tau^-$ Events 54

4.1 Introduction 54

4.2 Event Tagging Using the $\tau \to \rho\nu_\tau$ Channel 54

4.3 Event Selection 56

4.3.1 Background Rejection 56

4.3.1.1 Discriminating against Bhabha Events 57

4.3.1.2 Discriminating against Continuum Events 66

4.3.2 π^0 Reconstruction 70

4.3.2.1 π^0 Reconstruction Efficiency 73

4.3.3 ρ Reconstruction 76

4.4 Performance of Event Selection Method 79

4.4.1 Efficiency for Selection of $\tau \to \rho\nu_\tau$ Events 79

4.4.2 Bias to the τ Sample 81

4.4.3 Check of Background Contamination to the τ Sample 82

5 Measurement of the τ Leptonic Branching Ratios 87

5.1 Introduction 87

5.2 Lepton Identification 87

5.3 Performance of Lepton Identification 89

5.3.1 Lepton Selection Efficiency 89

5.3.1.1 Electron Identification Efficiency 90

5.3.1.2 Muon Identification Efficiency 91

5.3.2 Background Contamination in the Lepton Sample 92

5.4 Extraction of Leptonic Branching Ratios 93

5.4.1 Estimation of Statistical and Systematic Errors 96

5.4.2 Comparison of Experimental Results 97

5.5 Lepton Universality 98

6 Conclusions 100

6.1 Introduction 100

6.2 Online Software for the Calorimeter Trigger 100

6.3 Analysis of τ Decays 101

6.3.1 Improving on the Precision 102

A Branching Fractions of the τ Lepton **109**

B Class Diagrams **110**

List of Figures

1-1 Feynman Diagram describing the charged weak interaction process for leptonic τ decay. 17

1-2 Feynman Diagram describing the τ pair production process at BaBar. . . 20

2-1 Cut-away view of the BaBar detector showing locations of individual sub-detectors. 1. Silicon Vertex Tracker, 2. Drift Chamber, 3. Detector of Internally Reflecting Cherenkov, 4. Electromagnetic Calorimeter, 5. Magnet, 6. Instrumented Flux Return. 24

2-2 Cut-away view of the BaBar Silicon Vertex Tracker 25

2-3 Measured z and ϕ hit resolutions in the inner layer of the Silicon Vertex Tracker as a function of incident track angle from data events (blue) and from simulated events (red). 26

2-4 Axial view of the BaBar Drift Chamber. Dimensions are in mm. 28

2-5 Drift chamber cell spatial resolution as a function of distance measured using charged tracks from BaBar data. 29

2-6 Cross sectional view of the Detector of Internally Reflecting Cherenkov Light (DIRC) showing the path of emitted Cherenkov photons. 30

2-7 Kaon and pion selection efficiency in the DIRC from data events as a function of track momentum. 31

2-8 Cross-sectional view of the crystal layout in the BaBar Electromagnetic Calorimeter showing dimensions. 33

2-9 Schematic of the BaBar Instrumented Flux Return showing the barrel section and forward and backward endcaps. 35

2-10 Structure of the BaBar Trigger System showing path for event data. . . . 37

3-1 States of the data acquisition software Finite State Machine modelling the different stages in the operation of the BaBar detector. Arrows represent transitions between states. 43

3-2 Relationship of classes written to implement the initial Finite State Machine transitions for the calorimeter trigger. 45

3-3 Schematic of the hardware logic used for synchronisation of calorimeter tower energy sum data in the calorimeer trigger. The example shown is for a single cable. 48

3-4 Schematic of data carried on a cable from the calorimeter to the Calorimeter Trigger. The example shows 3 tower energy sum 16-bit data words and the frame bit which indicates the start of the tower energy sum data. . . . 49

3-5 Relationship of classes written to implement the accumulation of cable error data for the calorimeter trigger frameclash test. 50

3-6 Summary of frameclash positions on all calorimeter trigger input cables determined from the frameclash test software. Possible problem cables are indicated by shorter dark shaded regions. 51

3-7 Errors accumulated on calorimeter trigger input cables as a function of the time delay of the incoming frame bit on the cable from the calorimeter. The large spike in each histogram indicates the frameclash position. . . . 53

4-1 Feynman Diagram describing the charged weak interaction process for the $\tau \to \rho\nu_\tau$ decay channel. 55

4-2 E/p distributions for the charged track in the tagging hemisphere from (a) simulated τ pair events in which the τ in the tagging hemisphere decays via $\tau \to \rho\nu_\tau$ and (b) simulated Bhabha events. 58

4-3 E/p distributions for the charged track in the tagging hemisphere from (a) simulated continuum ($u\overline{u}, d\overline{d}, s\overline{s}$) events, (b) simulated continuum $c\overline{c}$ events, (c) simulated μ pair events, and (d) data events. 59

4-4 dE/dx distributions for the charged track in the tagging hemisphere measured in the drift chamber from simulated τ pair events in which the τ in the tagging hemisphere decays via $\tau \to \rho\nu_\tau$ and from simulated Bhabha events. 61

4-5 Momentum distributions of the reconstructed ρ candidate in the centre of mass for (a) true ρs from simulated τ pair events and (b) simulated Bhabha events. 62

4-6 Momentum distribution of the reconstructed ρ candidate in the centre of mass as a function of the polar angle of the charged track used in the ρ reconstruction from simulated Bhabha events. 63

4-7 Fraction of $\tau \to \rho\nu_\tau$ events retained after cutting on the centre of mass momentum of the reconstructed ρ candidate against the fraction of Bhabha events rejected for different track polar angle cuts. 63

4-8 Momentum distributions of the reconstructed ρ candidate in the centre of mass for simulated (a) continuum ($u\overline{u}, d\overline{d}, s\overline{s}$) events, (b) continuum $c\overline{c}$ events, and (c) μ pair events. 65

4-9 Fraction of $\tau \to \rho\nu_\tau$ events retained against the fraction of Bhabha events rejected for different cut values of discriminating variables studied for the rejection of Bhabha events. Cuts which have been applied in the analysis are highlighted. 66

4-10 Momentum distribution of the reconstructed ρ candidate in the centre of mass as a function of E/p for the charged track in the tagging hemisphere from simulated τ pair events (black) and from simulated Bhabha events (blue). 67

4-11 Invariant mass distributions for the hemisphere opposite the hemisphere used to tag the event from simulated (a) τ pair events, (b) continuum ($u\overline{u}, d\overline{d}, s\overline{s}$) events, and (c) continuum $c\overline{c}$ events. 68

4-12 Fraction of $\tau \to \rho\nu_\tau$ events retained against the fraction of continuum events rejected for different cut values of the invariant mass of the hemisphere opposite to the hemisphere used to tag the event. 69

4-13 Fraction of $\tau \to \rho\nu_\tau$ events retained against the fraction of continuum events rejected for cones of different half angles inside the tagging hemisphere. A cut of m $< 2\text{GeV}/c^2$ is applied to the opposite hemisphere. . . . 70

4-14 Momentum spectrum of π^0s produced in the $\tau \to \rho\nu_\tau$ decay channel from simulated generic τ pair events. 71

4-15 Opening angle of photons produced in the decay $\pi^0 \to \gamma\gamma$ for π^0s produced in $\tau \to \rho\nu_\tau$ decays as a function of π^0 momentum. The dashed line indicates the momentum above which the photons may produce merged clusters in the calorimeter. 72

4-16 Invariant mass distribution of neutral calorimeter clusters in the tagging hemisphere from data (points) and from simulated events (histogram). The shaded regions indicate different background contributions. 74

4-17 Invariant mass distribution of reconstructed ρ candidates in the tagging hemisphere from data events (points) and from simulated events (histogram). The shaded regions indicate different background contributions predicted from simulated events. The data is not well modelled by the simulation on the low mass side of the peak. 77

4-18 Momentum distribution in the centre of mass of reconstructed ρ candidates from data events. The dashed line indicates ρ candidates in the low mass region ($M_\rho < 0.5$ GeV/c^2) of figure 4-17. The distributions show a peak below about 1.5 GeV/c which is not seen in the simulated event samples. 79

4-19 Invariant mass distribution of reconstructed ρ candidates in the tagging hemisphere from data events (points) and from simulated events (histogram). The shaded regions indicate different background contributions predicted from simulated events. The simulation is in good agreement with the data. 80

4-20 Momentum distribution of reconstructed ρ candidates in the centre of mass from the enhanced sample of Bhabha events in the data after background subtraction (histogram) and from simulated Bhabha events with corrected normalisation (points). 84

B-1 Class diagram illustrating the ‘inheritance’ and ‘use’ relationships. 110

List of Tables

1-1 The gauge bosons of the Standard Model. 14

1-2 The quark flavours of the Standard Model. Quarks do not exist as free particles. Measurements of quark masses must therefore be made indirectly and are model dependent. A review of different models used to define quark masses may be found here [5]. 15

1-3 The leptons of the Standard Model. 15

4-1 Summary of signal π^0 efficiency for selection cuts. 75

4-2 Summary of efficiency for selection of $\tau \to \rho\nu_\tau$ events. 81

4-3 Applied cuts for selecting background enhanced samples of data events. . 83

4-4 Background fractions of different physics processes in the sample of data events passing the event selection predicted from simulated event samples. 86

5-1 Comparison of the electron identification efficiency measured from different samples of electrons with p $<$ 4.0 GeV/c in the data and from $\tau \to e\nu_e\nu_\tau$ decays in simulated τ pair events. 91

5-2 Background fractions remaining in the sample of data events passing the lepton identification predicted from simulated event samples. 93

5-3 Contributions to the absolute systematic error of the measured τ leptonic branching ratios. 97

5-4 Recent measurements of the τ leptonic branching ratios 98

5-5 Recent measurements of g_μ/g_e from measurements of the τ leptonic branching ratios. 99

6-1 Contributions to the absolute systematic error of the measured τ leptonic branching ratios (reproduced from table 5-3). 103

A-1 Branching fractions of the τ lepton. 109

A-2 Topological branching fractions of the τ lepton. 109

Acknowledgments

I would of course like to thank my supervisor, Mike Green, for his help and advice on all aspects of my work over the last few years.

Working on the BaBar experiment during the exciting period leading up to and beyond first data taking has been a great experience and I would like to thank Glen Cowan, Paul Dauncey, and Paul Harrison for their guidance and assistance at different times during my PhD studies. The experience was made all the more enjoyable by the friends and colleagues both at Royal Holloway and at SLAC who were there with me. Thanks particularly to Iain Scott, James Weatherall, and Dan Smith who helped me in the early days. Thanks also to Naveen Gunawardane, Dan Azzopardi, Mark Williams, Ajit Kurup, Pedro Vidal, Jason McFall, Pete Sanders, John Back, Michael George, Phil Clark, Jane Tinslay, Simon George, and Fabrizio Salvatore. A few others to mention outside of HEP: Derek Charles of course and, Rob, James, Bob, Kadir, Cedric, Hetal, and Anthony for the entertainment.

I acknowledge the financial support of PPARC while at Royal Holloway and at SLAC, without which my PhD studies would not have been possible.

I would like to thank my family and particularly my parents for all their support throughout my time at university. Finally, thanks to Helen for your unconditional support and encouragement.

1

Introduction

1.1 The Standard Model

The Standard Model describes our current knowledge of fundamental particles and their interactions. Particle interactions mediated by the exchange of gauge bosons give rise to the fundamental forces of nature. There are four fundamental forces known as strong nuclear, electromagnetic, weak nuclear, and gravity. Gravity is not included in the Standard Model and its gauge boson, assumed to be the graviton, has yet to be discovered. A summary of the mediating gauge bosons of the Standard Model used to describe the fundamental forces is given in table 1-1.

Gauge Boson	**Force**	**Mass**
Gluon (g)	Strong	0
Photon (γ)	Electromagnetic	0
$W^{\pm}$	Weak	M_W = 80.4 GeV/c^2
Z	Weak	M_Z = 91.2 GeV/c^2

Table 1-1. *The gauge bosons of the Standard Model.*

Particles which interact via the strong interaction are known as hadrons. The fundamental particles of which they are composed are the quarks. The quarks of the Standard Model are listed in table 1-2. The six types or flavours of quark fall into three generations with each generation containing one quark of positive charge and one quark of negative charge. Each quark may carry one of three colour charges, red, green, or blue. In addition

Quark Generation	Quark	Electric Charge	Mass
1st	d	-1/3	3 - 9 MeV/c^2
	u	2/3	1 - 5 MeV/c^2
2nd	s	-1/3	75 - 170 MeV/c^2
	c	2/3	1.15 - 1.35 GeVc^2
3rd	b	-1/3	4.0 - 4.4 GeV/c^2
	t	2/3	174.3 $\pm$ 5.1 GeV/c^2

Table 1-2. *The quark flavours of the Standard Model. Quarks do not exist as free particles. Measurements of quark masses must therefore be made indirectly and are model dependent. A review of different models used to define quark masses may be found here [5].*

there exists an antiquark for each quark which carries opposite charge and colour. The interactions between quarks (producing the strong nuclear force) are charge independent and mediated by the exchange of massless gluons between colour charges carried by the quarks.

The elementary particles which do not take part in strong interactions are the leptons. The leptons of the Standard Model are listed in table 1-3. Like the quarks, there are three generations of leptons. Each generation consists of a charged and a neutral lepton and has its own lepton number which is conserved in particle interactions. Apart from the

Lepton Generation	Lepton	Electric Charge	Mass	Lepton No.		
				l_e	l_μ	l_τ
1st	e	-1	0.511 MeV/c^2	1	0	0
	ν_e	0	< 3 eV/c^2	1	0	0
2nd	μ	-1	105.7 MeV/c^2	0	1	0
	ν_μ	0	< 0.19 MeV/c^2	0	1	0
3rd	τ	-1	1778. MeV/c^2	0	0	1
	ν_τ	0	< 18.2 MeV/c^2	0	0	1

Table 1-3. *The leptons of the Standard Model.*

assigned lepton number, the 2nd and 3rd generations are thought to be replicas of the 1st

generation and are only distinguished by the different masses of the charged leptons. The reason why there are 3 generations with different masses is not known. Each lepton has its own antiparticle, which carries opposite charge and lepton number. In contrast to the strong and electromagnetic forces the weak interaction is mediated by the heavy W and Z exchange bosons.

The Standard Model has been extensively tested experimentally and so far has been very successful. One of the few aspects which has yet to be validated experimentally is the predicted existence of the Higgs particle. This particle is required by the Higgs mechanism [1] which allows the existence of massive exchange bosons. The Higgs is widely expected to be discovered. Evidence of its existence may already have been found by the LEP experiments [2, 3]. Its discovery would provide further evidence in support of the Standard Model. Experimental searches for new particles and increased precision in the measurement of the properties of known particles provide ever more stringent tests of the Standard Model.

1.2 The τ Lepton

The τ is the heaviest and most recently discovered [4] lepton of the Standard Model. It is a short lived, unstable particle and has many decay modes due to its large mass of ~ 1.78 GeV/c^2 [5]. The decays of the τ lepton provide an opportunity to investigate weak interactions and test the Standard Model. In this thesis a study of the τ leptonic decay modes is presented. τ decays are well described theoretically by weak interaction theory and detailed descriptions may be found elsewhere [6, 7].

1.2.1 Leptonic τ Decays

τ leptons decay via the charged weak interaction process $\tau \rightarrow \nu_\tau + W$. The virtual W boson can subsequently decay into either a lepton pair, or a quark pair producing hadrons. The τ leptonic decay modes, $\tau \rightarrow e\nu_e\nu_\tau$ and $\tau \rightarrow \mu\nu_\mu\nu_\tau$, make up over a third of all τ decays (major τ branching fractions are listed in Appendix A). The Feynman diagram describing the weak interaction process for the leptonic τ decay modes is shown in figure 1-1.

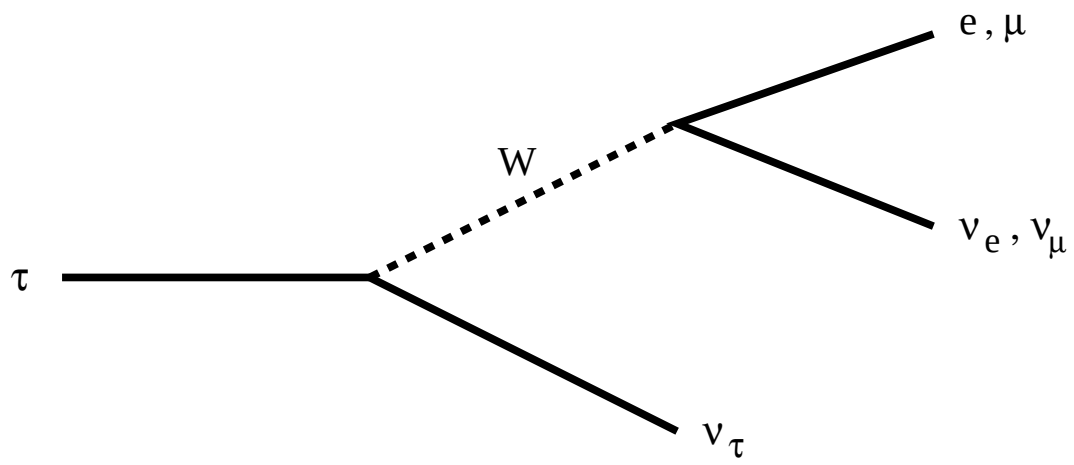

Figure 1-1. *Feynman Diagram describing the charged weak interaction process for leptonic τ decay.*

The total decay rate of the τ, Γ_{Tot}, is the sum of the partial decay rates to the individual decay modes:

$$\Gamma_{Tot} = \sum_i \Gamma_i. \tag{1.1}$$

The decay rate to any given mode as a fraction of the total decay rate gives the branching ratio for that mode. For the leptonic modes:

$$\mathcal{B}(\tau \to l\nu_l\nu_\tau) = \frac{\Gamma(\tau \to l\nu_l\nu_\tau)}{\Gamma_{Tot}}. \tag{1.2}$$

Theoretically, the decay rate for leptonic τ decay is given by [8]:

$$\Gamma(\tau \to l\nu_l\nu_\tau) = \frac{G_l^2 m_\tau^5}{192\pi^3} f\left(\frac{m_l^2}{m_\tau^2}\right) F_W \left[1 + \frac{\alpha(m_\tau)}{2\pi}\left(\frac{25}{4} - \pi^2\right)\right] \tag{1.3}$$

where $f\left(\frac{m_l^2}{m_\tau^2}\right) = 1 - 8\left(\frac{m_l^2}{m_\tau^2}\right) + 8\left(\frac{m_l^2}{m_\tau^2}\right)^3 + \left(\frac{m_l^2}{m_\tau^2}\right)^4 - 12\left(\frac{m_l^2}{m_\tau^2}\right)^2 ln\left(\frac{m_l^2}{m_\tau^2}\right)$

and $F_W = 1 + \frac{3}{5}\frac{m_\tau^2}{m_W^2}$.

The first term in equation (1.3) contains the strength of the interaction represented by the decay constant G_l given by

$$G_l^2 = \frac{g_l^2 g_\tau^2}{32 m_W^4} \tag{1.4}$$

where g_l and g_τ are the lepton couplings to the W, and m_W is the mass of the W boson. A derivation of the first term in equation (1.3) may be found in [9]. The remaining terms contain the following corrections to the decay rate. f(m_l^2/m_τ^2) is a correction for the non zero mass of the lepton in the final state [10] and has the values $f(m_l^2/m_\tau^2)$ = 1 for the $\tau \to e\nu_e\nu_\tau$ mode, and $f(m_l^2/m_\tau^2)$ = 0.973 for the $\tau \to \mu\nu_\mu\nu_\tau$ mode. F_W is a correction for the finite mass of the W and has the value F_W = 1.0003. The final term [8] takes into account radiative corrections for the emission of virtual photons and for real radiative decays so that the decay rate in equation (1.3) includes leptonic modes with additional real photons or electron-positron pairs, $\tau \to l\nu\nu\gamma$, $\tau \to l\nu\nu ee$.

The branching fractions to the leptonic modes have been measured experimentally with high precision. A review of recent measurements of the τ leptonic branching ratios is given in section 5.4.2 of chapter 5.

1.2.2 Lepton Universality

Lepton universality is a key component of the Standard Model. It describes the equality of the lepton couplings to the weak force. Measurements of lepton universality therefore provide a test of the Standard Model. The ratio of the τ leptonic decay rates may be used to compare the electron and muon weak couplings. From equation (1.3):

$$\frac{\Gamma(\tau \to \mu\nu_\mu\nu_\tau)}{\Gamma(\tau \to e\nu_e\nu_\tau)} = \frac{g_\mu^2}{g_e^2}\left[\frac{f\left(\frac{m_\mu^2}{m_\tau^2}\right)}{f\left(\frac{m_e^2}{m_\tau^2}\right)}\right]. \tag{1.5}$$

In the case of e-μ lepton universality, g_μ/g_e = 1 and the above ratio has the value 0.973. Experimentally, e-μ universality has been verified at the 3 per mille level from measurements of the τ leptonic branching ratios [11]. A review of recent measurements of the ratio g_μ/g_e is given in section 5.5 of chapter 5.

1.3 τ Physics at BaBar

The BaBar experiment has been designed for the study of CP violation[1] in B meson decays and has recently published the first evidence that CP violation has been observed in the B meson system [14]. However, it is also a very good tool for the study of τ physics. τ lepton pairs can be produced in e^+e^- collisions which have energy in the centre of mass greater than twice the mass of the τ, about 3.55 GeV/c^2. The BaBar centre of mass energy is 10.58GeV/c^2, well above the threshold for τ pair production. At this energy, $\tau^+\tau^-$ pairs are produced through the electromagnetic process $e^+e^- \to \tau^+\tau^-$ mediated by the exchange of a virtual photon. The Feynman diagram for this process is shown in figure 1-2.

[1] An introduction to CP violation can be found in many physics texts, for example [12]. A more detailed review may be found in [13].

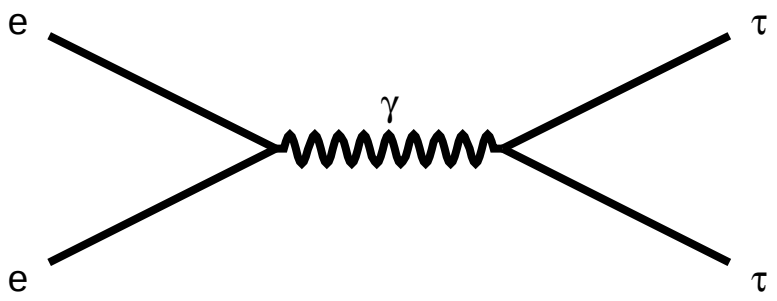

Figure 1-2. *Feynman Diagram describing the τ pair production process at BaBar.*

The BaBar centre of mass energy has been specifically chosen to optimise the production of B meson pairs. At this energy the cross section for $\tau^+\tau^-$ pair production within the acceptance of the BaBar detector is about 0.94nb compared to 1.05nb [15] for the production of B pairs. In addition, BaBar is a high luminosity experiment and has already produced a data sample of $20 fb^{-1}$ integrated luminosity which contains about 19×10^6 τ pairs. This already exceeds the τ pair samples obtained by the established LEP and CLEO experiments. Of these, CLEO has by far the largest sample of τs with $\sim 3 \times 10^6$ τ pairs. The expectation is that BaBar will produce $\sim 30 \times 10^6$ τ pairs each year. With this large data sample, the precision of many measurements such as the branching ratios of the τ are likely to be dominated by systematics rather than statistics.

The short lifetime of the τ means that τs produced at BaBar decay so close to their production point that they do not reach the innermost BaBar subdetector. Many of the particles produced in the τ decay can however be directly detected as they traverse the detector. The identification of τ decays in the BaBar detector is the focus of chapters 4 and 5 of this thesis. Precise vertex information may be used to measure the τ decay length and lifetime. Preliminary measurements of these properties have been made at BaBar and are described elsewhere [16, 17].

1.4 Thesis Outline

The overview presented in this chapter provides the background material to chapters 4, and 5 which form the major part of this thesis. These chapters present a preliminary measurement of the leptonic branching ratios of the τ lepton from an analysis of data from the BaBar experiment. The primary motivation in making this measurement has been to demonstrate the potential of BaBar and to highlight the current systematic limitations. The measurement is based on a data sample of $0.6 fb^{-1}$ integrated luminosity. This is only a small fraction of the total BaBar data set, but the dominance of systematic errors on this measurement, discussed in chapters 4 to 6, means that a larger data sample would not improve the precision achieved. It is expected that future analyses will be able to improve on the precision presented here as greater control of systematics is obtained.

A description of the BaBar detector is given in chapter 2. Each of the main components is described and its performance summarised. Any figures or quoted results relating to performance of detector components presented in this chapter are those officially approved by the BaBar experiment and I had no involvement in their production. My participation in the BaBar experiment is described from chapter 3 onwards. Chapter 3 is a self-contained account of software written for the calorimeter trigger, an essential component of the BaBar detector. Emphasis is placed on the application of object-oriented techniques in the software design. The major roles of the software are described and examples of results are given. The analysis of data is described over two chapters. Chapter 4 describes the techniques used for the selection of τ events from the data. Chapter 5 describes the identification of leptonic decays in the selected sample of τ events. The results presented in chapters 4 and 5 are used to extract the τ leptonic branching ratio measurements. In the final chapter, the main results presented in this thesis are summarised and concluding remarks are made.

2

The BaBar Experiment

2.1 Introduction

The BaBar detector has been taking data at the PEPII asymmetric storage ring at SLAC since May 1999. The primary aim of the BaBar experiment is the study of CP violation in the neutral B meson system. This requires the analysis of rare decay modes making it necessary to produce B mesons on a large scale. A brief description of PEPII will be given in this chapter followed by a summary of the BaBar detector. The component devices of the BaBar detector are each described and their performance summarised.

2.2 The PEPII Asymmetric Storage Ring

PEPII is an e^+e^- storage ring into which beams of 9 GeV electrons and 3.1 GeV positrons are injected from the SLAC linear accelerator. PEPII has been designed to produce the large numbers of B and $\overline{B}$ mesons required by the BaBar experiment for CP analyses. To achieve this, PEPII operates at a centre of mass energy of 10.58GeV/c^2, the Υ(4S) resonance, a bound state of a b and $\overline{b}$ quark which nearly always decays to B meson pairs. In addition, PEPII is designed to be a high luminosity collider, reaching a luminosity of $3 \times 10^{33} cm^{-2} s^{-1}$. This luminosity has already been achieved and the integrated luminosity recorded by BaBar in its first year of running was $20.7 fb^{-1}$. Increases in peak luminosity to $5 \times 10^{33} cm^{-2} s^{-1}$ are expected during 2001. In excess of 30 million Υ(4S)

per year will be produced. The asymmetry of the beam energies is also designed for CP violation studies. The unequal beams provide a boost $\beta\gamma$ of 0.56 in the laboratory frame enabling the decay length and hence the decay time of the B mesons to be determined. The difference in beam energies means that the electron and positron beams require separate rings. The beams are brought into head on collision at the location of the BaBar experiment with only 4.2ns between crossings.

2.3 The BaBar Detector

The BaBar detector is described in detail elsewhere [15, 19]. In this section only a summary of the component sub-detector devices will be given. The cut-away view of the BaBar detector in figure 2-1 shows the location of the individual sub-detectors. These are from the inside out; the Silicon Vertex Tracker, the Drift Chamber, the Detector of Internally Reflecting Cherenkov, the Electromagnetic Calorimeter, and the Instrumented Flux Return. In order to achieve the best possible acceptance with the asymmetric e^+e^- beams, the detector is positioned with the interaction point nearer the backward end of the detector to provide more coverage in the forward (boost) direction.

2.3.1 The Silicon Vertex Tracker

A measurement of CP violation in the decay of the two B mesons requires a measurement of the time between each B decay. The purpose of the Silicon Vertex Tracker is primarily to provide position information on the two B decay vertices from which the decay times may be derived. For the extraction of CP asymmetries, the separation of the decay vertices in the z direction must be measured with a resolution of less than half the mean separation of $\sim 250\mu m$ [20]. The position resolution for each B decay vertex needs to be less than around 80μm to measure the separation of the decay vertices with the accuracy required.

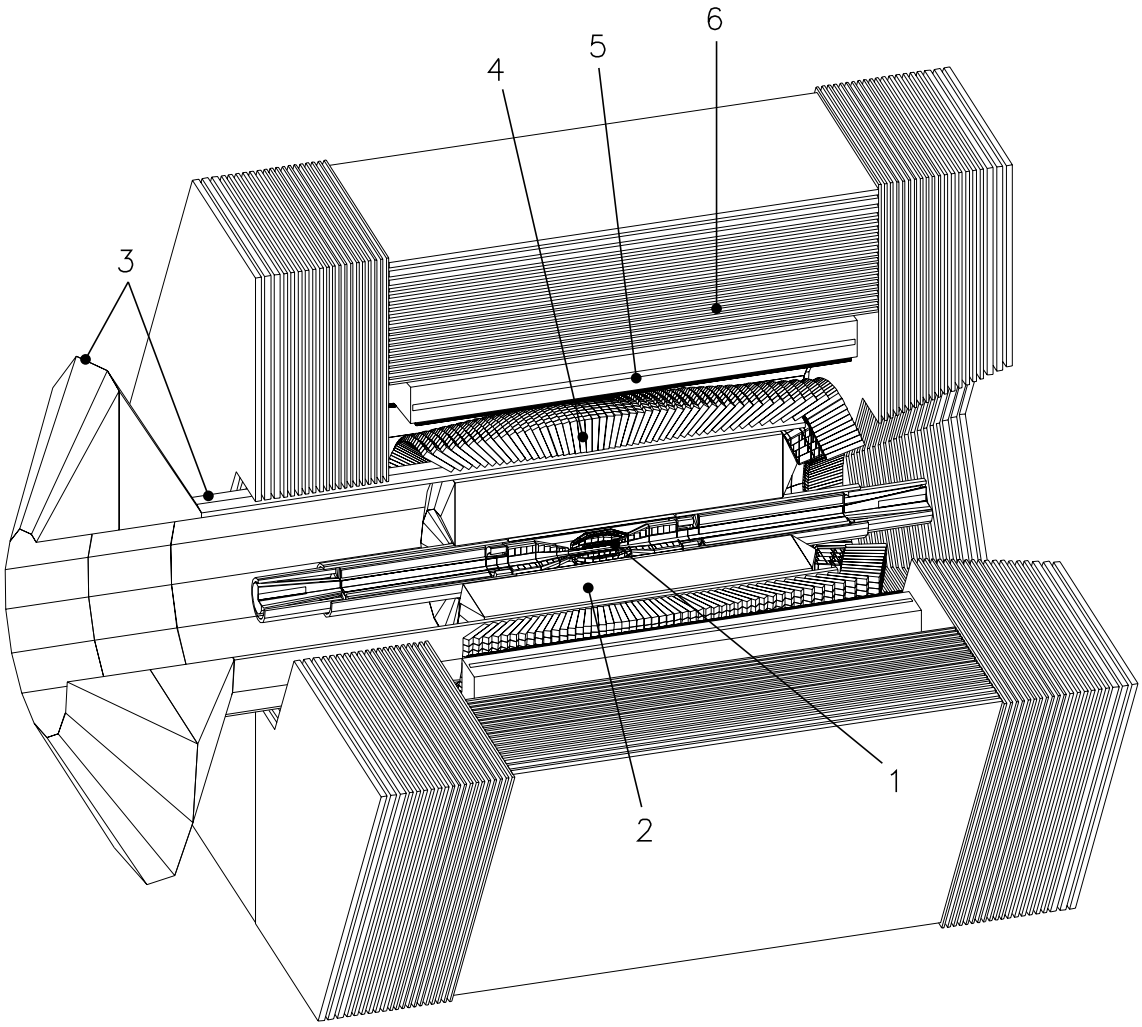

Figure 2-1. *Cut-away view of the BaBar detector showing locations of individual sub-detectors. 1. Silicon Vertex Tracker, 2. Drift Chamber, 3. Detector of Internally Reflecting Cherenkov, 4. Electromagnetic Calorimeter, 5. Magnet, 6. Instrumented Flux Return.*

This detector also serves as the BaBar experiment's inner tracking device, and will provide the only tracking information for charged particles with $p_t < 100$MeV/c. A detailed description of the Silicon Vertex Tracker may be found in [21].

A cut-away view of the detector is shown in figure 2-2. The detector material consists

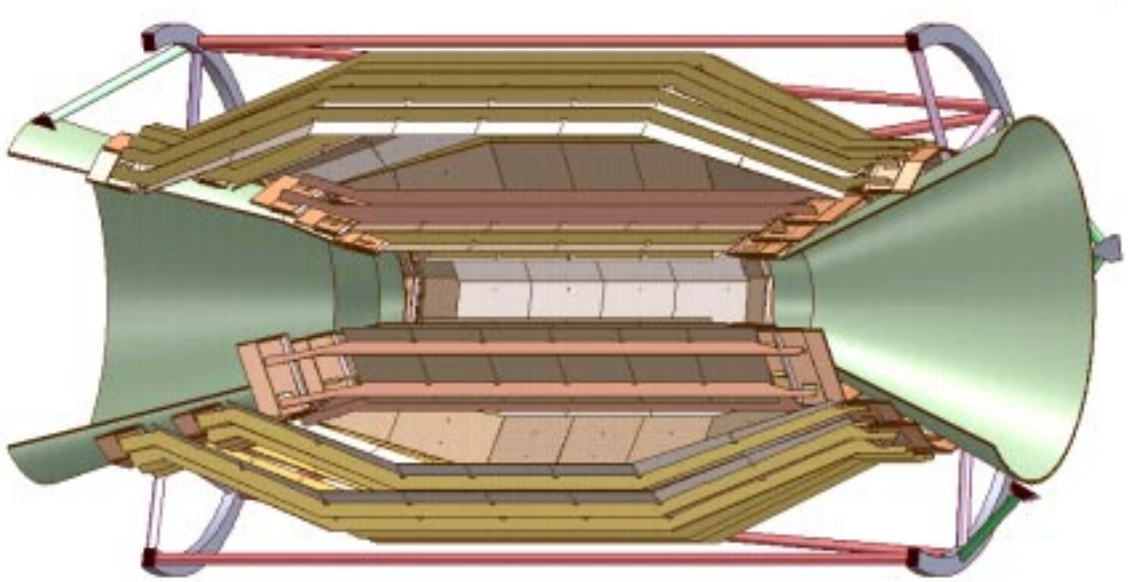

Figure 2-2. *Cut-away view of the BaBar Silicon Vertex Tracker*

of 5 concentric double-sided layers of silicon surrounding the beam pipe from a radius of 3.2cm for the inner layer to 14.4cm for the outer layer. Each layer provides a position measurement in the z and ϕ directions. Figure 2-3 shows the hit resolution obtained from data and simulated events in the z and ϕ directions measured in the inner layer of the Silicon Vertex Tracker as a function of incident track angle. The data events show a slightly larger resolution compared to the simulated events. A description of the Silicon Vertex Tracker hit resolution analysis can be found in [22]. The resolution in the z direction on the measured separation of B decay vertices is $\sim 110 \mu m$ [23] which meets the physics requirements.

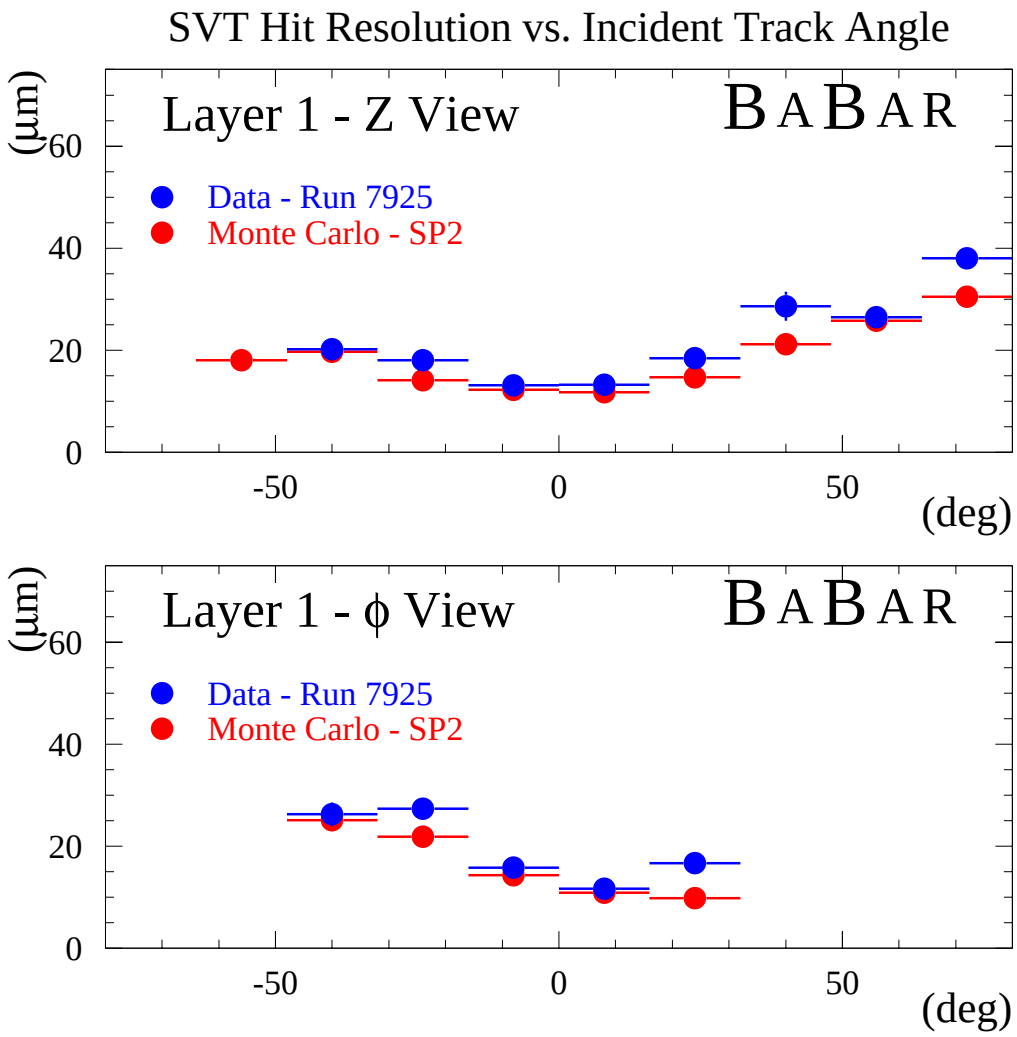

Figure 2-3. *Measured z and ϕ hit resolutions in the inner layer of the Silicon Vertex Tracker as a function of incident track angle from data events (blue) and from simulated events (red).*

The Silicon Vertex Tracker defines the acceptance for the BaBar experiment and can detect charged particles over the polar angle -0.87 $<$ cosθ $<$ 0.96 in the laboratory frame. It has been designed to cover a larger solid angle in the boost direction. The acceptance is limited by the permanent magnets located 20cm either side of the interaction point in the z direction which are required for separating the electron and positron beams.

A small amount of material has been used in the construction to try to minimize multiple scattering which has an adverse effect on the position resolution. The location of the Silicon Vertex Tracker so close to the beam pipe has two important implications. Firstly access is difficult making reliability a primary concern. Secondly, the detector material must be highly resistant to radiation damage.

2.3.2 The Drift Chamber

The reconstruction of exclusive final states is a key component of many physics analyses for which knowledge of particle momenta is required. The main task of the Drift Chamber, the primary source of tracking information for the BaBar experiment, is to provide a momentum measurement of charged particles which traverse it. In addition, dE/dx information from the drift chamber is used for particle identification.

The Drift Chamber immediately surrounds the support tube which encloses the Silicon Vertex Tracker. The detector is shown schematically in figure 2-4. It is a cylindrical device 280cm in length with an inner radius of 23.6cm and outer radius of 80.9cm. The acceptance covers the polar angle -0.92 $<$ cosθ $<$ 0.96 in the laboratory frame. The detector is composed of 10 layers of wires, each layer consisting of 4 inner layers. The wires in the drift chamber make up a series of 7104 hexagonal drift cells. Each cell consists of a 20μm gold-plated tungsten anode sense wire at a potential of 1960V at its centre. The cell boundary is made up of 80μm and 120μm gold-plated aluminium field wires. Position information is determined from the drift time of ions from charged

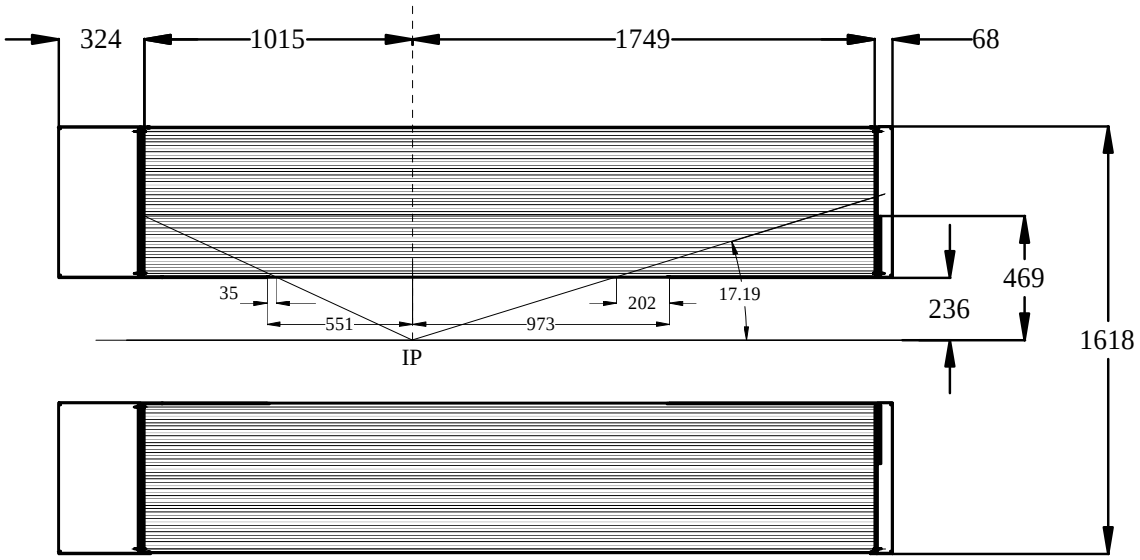

Figure 2-4. *Axial view of the BaBar Drift Chamber. Dimensions are in mm.*

particles traversing a cell. As with the Silicon Vertex Tracker the amount of material has been kept to a minimum to reduce multiple scattering. The gas in the chamber is 80% Helium and 20% Isobutane.

The Drift Chamber cell spatial resolution is an important factor contributing to the momentum resolution for charged tracks, the principal measure of performance for the Drift Chamber. Figure 2-5 shows the Drift Chamber cell spatial resolution obtained using charged tracks from BaBar data. The resolution averaged over the cell is $125\mu m$ which exceeds the performance goal of $140\mu m$. The transverse momentum resolution is $\sigma_{pt}/p_t \approx 0.3\%$.

2.3.3 The Detector of Internally Reflecting Cherenkov Light (DIRC)

The identification of charged particles is necessary for the reconstruction of many exclusive final states. The Detector of Internally Reflecting Cherenkov Light, or DIRC, is a

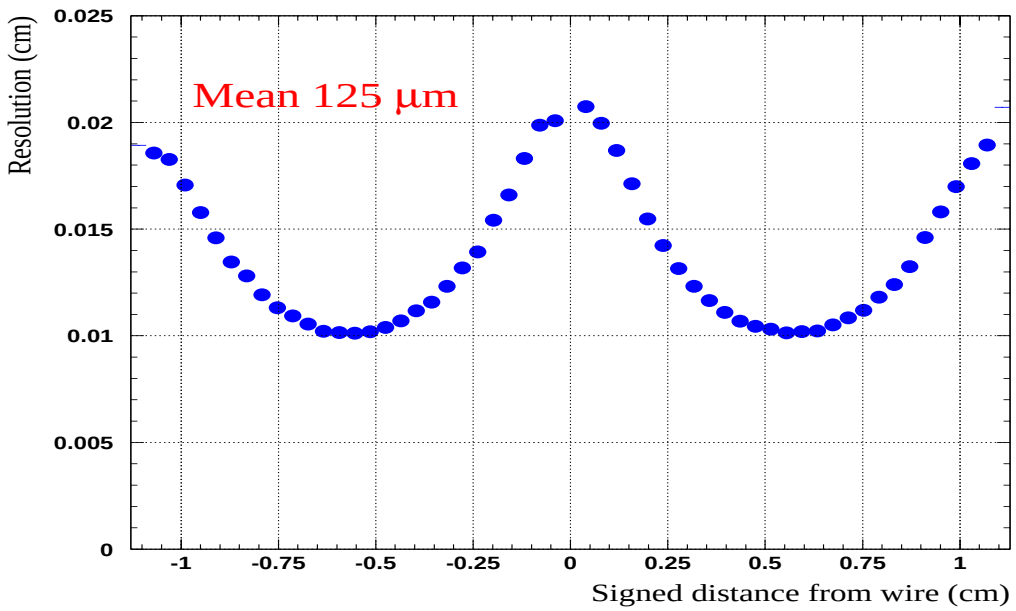

Figure 2-5. *Drift chamber cell spatial resolution as a function of distance measured using charged tracks from BaBar data.*

particle identification device designed to distinguish between charged pions and kaons with momentum greater than ∼250MeV/c. A detailed description may be found in [24].

The detector has a 12-sided polygon barrel section of radius 80cm enclosing the Drift Chamber and made up of an arrangement of 144 quartz bars of length 4.9m. The acceptance over the polar angle is -0.84 $< \cos\theta <$ 0.90 in the laboratory frame. The refractive index of quartz is such that particles traversing the detector travel faster than light in the quartz medium and emit a cone of Cherenkov light. The emitted Cherenkov photons travel along the quartz bars by total internal reflection into a tank of purified water at the backward end of the detector. Cherenkov light which travels along the bars in the forward direction is reflected back by a mirror located at the front end of the bars. The water tank is lined with ∼11000 photomultipliers to detect the Cherenkov photons. The process is shown schematically in a cross section of the detector in figure 2-6.

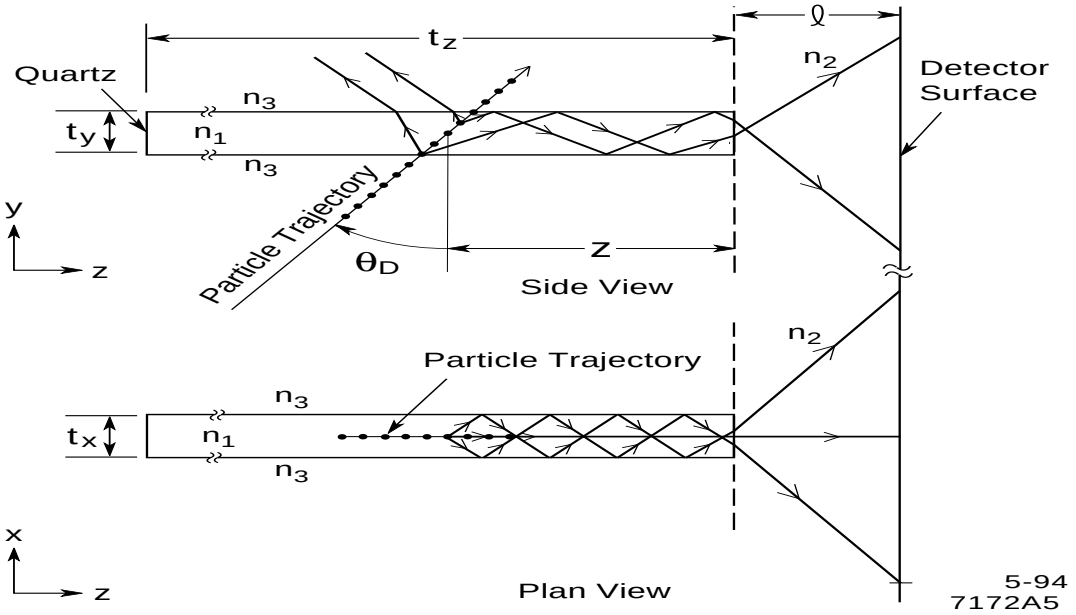

Figure 2-6. *Cross sectional view of the Detector of Internally Reflecting Cherenkov Light (DIRC) showing the path of emitted Cherenkov photons.*

The emitted cone of Cherenkov light is detected by the photomultipliers as a ring which is used to determine the angle of emission of the cone with respect to the charged track. The velocity, β, of an incident particle determines the angle of emission of the cone in a medium of refractive index n:

$$\theta_c = cos^{-1}\left(\frac{1}{\beta n}\right). \tag{2.1}$$

A measurement of the cone angle therefore allows determination of the particle velocity which can be used together with the momentum measured by the drift chamber to determine the particle mass. Figure 2-7 shows the kaon and pion selection efficiency achieved in the DIRC from data events as a function of track momentum. This shows good k/π separation over the momentum range. The performance degrades slightly near the upper end of the momentum spectrum.

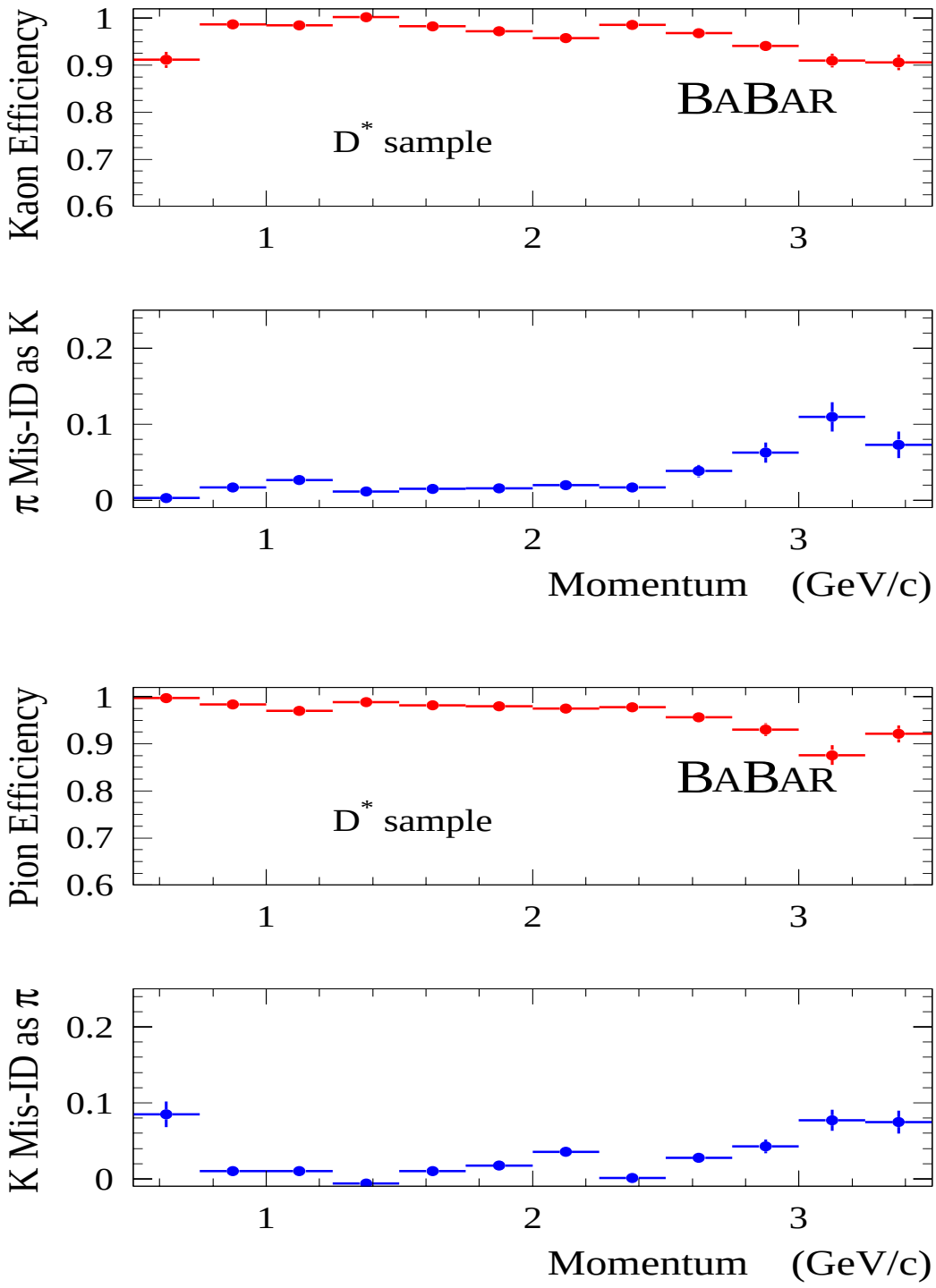

Figure 2-7. *Kaon and pion selection efficiency in the DIRC from data events as a function of track momentum.*

2.3.4 The Electromagnetic Calorimeter

Many CP channels of interest contain π^0s which subsequently decay into low energy photons. Given the small branching fractions of CP channels, it is crucial for CP physics to be able to reconstruct π^0s with high efficiency from the low energy neutral deposits left by the daughter photons producing electromagnetic showers in the calorimeter. The Electromagnetic Calorimeter measures the energy deposits from the interaction of incident charged and neutral high energy particles.

The calorimeter consists of 6580 thallium doped caesium iodide CsI(TI) crystals divided into a cylindrical barrel section and a conical forward endcap. The crystals vary in length from 16.1X_0 in the backward part of the barrel to 17.6X_0 in the forward endcap. Each crystal has a front face of 4.7 $\times$ 4.7 cm^2. The barrel section encloses the DIRC quartz bars and has an inner radius of 90.5 cm and an outer radius of 136 cm. The barrel crystals are arranged in an array of 48 crystals in θ by 120 in ϕ. The crystal layout is shown schematically in figure 2-8. The polar angle acceptance of the calorimeter is $-0.78 < \cos\theta < 0.96$ in the laboratory frame.

The crystal material produces scintillation light during the production of electromagnetic and hadronic showers caused by particle interactions. Free electrons resulting from these showers produce unstable excited states in the thallium atoms which fall back to a stable state with the emission of light. The scintillation light is detected by photomultiplier tubes attached to the back faces of the crystals.

The energy resolution of the calorimeter is given by the expression [18]

$$\frac{\sigma_E}{E} = \frac{a}{E^{1/4}} \oplus b \tag{2.2}$$

where the energy E is in GeV. The intended resolution has $a \approx 1\%$ and $b \approx 1.2\%$. The actual resolution which has been achieved does not match the intended resolution with

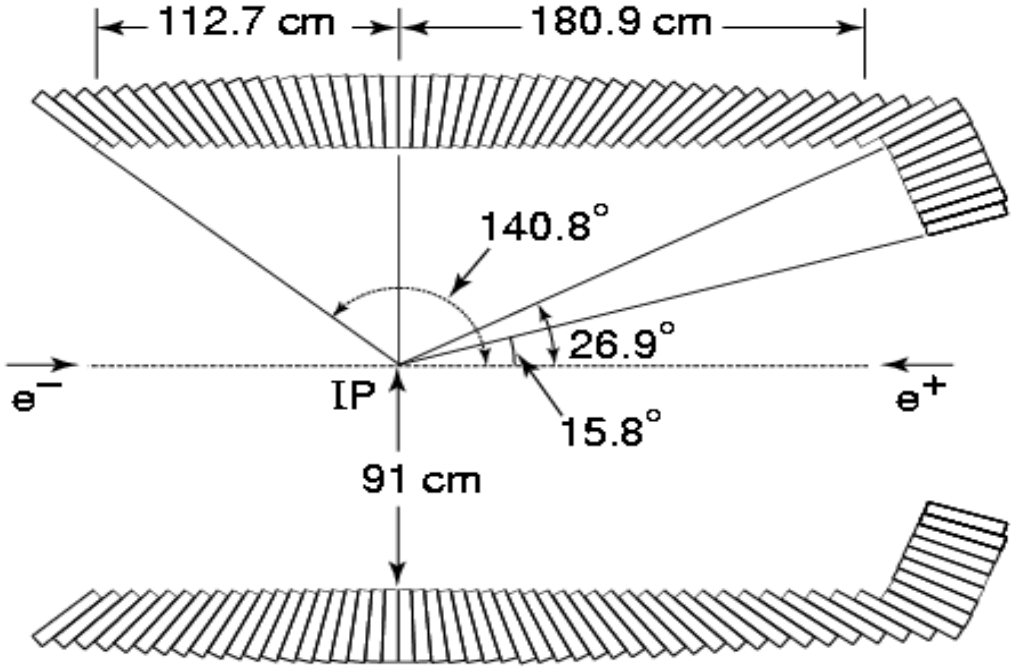

Figure 2-8. *Cross-sectional view of the crystal layout in the BaBar Electromagnetic Calorimeter showing dimensions.*

the terms a and b having the values $a \approx 1.33\%$ and $b \approx 2.1\%$ [23]. The expected angular resolution of the calorimeter is given by the expression [19]

$$\sigma_{\theta,\phi} = \frac{3mr}{\sqrt{E}} + 1mr \tag{2.3}$$

where again the energy E is in GeV. Measured values of $\sigma_{\theta,\phi}$ have indicated that again the actual resolution is larger than the target value [23].

The π^0 reconstruction efficiency in the calorimeter is a performance parameter which will vary with individual analyses of the data. This is discussed in the context of $\tau \rightarrow \rho\nu_\tau$ reconstruction in chapter 4.

2.3.5 The Solenoidal Magnetic Field

A constant magnetic field of 1.5T is produced by a superconducting solenoid. The curvature of the path of charged particles moving through the magnetic field allows determination of momentum in the tracking devices. The momentum resolution depends on the accuracy with which the curvature can be determined, and this increases with the magnetic field. A field of 1.5T was chosen to achieve good momentum resolution. The direction of curvature also allows the charge of the particle moving through the field to be determined.

2.3.6 The Instrumented Flux Return

The Instrumented Flux Return is the outermost BaBar detector and is used for the identification of muons. A detailed description of the Instrumented Flux Return may be found in [25]. The structure for this detector is the magnetic flux return iron. The detector consists of a hexagonal barrel section shown schematically in figure 2-9, and both forward and backward endcaps. The acceptance covers the solid angle from 300mrad in the forward direction to 400mrad in the backward direction. The structure consists of 18 layers of iron plates of increasing thickness which range from 2cm for the inner layer to 10cm for the outer layer. The active detectors are Resistive Plate Chambers which are sandwiched in the gaps of $\sim$3.2cm between the layers of iron plates. The are 19 layers of Resistive Plate Chambers in the barrel section, and 18 layers in each endcap. In the barrel section there is also an additional inner cyclindrical Resistive Plate Chamber enclosing the Electromagnetic Calorimeter. Each Resistive Plate Chamber consists of a gas contained between two Bakelite plates, each of thickness 2mm. There is a potential difference between the plates with one plate operating at high voltage and the other plate earthed. A charged particle traversing the chamber produces a spark which gives rise to

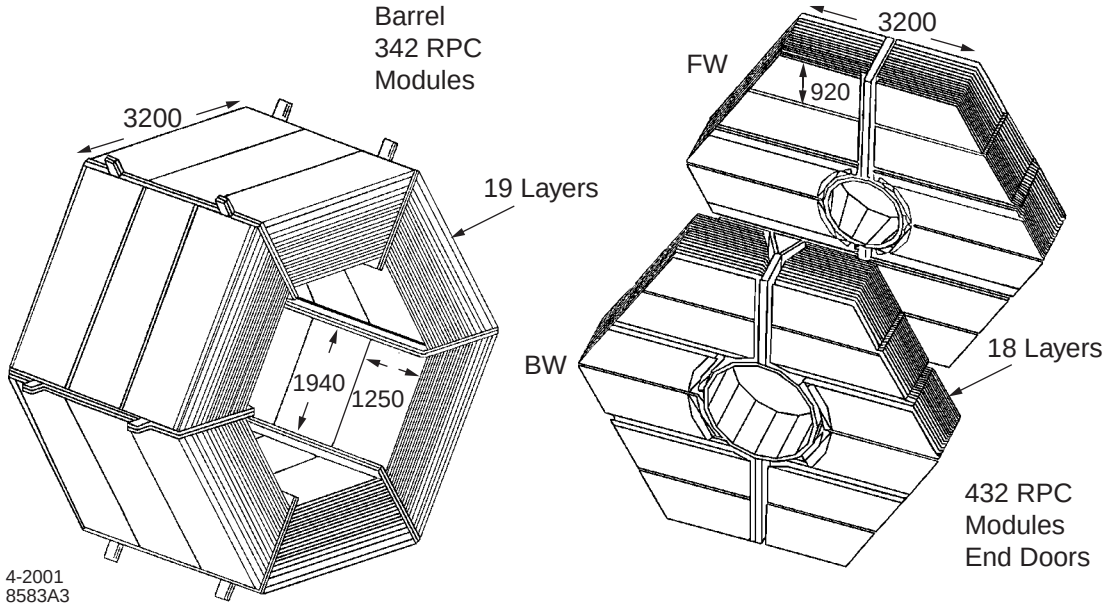

Figure 2-9. *Schematic of the BaBar Instrumented Flux Return showing the barrel section and forward and backward endcaps.*

electrical signals in aluminium strips running orthogonally along the plates. The strips provide a position measurement in the z and ϕ directions in the barrel section and in the x and y directions in the endcaps.

The identification of muons is important for the study of τ leptonic decays presented in this thesis. The performance for muon identification using the Instrumented Flux Return is described in chapter 5.

2.3.7 The Trigger System

In addition to studies of B physics, the BaBar experiment provides an opportunity for many other physics analyses. Interesting physics events at the $\Upsilon(4S)$ resonance include charm, τ, and $\gamma\gamma$ events. The BaBar trigger system aims to select events containing channels of interest to the BaBar physics program with high efficiency from a high background

environment. The selection efficiency is required to be $> 99\%$ for B physics events and $> 95\%$ for charm and τ events. A full description of the trigger system requirements is given in [26].

The structure of the BaBar trigger system is shown schematically in figure 2-10. The trigger system has two levels. The first, Level 1, is a hardware trigger which reduces the rate of accepted events to no more than 2kHz. A detailed description may be found in [27]. Level 1 trigger decisions are based on information from the Electromagnetic Calorimeter and Drift Chamber only. The three main components of this trigger are the Calorimeter Trigger [28], the Drift Chamber Trigger [29], and the Global Trigger. The Calorimeter Trigger receives and processes crystal tower energies[1] from the calorimeter to provide the Global Trigger with ϕ positions of calorimeter clusters passing different energy thresholds. The Drift Chamber Trigger provides the Global Trigger with ϕ positions of long and short charged tracks in the Drift Chamber. The Global Trigger combines the calorimeter and Drift Chamber information and makes the Level 1 trigger decision. A Level 1 trigger requires at least two tracks in the Drift Chamber, one reaching the Drift Chamber outer layers ($P_t > 180$ MeV/c), the other reaching at least the middle layers ($P_t > 120$ MeV/c), and two clusters in the calorimeter. Most Level 1 triggers are caused by beam induced backgrounds. Beam particles which undergo bremsstrahlung or coulomb scattering from residual gas in the beam pipe may hit the beam pipe material. This interaction can result in charged tracks producing the required Drift Chamber hits and calorimeter clusters. The time between beam crossings is only 4.2ns and is not enough time to read out the detector. Digitised detector data are therefore written to circular buffers in the front end electronics while waiting for a Level 1 trigger decision. The depth of the buffers is 12μs, the time allowed for the Level 1 trigger to make a decision.

If an event is accepted by the Level 1 trigger, event data are read out from the sub-detector circular buffers and combined (a process known as event building) before being passed

[1] A crystal tower is a group of 3×8 crystals in the calorimeter.

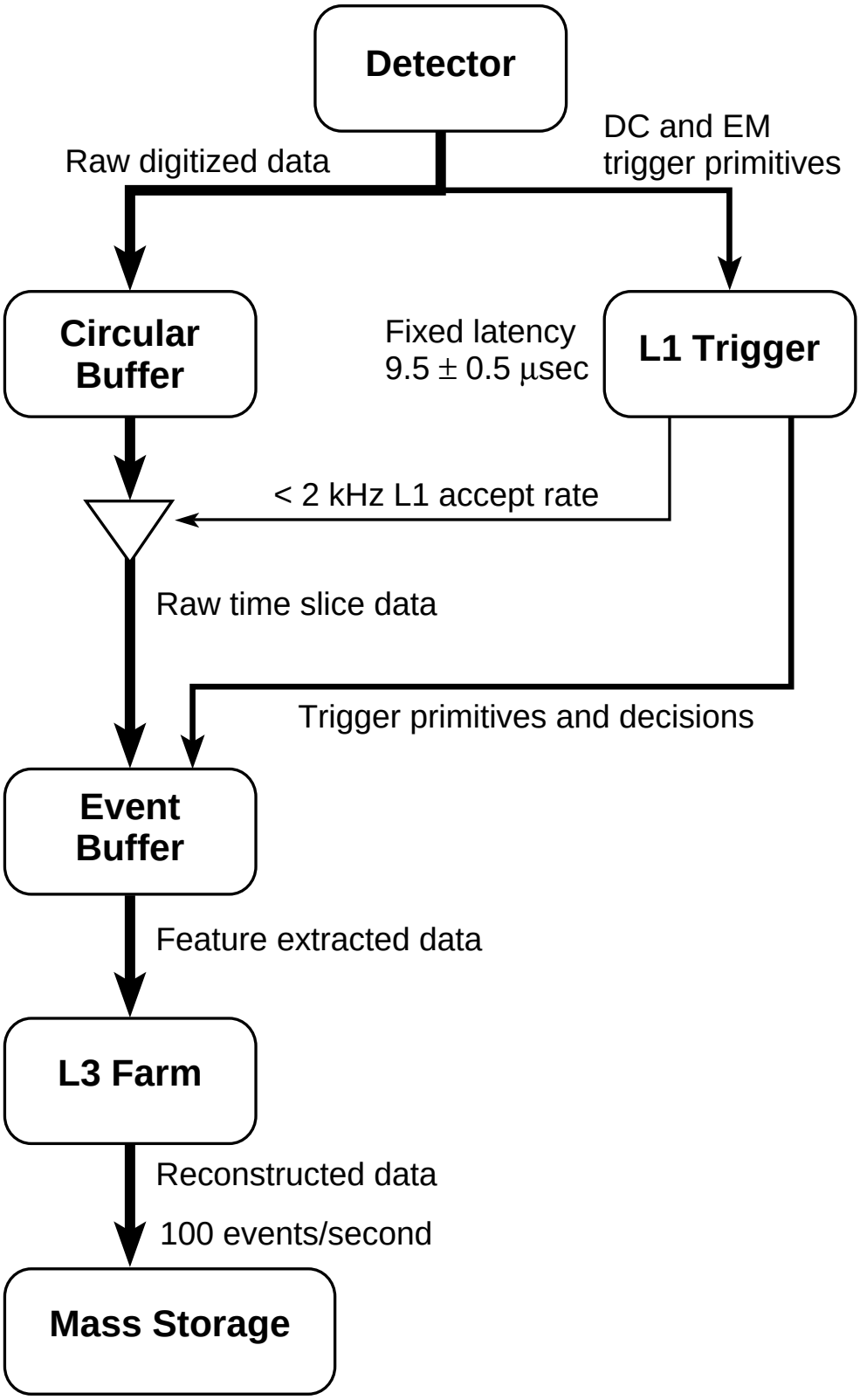

Figure 2-10. *Structure of the BaBar Trigger System showing path for event data.*

to the second trigger level, the Level 3 trigger[2]. This allows the Level 3 trigger to use information from all sub-detectors in making a decision to accept or reject an event. Level 3 is a software trigger with a maximum rate of 100Hz. The Level 3 algorithms are designed to reject those background processes accepted by the Level 1 trigger while retaining the interesting physics events. Event data accepted by the Level 3 trigger is stored to tape.

[2]The second trigger level is known as Level 3 since the design allows for an intermediate Level 2 software trigger to be implemented at a later time if required.

3

Online Software for the Calorimeter Trigger

3.1 Introduction

The calorimeter trigger is an essential part of the BaBar experiment. The calorimeter trigger software is intrinsic to the operation of and acquisition of data from the calorimeter trigger. A key factor in the design of both the online and offline software for the BaBar experiment is the object oriented approach which has been taken. A description of the principal features of object oriented software design is given in this chapter. The design of and the major roles of software written for the calorimeter trigger will also be described.

3.2 Object Oriented Software Design

The software implementation for the BaBar experiment is in the C++ programming language which supports object oriented techniques. Detailed descriptions of object oriented design methods may be found elsewhere [30, 31]. This section outlines the program structure of object oriented software and summarises the major concepts and terminology.

3.2.1 Structure of Object Oriented Software

Object oriented design is a further development of the established concept of simplifying complex software by splitting it into a set of smaller well defined tasks. In conventional programming languages these tasks are implemented as functions with the data to be operated on being passed into the functions. Using this approach, functions have to know what form the data will be arriving in. If at a later time the way the data is represented changes, all functions which use that data also need to be modified to expect the new data format. In large software projects, this kind of code maintenance can be a significant task and software can be easily broken or become highly unstable.

In object oriented software the program structure is designed not in terms of functions but in terms of data *objects*. An object represents a set of data and as such has a definite state defined by the values of its own data. An object also provides a collection of functions which may operate on the data owned by the object and define the behaviour of the object. The functions and data variables which are associated with an object are defined by the object's *class*. Multiple objects may belong to the same class definition. Objects belonging to the same class will have the same behaviour since they share the same code implementation for their functions. They will also share the same data variables but they may hold different values in different objects hence the objects may not have the same state (data values). Each object also has a unique name, it has an identity.

3.2.2 Concepts and Terminology

The list of functions provided by an object form the object *interface*. From a users point of view an object is simply an interface. An object's implementation, the internal variables belonging to an object and the implementation of an object's functions are distinct to the object interface. The only way to access an object's data from outside the object is via

the interface. We say that an object *encapsulates* its data. Moreover, the implementation is not visible from outside the object but is *hidden* behind the interface. An important consequence of this is that a user of the object does not know (or need to know) how the object performs any of its functions. A user only needs to know (and can only know) about the object interface. In this sense, a user may think of an object interface as providing a list of *services*. If the user requires a particular service it must ask the object to carry it out. This protects the user from changes to the object's implementation, arguably the major benefit of object oriented design. This localisation means that code becomes more modular and therefore easier to maintain. The concept of characterising an object by its interface is known as abstraction.

Object orientation incorporates the inheritance relationship between classes. Inheritance is a mechanism which allows common generic code to be shared between classes. A class can acquire the interface and implementation of a generic parent class, or base class. The interface may then be added to or the implementation of any of the functions overridden to produce the required specialisation. Advantages come from the generic code being re-used and the easy extensibility, since sub-class extensions do not affect the parent class code. In some cases the parent class may only provide an interface and leave all implementation to its sub-classes. The parent class is then described as an abstract base class. A function which has no implementation in the parent class is described as a *pure virtual* function.

3.3 The BaBar Data Acquisition Software

The online software for the calorimeter trigger must work within the context of, and is therefore intrinsically linked to the BaBar core data acquisition software. The major task of the data acquisition software is to transport event data from the detector to the offline environment for further processing and storage. A full description of the data acquisition

software can be found elsewhere [32, 33]. This section outlines the aspects relevant to the design and implementation of the online software for the calorimeter trigger.

3.3.1 The Finite State Machine Model

Each of the component sub-detectors which make up the BaBar detector is operated within the context of a *run* using a Finite State Machine model provided by the BaBar core data acquisition software. The Finite State Machine models the different stages each sub-detector must go through to either take data or perform a calibration run from start to finish. The different stages of the Finite State Machine are shown schematically in figure 3-1. The main stages of a run are 'booted', 'running', and 'active' illustrated in the figure. In the initial 'booted' stage the system is in a random state and the detector front end electronics must be configured before they are ready to take data. The system ready for data taking is represented by the 'running' state. In the 'active' state the detector takes data. The smaller rounded boxes in the figure represent states within the three main stages. The transition from one of these states to the next (represented by arrows in figure 3-1) corresponds to an *action* taken by the sub-detector to reach the next stage. An action in practice is the execution of a piece of sub-system code to control or configure its front end electronics. Examples of software executed in the calorimeter trigger during transitions are described in section 3.4. The core data acquisition software provides the interface through which sub-detector electronics may be controlled during transitions via an abstract base class.

3.3.2 Data Transportation

Event data is transported on transitions of the Finite State Machine and organised into software *containers*. A container is a software abstraction designed to encapsulate

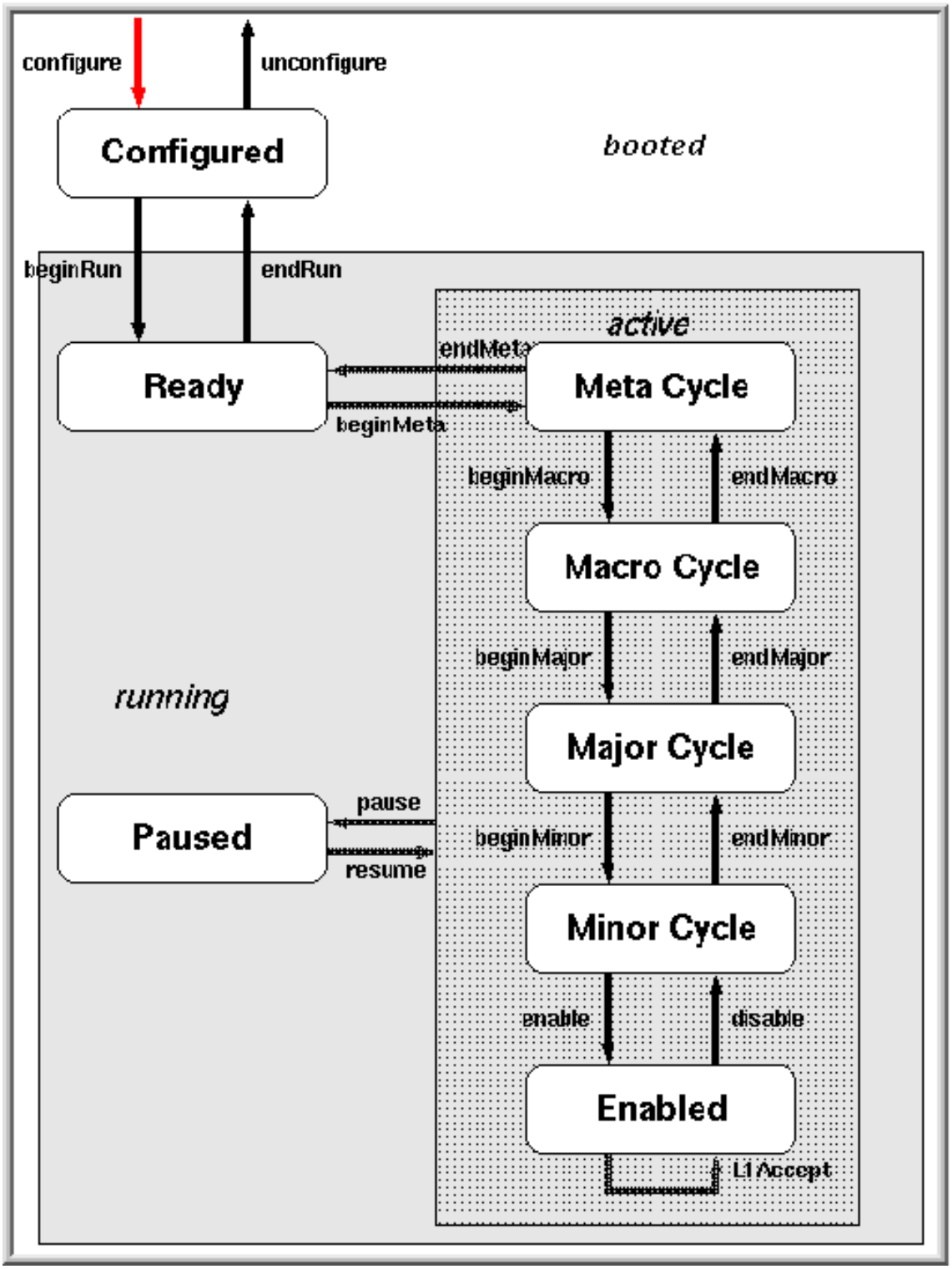

Figure 3-1. *States of the data acquisition software Finite State Machine modelling the different stages in the operation of the BaBar detector. Arrows represent transitions between states.*

detector data. On any *end* transition within the active state of figure 3-1 data may be transmitted out of the Finite State Machine environment and placed into an area of shared memory. Individual containers of detector data may be retrieved from this area by an offline Unix machine. The data can then be accessed through the container interface. A useful application is the processing of calibration data. An example of the use of containers applied to the calorimeter trigger is given in section 3.4.2.2.

3.4 Software for the Calorimeter Trigger

The sequence of transitions of the data acquisition software Finite State Machine (represented by arrows in figure 3-1) are implemented in the calorimeter trigger software as a set of C++ classes which allow connection to and control of the calorimeter trigger electronics. It is desirable to be able to perform several different types of run (e.g. calibrations, data taking) and the calorimeter trigger software has been structured to provide this flexibility and follow separate paths for different run types. This section describes the software implementation following the path taken for an individual type of run for the calorimeter trigger.

3.4.1 Common Transition Classes

The first three transitions of the Finite State Machine (figure 3-1) are the configure, beginRun, and beginMeta transitions. The software implementation in the calorimeter trigger for these transitions is common to all run types. The relationship structure of the classes written to implement these transitions is illustrated in figure 3-2 and the individual classes are described below[1].

[1] See appendix B for an explanation of the notation used for class relationship diagrams in this chapter.

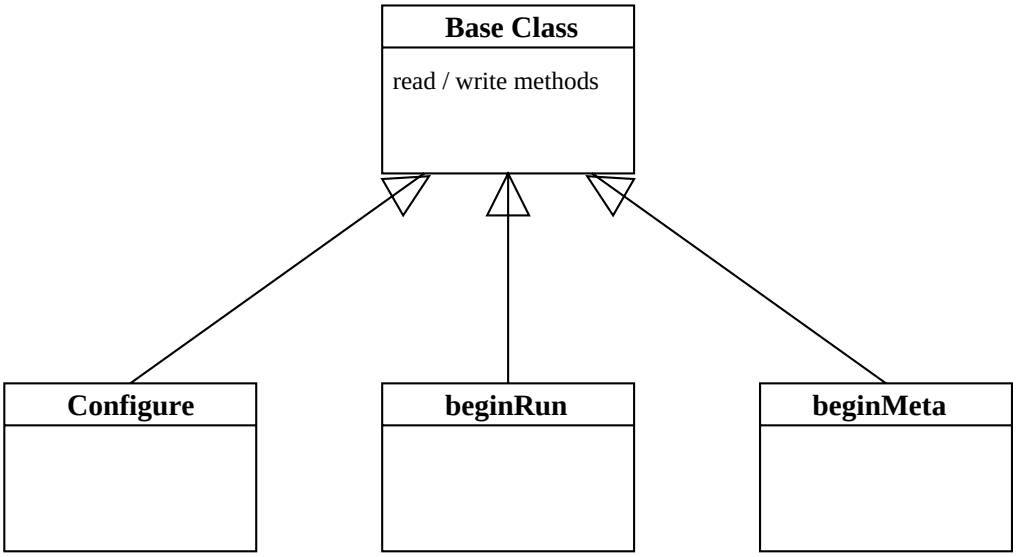

Figure 3-2. *Relationship of classes written to implement the initial Finite State Machine transitions for the calorimeter trigger.*

During the initial stages of a run, the calorimeter trigger electronics have to be correctly configured. The calorimeter trigger configuration requires reading from and writing to the calorimeter trigger electronics. Access to the read/write code implementation is therefore required by the transition classes. This is achieved by placing the read/write method implementation into a base class. The base class interface is made available to the calorimeter trigger transition classes through inheritance, represented by the arrows in figure 3-2, providing access to whichever read/write methods are required on any particular transition.

The configure transition class defines the calorimeter trigger object corresponding to the Finite State Machine configure transition. The interface provides the method for the configuration of the calorimeter trigger hardware. The configuration method consists of a switch responsible for determining the type of run and performing the appropriate configuration via the base class interface. There are two parts to the configuration. Firstly,

key sets of constants[2] are downloaded to the calorimeter trigger electronics via the base class interface. Secondly, the calorimeter trigger may be configured to operate in either a diagnostics or data taking mode. The diagnostics configuration allows simulated data to be inserted either at the inputs to the calorimeter trigger processors or at the calorimeter trigger outputs. The data taking configuration is used for data taking runs and other calibrations. In this configuration real data from the calorimeter is expected at the inputs and the results of processing this data are sent to the global trigger.

The beginRun transition class corresponds to the Finite State Machine 'beginRun' transition from the 'configured' state to the 'ready' state illustrated in figure 3-1. This is also a derivative of the base class. The sole responsibility of this class is to read back and verify, via the base class interface, the configuration data loaded into the calorimeter trigger hardware during the configure transition.

The beginMeta transition class is the calorimeter trigger class associated with the Meta level 'begin' transition in figure 3-1. This class provides the flexibility to perform different types of run and acts as a switch to determine which branch of the calorimeter trigger software is executed during the rest of the run.

3.4.2 Frameclash Test Software

Transitions (arrows in figure 3-1) below the Meta Cycle state in the 'active' stage of the Finite State Machine have different software implementations for different types of run. The transitions within the active state may be sequenced as a set of nested loops for calibration or diagnostics purposes. An example of this is the calorimeter trigger frameclash test. The frameclash test is essential to the correct operation of the calorimeter trigger. This section

[2] A description of the constants required for the calorimeter trigger configuration may be found elsewhere [34, 35]. The intention here is to highlight the software structure.

describes the purpose of the frameclash test and the software implementation written to perform the test. The results from an example frameclash run will also be shown.

3.4.2.1 Frameclash Definition

The calorimeter front end electronics sample and digitise crystal tower energies[3] at a rate of 3.7MHz. This task is performed by 120 electronics modules, each module processing either 2 or 3 tower energy sums. Digitised tower energy sum data are sent along cables to the calorimeter trigger from the calorimeter front end electronics at the same rate, 3.7MHz, to form the input to the calorimeter trigger processors. Timing differences between the calorimeter electronics modules mean that tower energy sum data from different crystal towers in the calorimeter taken during the same time sample do not arrive simultaneously at the calorimeter trigger inputs. It is therefore necessary to synchronise all the tower energy sums from the same time sample before processing in the calorimeter trigger. The synchronisation is achieved in the calorimeter trigger hardware. A schematic of the synchronisation logic[4] is shown in figure 3-3. A detailed description of the synchronisation logic can be found elsewhere [36]. A brief summary is given here.

Cables from the calorimeter carry either 2 or 3 tower energy sums and a single bit, known as the *frame* bit, which is synchronised to the first bit of the tower energy data words, illustrated in figure 3-4. On arrival at the calorimeter trigger the tower energy sums on each cable are written into memory buffers in the calorimeter trigger processors. The arrival of the cable frame bit indicates the start of the tower energy data and is used to trigger the writing of the data bits to individual memory addresses which is controlled by a counter (see figure 3-3). The logic in figure 3-3 shows an example for a single cable. To align the data from all cables, all memory buffers containing cable data are then read out simultaneously a short time later, the readout being triggered by a separate bit, also

[3] A crystal tower is a group of 3×8 crystals in the calorimeter.

[4] The acronym 'TPB' in figure 3-3 stands for 'Trigger Processor Board'.

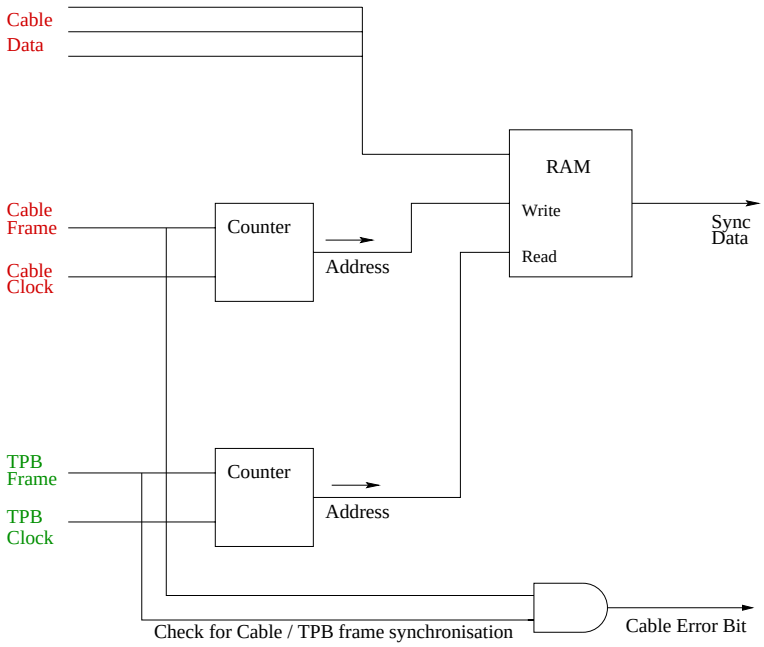

Figure 3-3. *Schematic of the hardware logic used for synchronisation of calorimeter tower energy sum data in the calorimeer trigger. The example shown is for a single cable.*

referred to as a frame bit, generated by the calorimeter trigger at 3.7MHz and out of phase with the incoming cable frame bit.

The relative timing of the two frame bits has an important implication. To ensure the integrity of the tower energy sum data, the memory buffers must not be written to and read from simultaneously. This would lead to unpredictable behaviour and could potentially lead to data from different time samples being processed together, or the corruption of tower energy sum data. This situation would occur if the time of the incoming cable frame bit and the generation of the calorimeter trigger frame bit were to coincide. This is the definition of a *frameclash*. If a frameclash occurs it is flagged in the hardware as a cable error.

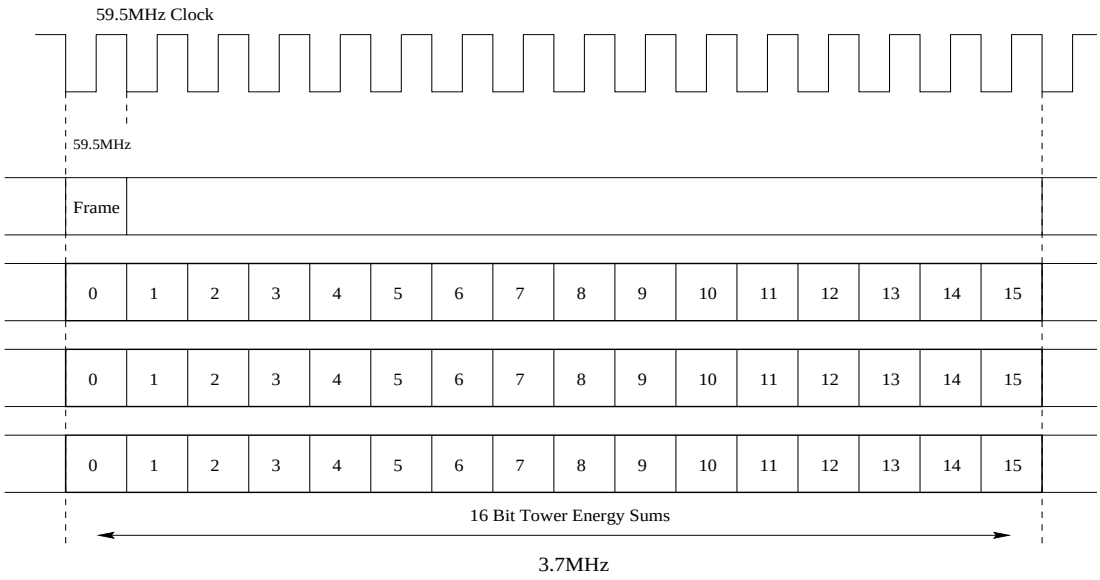

Figure 3-4. *Schematic of data carried on a cable from the calorimeter to the Calorimeter Trigger. The example shows 3 tower energy sum 16-bit data words and the frame bit which indicates the start of the tower energy sum data.*

3.4.2.2 Frameclash Test

The primary goal of the frameclash test is to ensure a frameclash does not occur on any of the 120 cable inputs to the calorimeter trigger during data taking. The calorimeter electronics have the ability to delay sending the tower energy sum data (and corresponding frame bit) by up to 0.27μs (one 3.7MHz cycle) in units of 16.8ns. The aim is to find a suitable value for this delay so that a frameclash situation is avoided. The frameclash test does not need to be performed often. Once a suitable frame delay value has been found it can be programmed into the calorimeter electronics modules and does not need to be changed between runs. During the calibration the time delay of the frame bits sent on each of the cables from the calorimeter is incremented over a whole 3.7MHz cycle. There are 16 different delay values covering a cycle, and for each delay the calorimeter trigger cables are scanned for cable errors. Each frame delay increment is performed

on a beginMajor transition of the Finite State Machine. The sequence of transitions from beginMajor through to endMajor are required to process one frame delay value and form an outer loop which is executed 16 times. For each frame delay, an inner loop of transitions is executed multiple times from beginMinor through to endMinor. The cables are scanned for errors during the L1Accept transition in this inner loop. The class relationship structure of the software implementation for this transition is shown in figure 3-5.

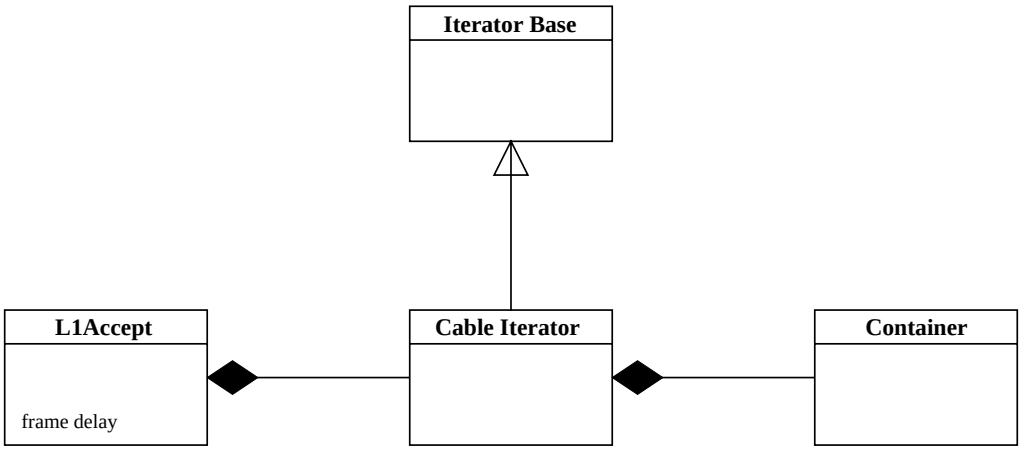

Figure 3-5. *Relationship of classes written to implement the accumulation of cable error data for the calorimeter trigger frameclash test.*

The L1Accept transition class encapsulates the current cable frame delay. It also contains a cable iterator object which is instantiated during the transition. The cable iterator is a derivative of a more general iterator base class designed to iterate over the calorimeter trigger processor boards. The base class defines a pure virtual function which sub-classes must implement to access the calorimeter trigger data on each processor board. The cable iterator derivative provides an implementation for the virtual method which scans each of the cables and access the cable error data. This class owns a container object into which cable error data is accumulated for all cables.

After 16 iterations of the outer loop of transitions the cable error data corresponding to each frame delay has been accumulated, into the container. The container is then transported to the endMacro transition where it is transmitted out of the Finite State Machine environment.

An offline module has been written which finds and retrieves the container of cable error data from the shared memory area. The cable error data is accessed by this module through the container interface and processed to produce histograms of cable error data for subsequent analysis. Figure 3-6 shows an example of the results from a frameclash test. It

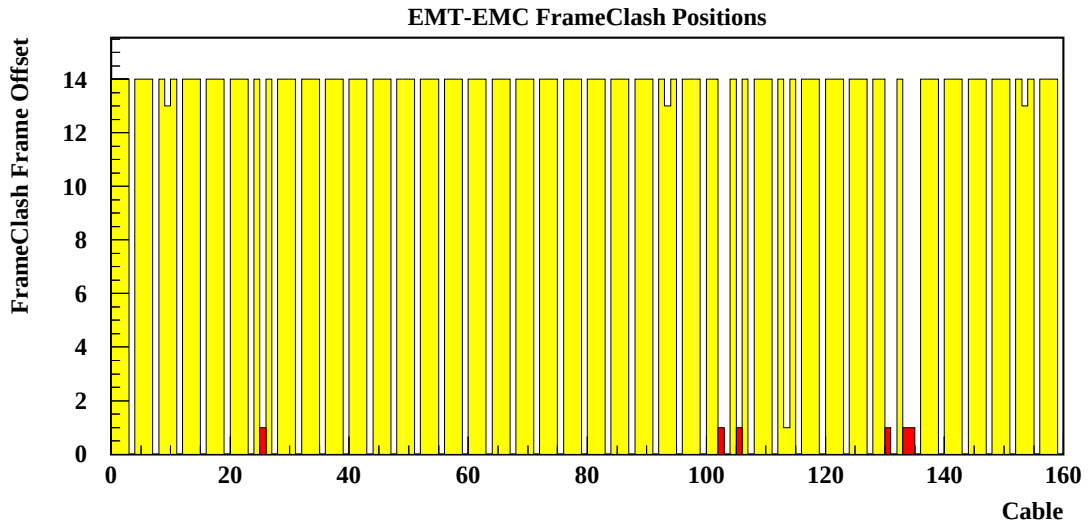

Figure 3-6. *Summary of frameclash positions on all calorimeter trigger input cables determined from the frameclash test software. Possible problem cables are indicated by shorter dark shaded regions.*

gives a summary of the frame delay values where frameclashes occured for all calorimeter trigger cables. It indicates that a frameclash occurs at the same frame delay value on almost all of the cables. In this example any of the 16 delay values other than 13 or 14 would be suitable for the frame delay setting. Possible problem cables are indicated by the shorter dark shaded regions. These may require further investigation if they are not known

problems. To aid in this, histograms of the cable errors accumulated on individual cables for each of the sixteen delay positions for the frame bit can also be viewed. Examples for several cables are shown in figure 3-7. A single spike in each histogram indicates the frameclash position. Problems such as disconnected or bad cables, or bad calorimeter electronics modules would show up in these plots as completely filled histograms or as histograms showing intermittent spikes. This useful feature meant the frameclash test was often used for this purpose during development of the calorimeter trigger.

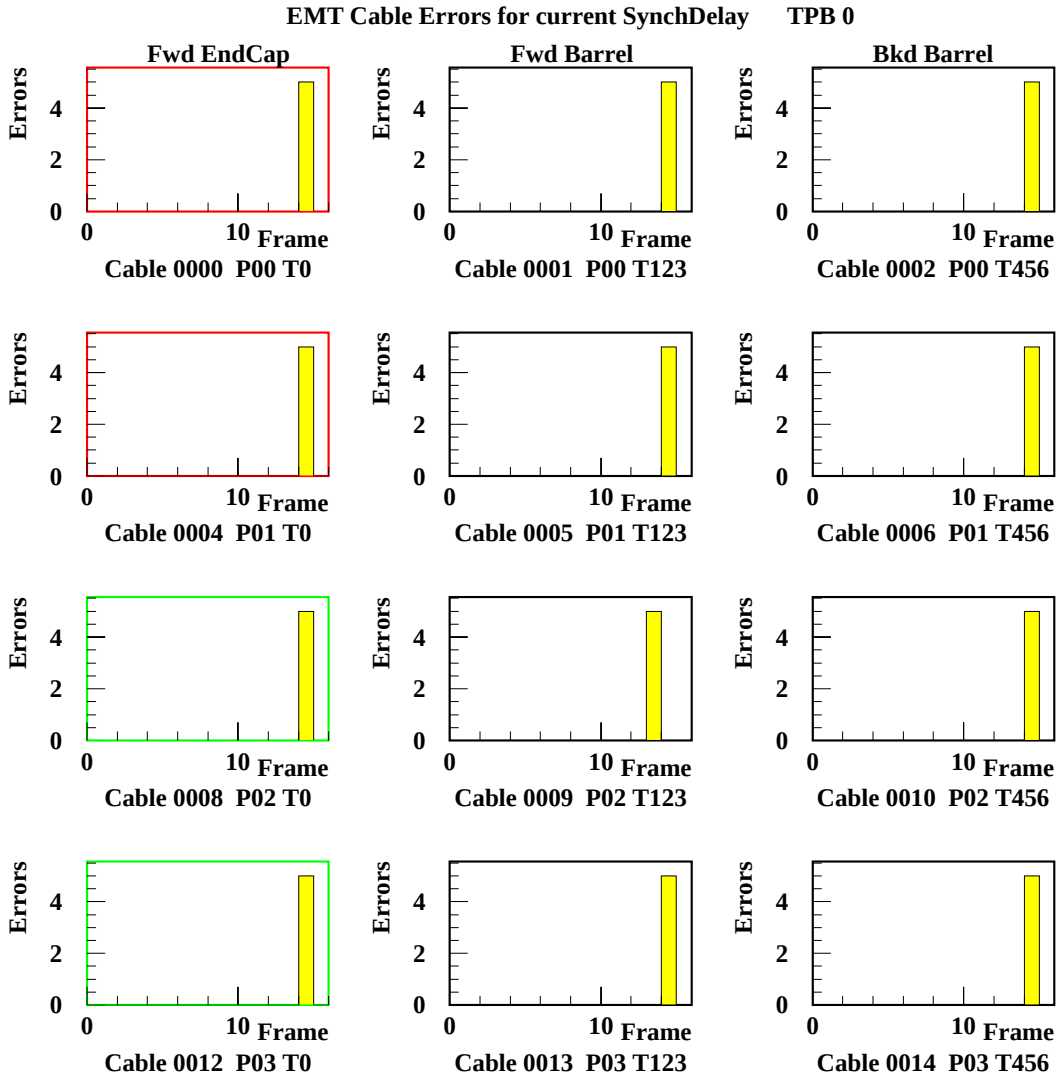

Figure 3-7. *Errors accumulated on calorimeter trigger input cables as a function of the time delay of the incoming frame bit on the cable from the calorimeter. The large spike in each histogram indicates the frameclash position.*

4

Selection of $\tau^+\tau^-$ Events

4.1 Introduction

The short lifetime of the τ lepton makes it possible to study its decay modes inside the BaBar detector. The initial stage of a study of τ decays is the separation of $e^+e^- \to \tau^+\tau^-$ events from other final states of electron-positron collisions at the $\Upsilon(4S)$ resonance. This chapter will describe the technique used for the selection of $e^+e^- \to \tau^+\tau^-$ events in this analysis. A summary of the performance of the event selection method will also be given.

4.2 Event Tagging Using the $\tau \to \rho\nu_\tau$ Channel

An accurate measurement of the τ leptonic branching ratios requires a sample of τs which has high purity and is unbiased. Since the decay modes of the individual τs in any τ pair event are uncorrelated, the identification of the decay mode of one τ may be used to tag the event as a $\tau^+\tau^-$ event allowing a measurement to be made on the decay of the remaining τ. Identifying one of the decay modes will also suppress backgrounds from non-τ events increasing the purity of the selected τ sample.

The aim of the analysis presented here is to identify $e^+e^- \to \tau^+\tau^-$ events through partial reconstruction of the channel $\tau \to \rho\nu_\tau$. This channel has the largest branching fraction of the τ (Appendix A) accounting for a quarter of all τ decays and making it an ideal mode for tagging τ events.

The Feynman diagram describing the charged weak interaction process for the $\tau \rightarrow \rho\nu_\tau$ decay channel is shown in figure 4-1. The charged ρ is a short lived state which decays via

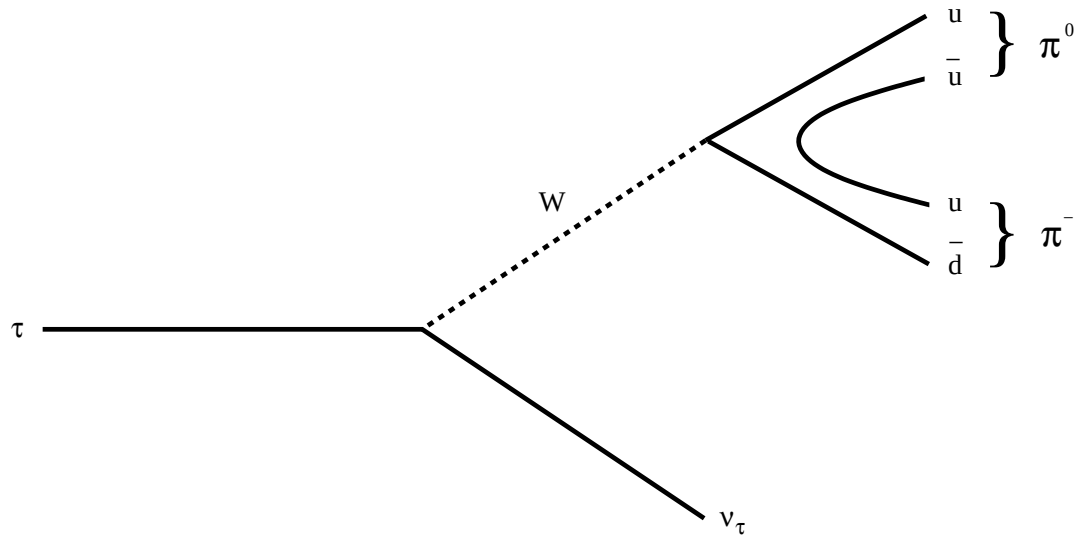

Figure 4-1. *Feynman Diagram describing the charged weak interaction process for the $\tau \rightarrow \rho\nu_\tau$ decay channel.*

a strong interaction process to a charged and a neutral pion. The π^0 is a highly unstable particle and decays rapidly via the electromagnetic process $\pi^0 \rightarrow \gamma\gamma$. The π^0 lifetime is only 0.8 x 10^{-16}s.

The signature for a $\tau \rightarrow \rho\nu_\tau$ event in the detector is the existence of a charged track from the charged pion and either one or two neutral clusters[1] in the calorimeter resulting from the daughter photons in the decay of the π^0. There will also be missing energy due to the neutrino not being detected. In some cases one or both of the photons may convert into an electron-positron pair resulting in additional charged tracks.

[1]A cluster is a continuous region of crystals in which energy from one or more incident particles has been deposited.

4.3 Event Selection

The event selection has been carried out on $0.6 fb^{-1}$ integrated luminosity of data taken by the BaBar experiment at the Υ(4S) resonance during 2000. The event is first divided into hemispheres in the centre of mass defined by the plane perpendicular to the thrust axis of the event. The thrust axis is defined as[15] the direction in which the sum of the longitudinal momenta of the particles is a maximum. The tagging hemisphere is required to have exactly one well reconstructed charged track originating near the interaction point and at least one neutral cluster in the calorimeter. The opposite hemisphere is required to have at least one well reconstructed charged track originating near the interaction point. A charged track is defined using standard cuts for the BaBar experiment to have at least 12 hits in the Drift Chamber and to have transverse momentum in the range 0.1$< P_t <$ 10 GeV/c. In addition, the distance of closest approach to the interaction point is required to be within $\pm$10cm in the z direction and within 1.5cm in the xy plane perpendicular to the beam. Only tracks which fall within the polar angle acceptance of $0.41 < \theta < 2.54$ radians are considered in the event selection.

4.3.1 Background Rejection

At the $\Upsilon(4S)$ resonance it is particularly important to isolate τ pair events from the $e^+e^- \rightarrow e^+e^-$ Bhabha scattering background. The effective cross section for this process within the acceptance of the BaBar detector is $\sim$40nb [15] compared to 0.94nb [15] for τ pair events making Bhabha scattering the most severe source of background.

Continuum events, where an e^+e^- collision results in the production of a $u\overline{u}$, $d\overline{d}$, $s\overline{s}$, or $c\overline{c}$ quark pair also have a larger effective cross section (3.4nb) [15] within the acceptance of the BaBar detector than that for τ pair production and represent a significant source of background.

In addition to Bhabha and continuum events, the background from μ pair events has been studied. The effective cross section within the acceptance of the BaBar detector for the production of μ pairs is 1.16nb [15] which is comparable to the effective cross section for τ pair events. Several discriminating variables have been studied for the rejection of non-τ physics processes and are discussed in the following sections. Background studies have been carried out using simulated samples of Bhabha events, continuum ($u\overline{u}, d\overline{d}, s\overline{s}$) events, continuum $c\overline{c}$ events, μ pair events, and τ pair events. The BaBar detector was simulated using the Geant3 [37] based BBSIM [38] program.

4.3.1.1 Discriminating against Bhabha Events

The primary discriminating variable used for the rejection of Bhabha events is E/p, the ratio of the electromagnetic shower energy measured in the calorimeter to the track momentum measured by the tracking devices. Incident electrons are totally absorbed by the calorimeter depositing all of their energy in the form of an electromagnetic shower. The expected value for electrons therefore is E/p $\approx$1. Other particle types typically only deposit some fraction of their energy in the calorimeter leading to lower values of E/p. Figure 4-2 shows the E/p distribution for the charged track in the tagging hemisphere from (a) simulated τ pair events in which the τ in the tagging hemisphere decays via $\tau \rightarrow \rho\nu_\tau$ and (b) simulated Bhabha events. A clear electron peak can be seen at the expected value of E/p$\approx$1 in the distribution for the simulated Bhabha events which is well separated from the distribution for $\tau \rightarrow \rho\nu_\tau$ hemispheres where the charged track in the tagging hemisphere is a pion. The E/p distributions for the charged track in the tagging hemisphere from other simulated non-τ physics samples and from data events are shown in figure 4-3(a-d). The E/p distribution for continuum ($u\overline{u}, d\overline{d}, s\overline{s}$) events shown in figure 4-3(a) is difficult to distinguish from the distribution for $\tau \rightarrow \rho\nu_\tau$ hemispheres (figure 4-2(a)) since the charged particles produced in continuum events are predominantly pions. The distribution for $c\overline{c}$ continuum events shown in figure 4-3(b) is also similar due to the

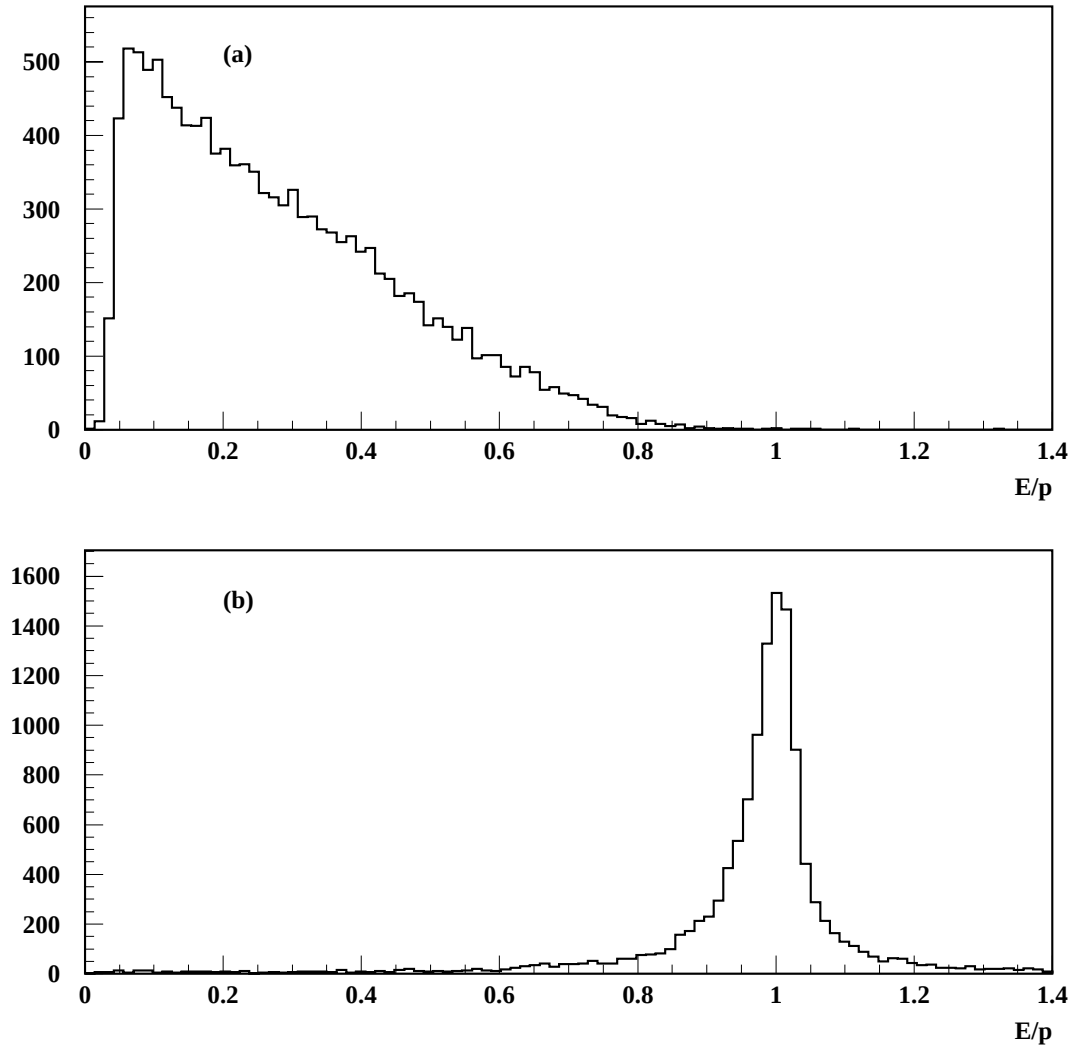

Figure 4-2. *E/p distributions for the charged track in the tagging hemisphere from (a) simulated τ pair events in which the τ in the tagging hemisphere decays via $\tau \rightarrow \rho\nu_\tau$ and (b) simulated Bhabha events.*

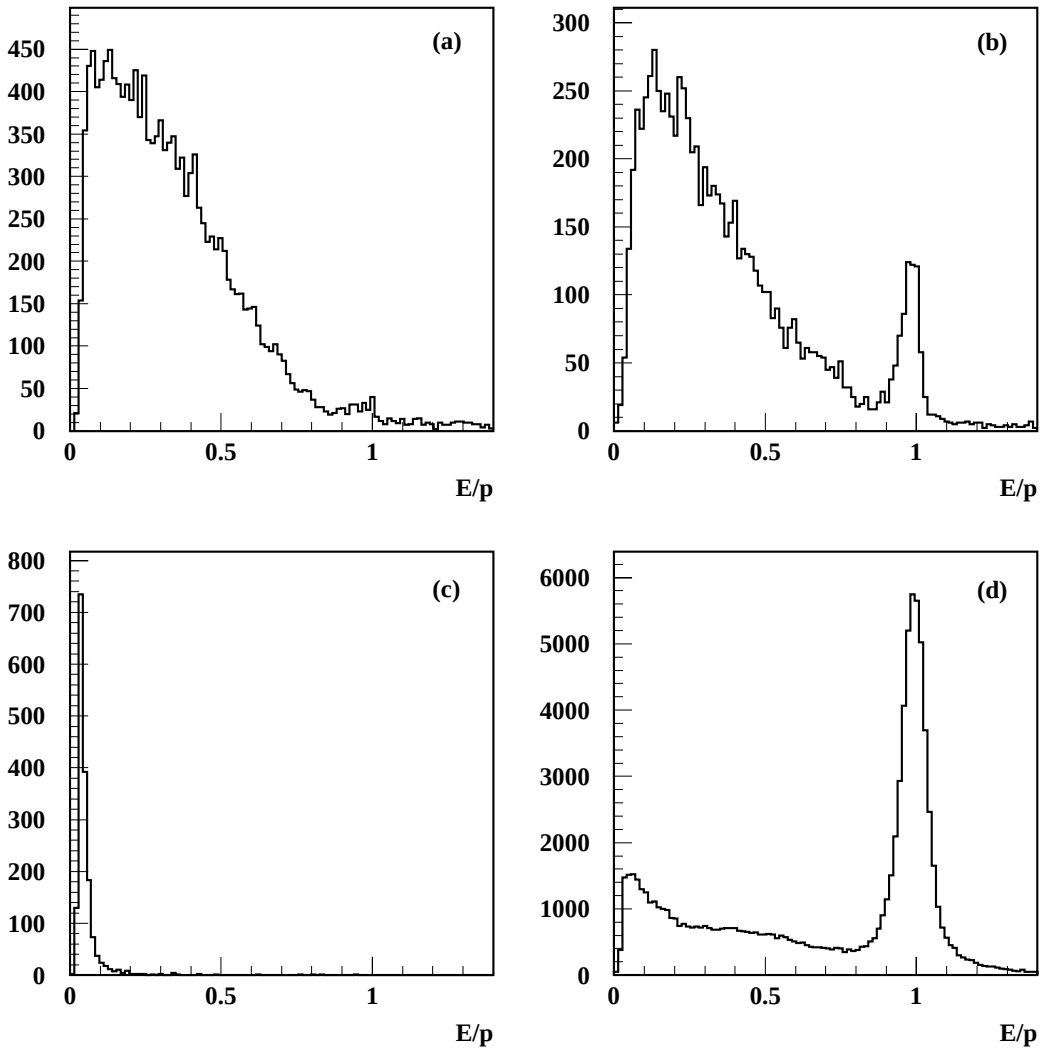

Figure 4-3. *E/p distributions for the charged track in the tagging hemisphere from (a) simulated continuum ($u\overline{u}$, $d\overline{d}$, $s\overline{s}$) events, (b) simulated continuum $c\overline{c}$ events, (c) simulated μ pair events, and (d) data events.*

production of charged pions in these events but exhibits an electron peak at E/p≈1. These electrons are produced in the decays of the heavier and shorter lived mesons produced in $c\overline{c}$ events. Muons deposit very little energy in the calorimeter which results in the low values of E/p illustrated by the distribution shown in figure 4-3(c). The very large electron peak in the distribution for data events shown in figure 4-3(d) demonstrates that Bhabha scattering is the dominant physics process.

The rate of energy loss through ionisation, dE/dx, on the charged track in the tagging hemisphere measured in the drift chamber also allows for discrimination between electrons from Bhabha events and charged pions from $\tau \rightarrow \rho\nu_\tau$ decays. For relativistic particles dE/dx varies as a function of velocity[2]. Since Bhabha electrons have greater velocity than the pions produced in $\tau \rightarrow \rho\nu_\tau$ decays, they are expected to have larger values of dE/dx. Figure 4-4 shows the dE/dx distributions for the charged track in the tagging hemisphere from simulated τ pair events in which the τ in the tagging hemisphere decays via $\tau \rightarrow \rho\nu_\tau$ and from simulated Bhabha events, illustrating the discrimination achievable in the drift chamber. There is some overlap in the distributions, but it can be seen that pions from $\tau \rightarrow \rho\nu_\tau$ decays typically have the expected lower values of dE/dx than electrons from Bhabha events.

Further Bhabha rejection may be achieved by cutting on the centre of mass momentum of the reconstructed ρ candidate in the tagging hemisphere (ρ reconstruction is discussed in section 4.3.3). In τ events the ρ momentum is dependent on the momentum of the undetected neutrino produced in the $\tau \rightarrow \rho\nu_\tau$ decay. In Bhabha events no neutrinos are produced so the momentum of the initial electron should be ≈5.3GeV/c, half the energy available in the centre of mass. Figure 4-5 shows the momentum distributions in the centre of mass for (a) true ρs reconstructed from simulated τ pair events and (b) reconstructed ρ candidates from simulated Bhabha events. The ρ candidate momentum distribution for

[2]The parameterisation of dE/dx for charged particles may be found in many physics texts, examples are [5, 12].

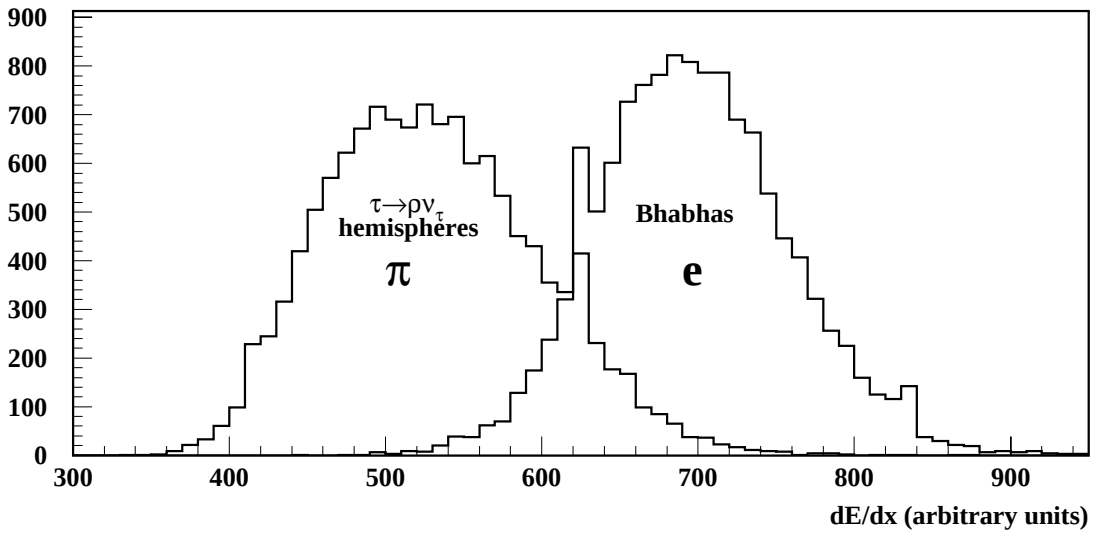

Figure 4-4. *dE/dx distributions for the charged track in the tagging hemisphere measured in the drift chamber from simulated τ pair events in which the τ in the tagging hemisphere decays via $\tau \rightarrow \rho\nu_\tau$ and from simulated Bhabha events.*

simulated Bhabha events shows the expected peak with a long low momentum tail. The reason for the tail is illustrated in figure 4-6 which shows the momentum distribution of the reconstructed ρ candidate in the centre of mass as a function of the polar angle of the charged track used in the ρ reconstruction from simulated Bhabha events. This indicates that the long tail is due to low angle electrons which lose momentum passing through a greater amount of detector material. The track polar angle distribution for Bhabha events is also strongly peaked towards low angles suggesting a cut on the ρ candidate momentum may be combined with a cut on the track polar angle to give improved Bhabha rejection. Figure 4-7 illustrates how the performance of a cut on the ρ candidate momentum varies when combined with different track polar angle cuts. The fraction of $\tau \rightarrow \rho\nu_\tau$ events retained after the cut is plotted against the fraction of Bhabha events rejected. Each line in the figure represents a different track polar angle cut, and the points along each line represent different values of a cut on the ρ candidate momentum for the given cut on the track polar angle. Points which fall in the region to the right of the line representing a

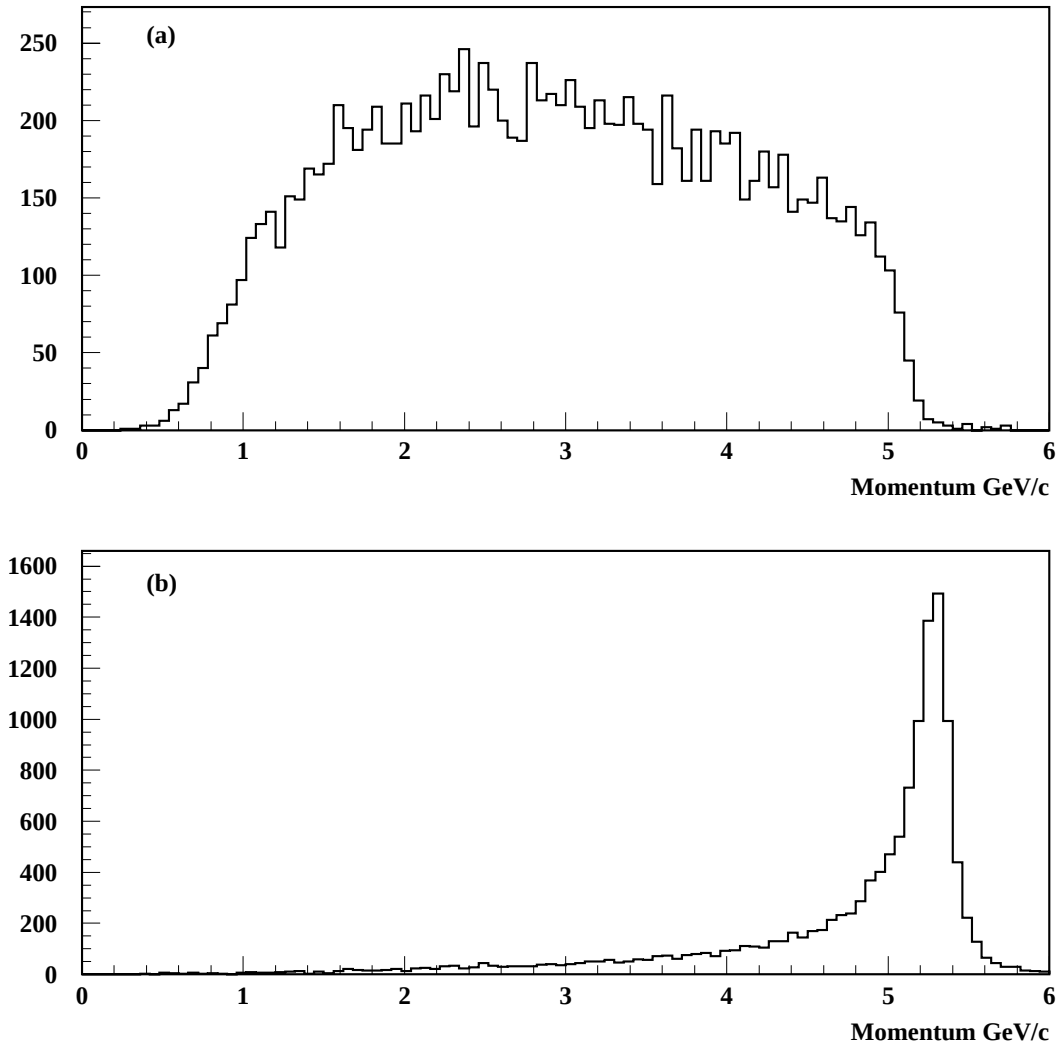

Figure 4-5. *Momentum distributions of the reconstructed ρ candidate in the centre of mass for (a) true ρs from simulated τ pair events and (b) simulated Bhabha events.*

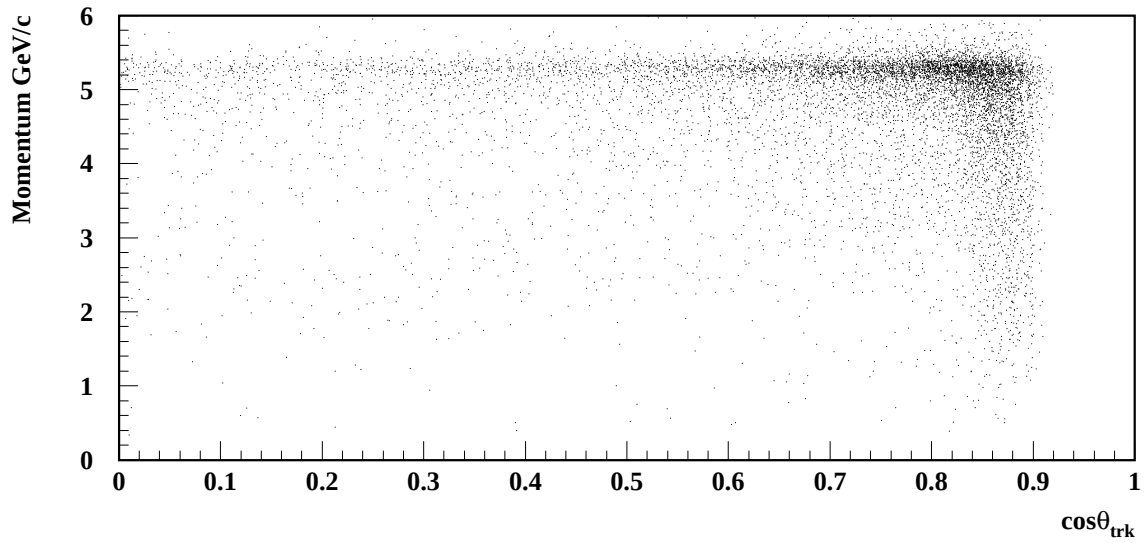

Figure 4-6. *Momentum distribution of the reconstructed ρ candidate in the centre of mass as a function of the polar angle of the charged track used in the ρ reconstruction from simulated Bhabha events.*

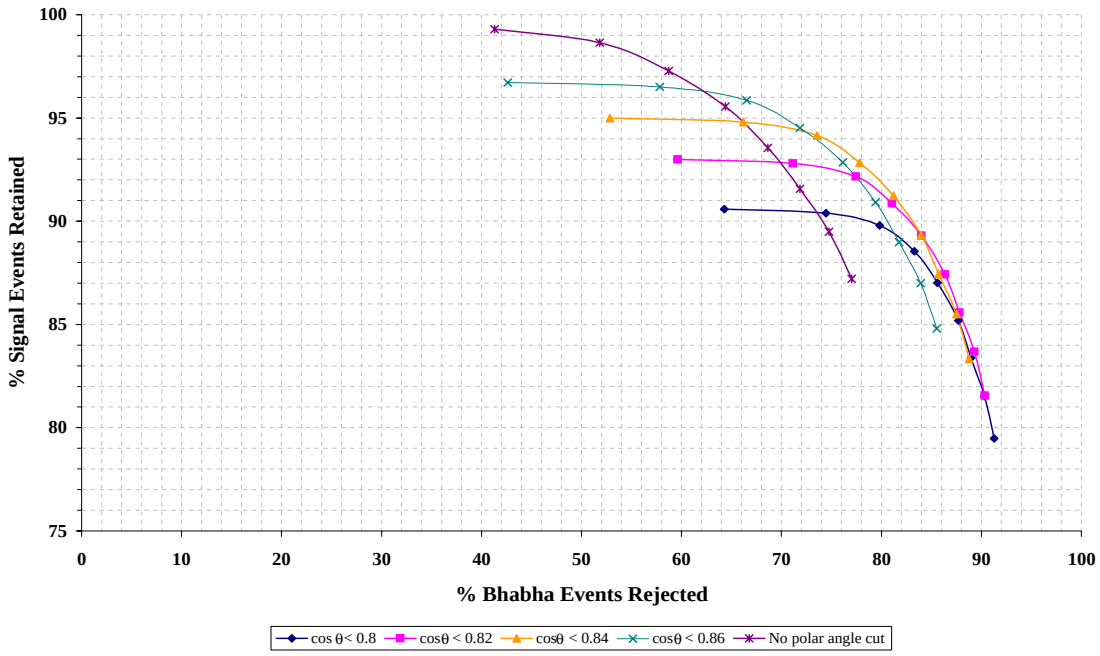

Figure 4-7. *Fraction of $\tau \rightarrow \rho\nu_\tau$ events retained after cutting on the centre of mass momentum of the reconstructed ρ candidate against the fraction of Bhabha events rejected for different track polar angle cuts.*

cut only on the ρ candidate momentum correspond to a combination of track polar angle and ρ candidate momentum cuts which give improved Bhabha rejection. We see that it is possible to choose a combination of cuts which will give an improvement in rejection with very little loss in signal retention.

The momentum distributions of the reconstructed ρ candidate in the centre of mass for other simulated non-τ physics samples are shown in figure 4-8(a-c). A comparison of the distributions in figures 4-8(a) and 4-8(b) with the distribution for $\tau \rightarrow \rho\nu_\tau$ hemispheres (figure 4-5(a)) shows this variable is not useful for discriminating against continuum events. However, the distribution for μ pair events shown in figure 4-8(c) is similar to that for Bhabha events (figure 4-5(b)) since again there are no undetected neutrinos, and the momentum of the initial μ should be $\approx$5.3GeV/c. This indicates that a cut on the ρ candidate momentum is also effective in discriminating against μ pair events.

Figure 4-9 shows a summary of the performance of the discriminating variables studied for the rejection of Bhabha events. For each variable, the fraction of signal $\tau \rightarrow \rho\nu_\tau$ events retained after the cut is plotted against the fraction of Bhabha events rejected. Each discriminating variable is represented by a coloured line with the points representing different cut values. The selection cuts which have been applied in the analysis are highlighted. An ideal selection cut would reject 100$\%$ of Bhabha events while retaining 100$\%$ of signal events and corresponds to a point in the top right hand corner of figure 4-9. The figure then indicates that E/p is the most effective discriminating variable. The point corresponding to a cut of E/p < 0.8 applied to the charged track in the tagging hemisphere is closest to the ideal value and rejects $\sim$92$\%$ of Bhabha events while retaining over 98$\%$ of $\tau \rightarrow \rho\nu_\tau$ events. In addition to the cut on E/p described above, a requirement on the centre of mass momentum to be $<$ 5.1GeV/c has been applied to the reconstructed ρ candidate. This cut also has very high signal retention while increasing the Bhabha rejection so that the combination of the applied cuts rejects over 97$\%$ of Bhabha events while retaining $\sim$97$\%$ of $\tau \rightarrow \rho\nu_\tau$ events. This is illustrated graphically in figure 4-10

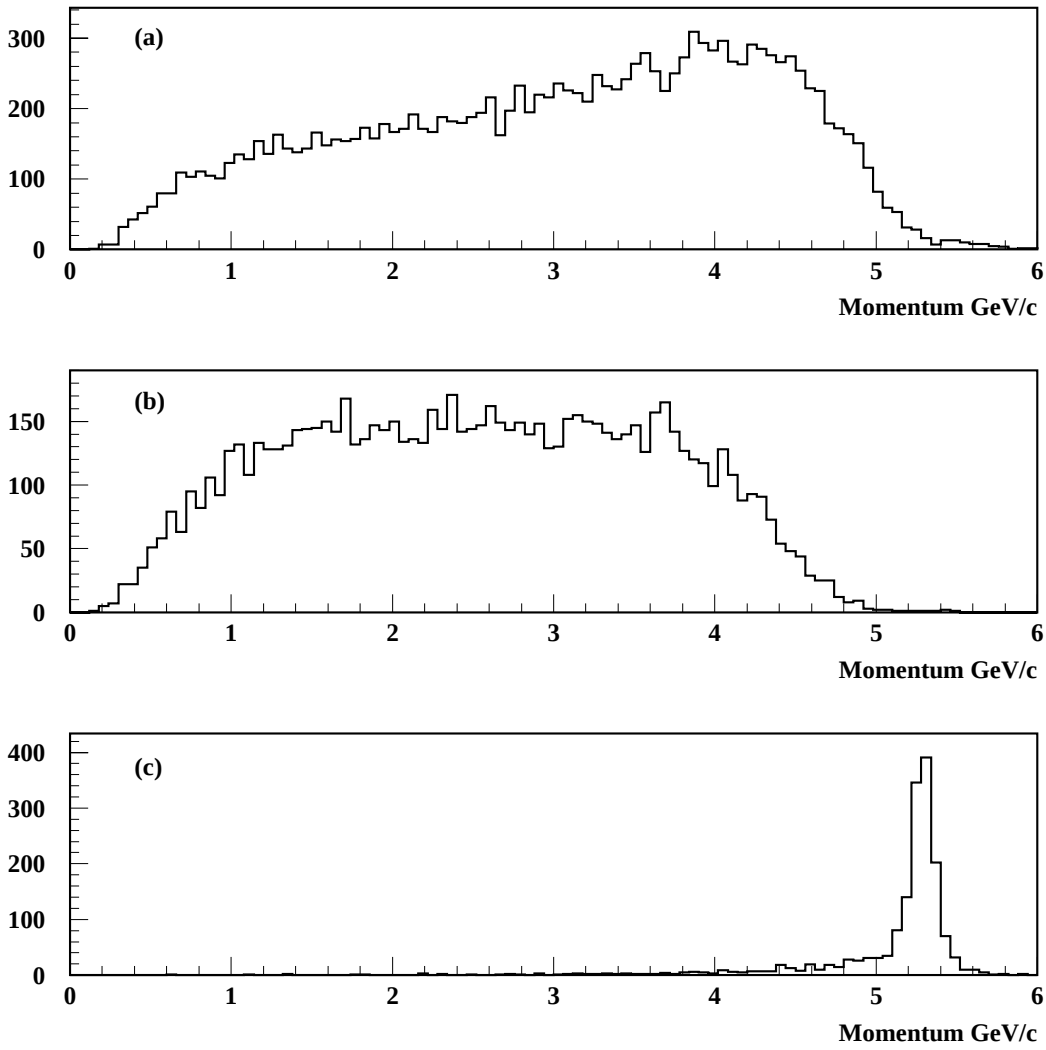

Figure 4-8. *Momentum distributions of the reconstructed ρ candidate in the centre of mass for simulated (a) continuum ($u\overline{u}, d\overline{d}, s\overline{s}$) events, (b) continuum $c\overline{c}$ events, and (c) μ pair events.*

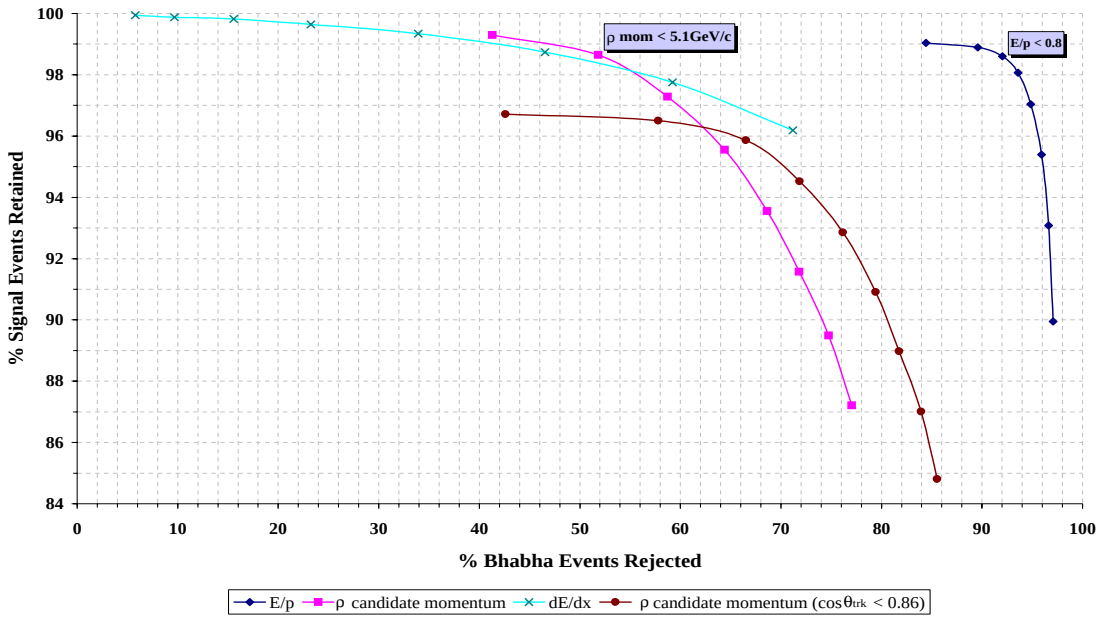

Figure 4-9. *Fraction of $\tau \rightarrow \rho\nu_\tau$ events retained against the fraction of Bhabha events rejected for different cut values of discriminating variables studied for the rejection of Bhabha events. Cuts which have been applied in the analysis are highlighted.*

which shows the ρ candidate momentum in the centre of mass against E/p for the charged track in the tagging hemisphere from simulated τ pair events in which the charged track in the tagging hemisphere decays via $\tau \rightarrow \rho\nu_\tau$ and from simulated Bhabha events. The applied cuts are indicated by the dashed lines.

4.3.1.2 Discriminating against Continuum Events

The requirement of a single track in the tagging hemisphere suppresses the background from continuum events. However, even with this requirement continuum events are still a significant source of background. Further reduction may be obtained by cutting on the reconstructed invariant mass of the hemisphere opposite to the hemisphere used to tag the event. For τ hemispheres, the reconstructed invariant mass is expected to be less than 1.8GeV/c^2, the mass of the τ, since neutrinos are produced in τ decays which are not

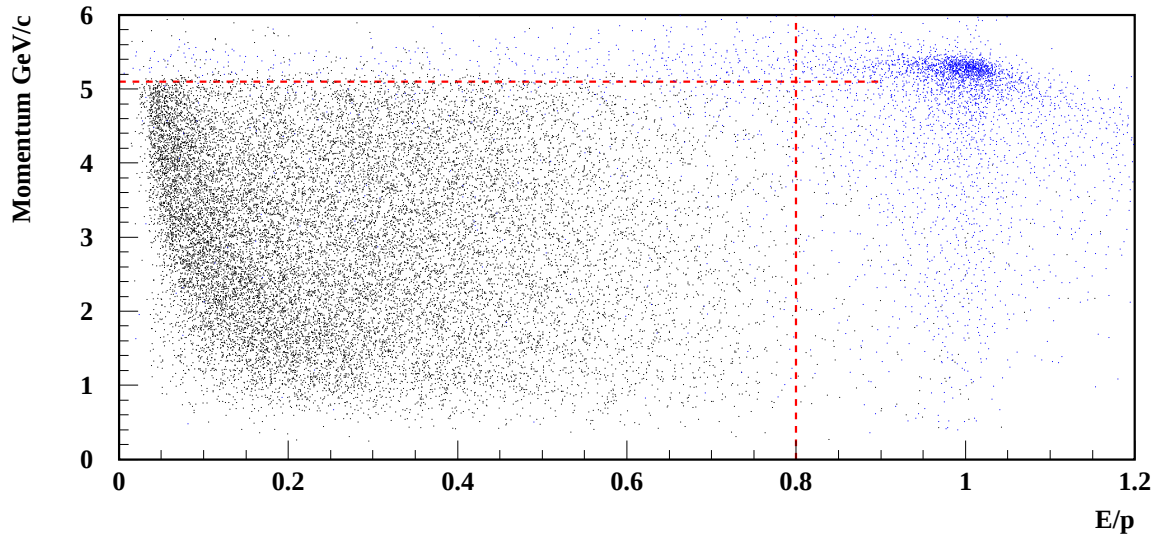

Figure 4-10. *Momentum distribution of the reconstructed ρ candidate in the centre of mass as a function of E/p for the charged track in the tagging hemisphere from simulated τ pair events (black) and from simulated Bhabha events (blue).*

detected and carry off some fraction of the τ's energy. The invariant mass distributions for the hemisphere opposite to the hemisphere used to tag the event from simulated τ pair events, simulated continuum ($u\overline{u}, d\overline{d}, s\overline{s}$), and simulated continuum $c\overline{c}$ events are shown in figure 4-11(a-c). The distribution for simulated τ pair events shown in figure 4-11(a) extends up to the τ mass as expected and exhibits a large spike at the charged pion mass. These are events where the hemisphere contains only a single charged track which, since no particle identification has been carried out, has the pion mass assigned to its four-vector. A large spike is expected since the one prong mode (see Appendix A) is by far the most common topology for τ decays. The distributions for both types of continuum events shown in figures 4-11(b) and 4-11(c) are very similar in shape and extend well beyond the distribution for τ hemispheres. Figure 4-12 shows the performance of this cut for continuum ($u\overline{u}, d\overline{d}, s\overline{s}$) and continuum $c\overline{c}$ events. The fraction of $\tau \to \rho\nu_\tau$ events retained after the cut is plotted against the fraction of continuum events rejected. Each type of continuum is represented by a coloured line with the points representing different

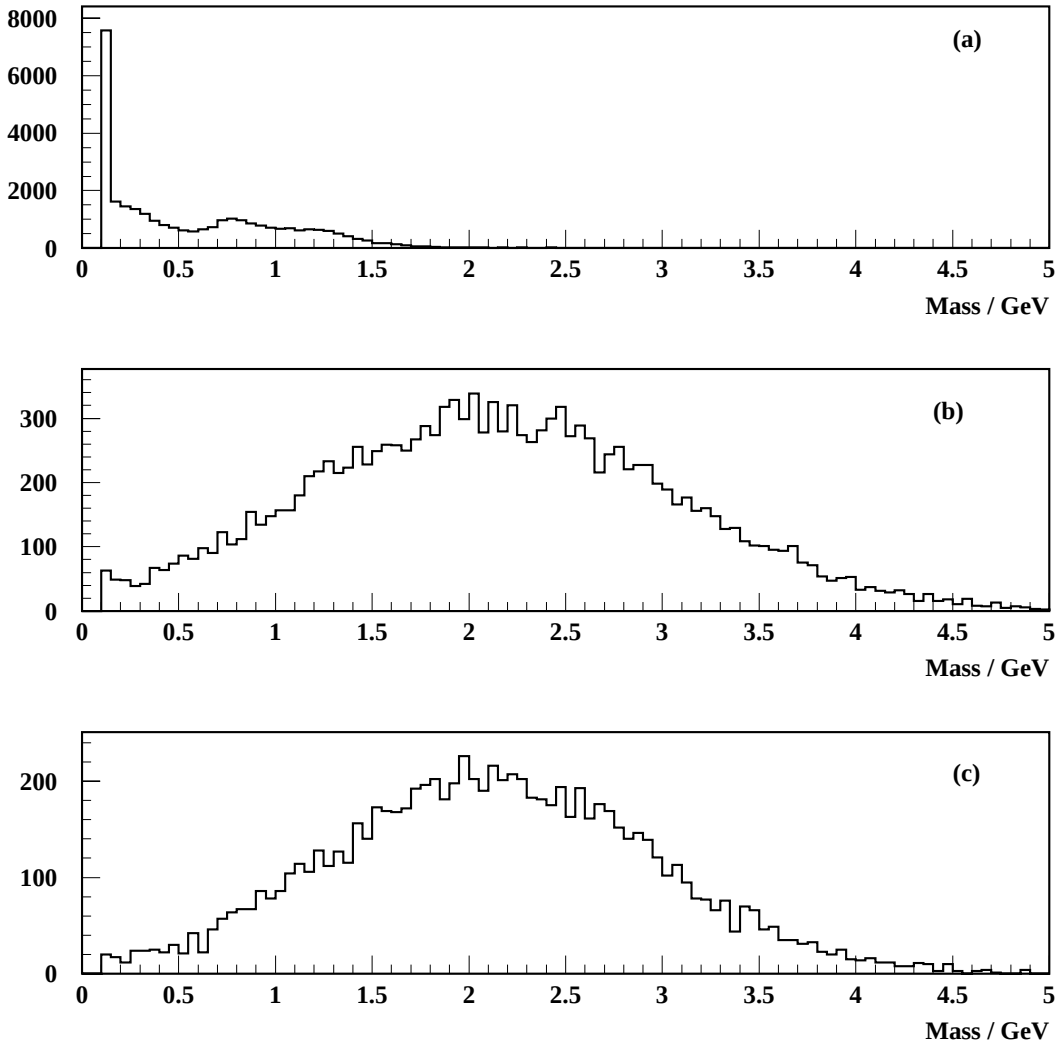

Figure 4-11. *Invariant mass distributions for the hemisphere opposite the hemisphere used to tag the event from simulated (a) τ pair events, (b) continuum ($u\overline{u}, d\overline{d}, s\overline{s}$) events, and (c) continuum $c\overline{c}$ events.*

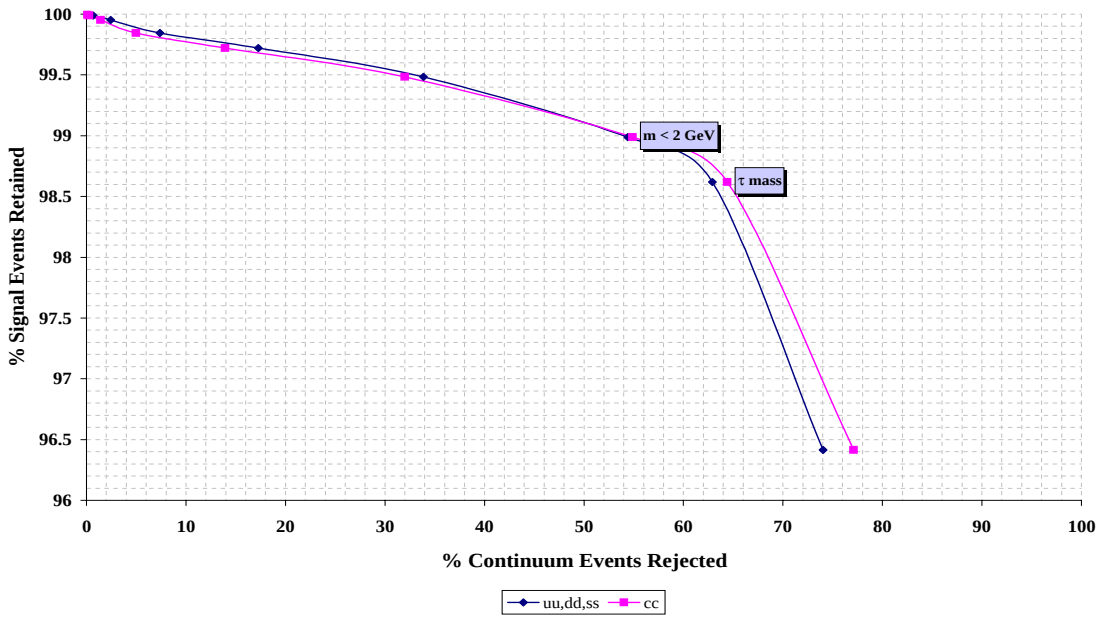

Figure 4-12. *Fraction of $\tau \rightarrow \rho\nu_\tau$ events retained against the fraction of continuum events rejected for different cut values of the invariant mass of the hemisphere opposite to the hemisphere used to tag the event.*

cut values. The hemisphere in question is the hemisphere on which the branching ratio measurement is made. It is therefore important that a cut on the reconstructed invariant mass of this hemisphere does not bias the final τ sample. In principle the hardest cut which could be made without introducing a bias to the τ sample would be at 1.78GeV/c^2, the τ mass, highlighted in the figure. However in practice, the thrust axis may not always cleanly divide the event, hence to minimise the risk of bias the cut applied is set slightly above the τ mass at 2GeV/c^2 which rejects $\sim$54$\%$ of both continuum ($u\overline{u}, d\overline{d}, s\overline{s}$) and continuum $c\overline{c}$ events while retaining $\sim$99$\%$ of $\tau \rightarrow \rho\nu_\tau$ events.

A second measure which may be implemented for the rejection of continuum events is the definition of a cone about the thrust axis inside the tagging hemisphere with only events contained inside the cone considered in the event selection. Continuum events will typically produce several particles which spread out over a wider area compared with the more collimated $\tau \rightarrow \rho\nu_\tau$ events. The effect of introducing cones of different half

angles combined with a cut of 2GeV/c^2 on the invariant mass of the opposite hemisphere is illustrated in figure 4-13. The fraction of $\tau \rightarrow \rho\nu_\tau$ events retained after the cut is plotted

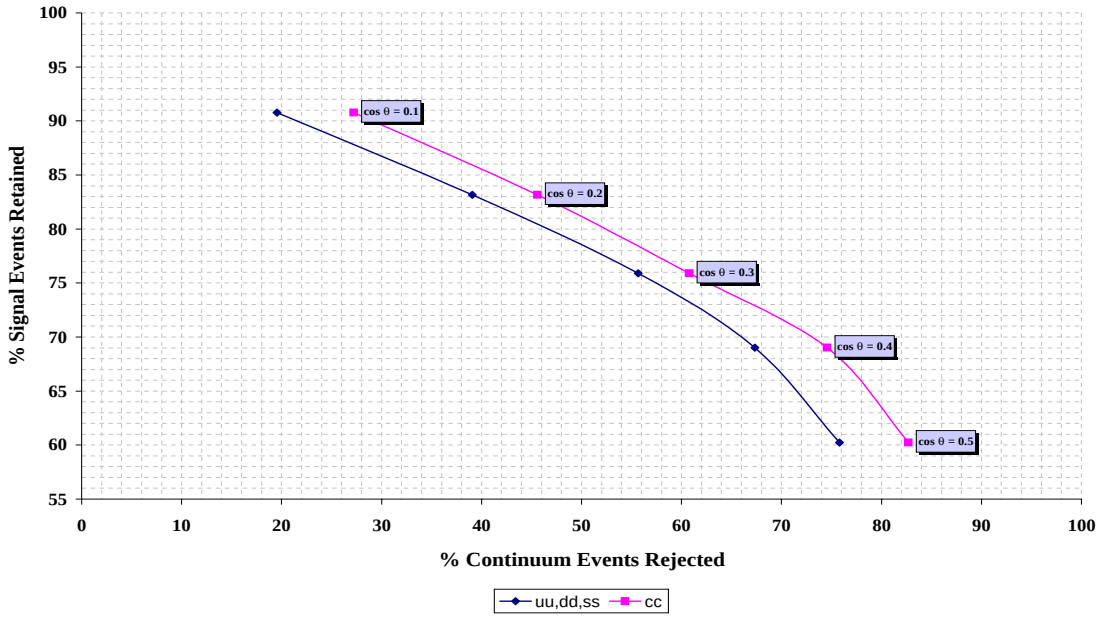

Figure 4-13. *Fraction of $\tau \rightarrow \rho\nu_\tau$ events retained against the fraction of continuum events rejected for cones of different half angles inside the tagging hemisphere. A cut of $m < 2GeV/c^2$ is applied to the opposite hemisphere.*

against the fraction of continuum events rejected. Each type of continuum is represented by a coloured line with the points representing cones of different half angle. It is clear that the definition of even a wide cone has a significant impact on signal efficiency and this cut has not been implemented.

4.3.2 π^0 Reconstruction

The presence of a π^0 in the final state of the $\tau \rightarrow \rho\nu_\tau$ mode makes π^0 reconstruction an important factor in this analysis. The efficiency for π^0 reconstruction also provides an indication of the performance of the electromagnetic calorimeter.

The momentum spectrum for π^0s produced in $\tau \rightarrow \rho\nu_\tau$ decays from simulated τ pair events in which both τs are allowed to decay generically is shown in figure 4-14. The

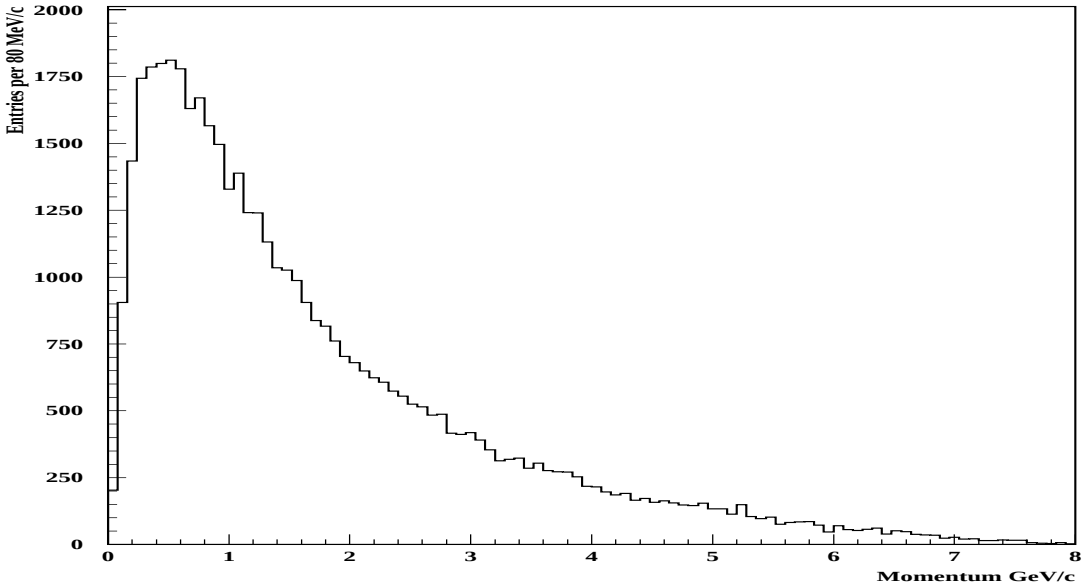

Figure 4-14. *Momentum spectrum of π^0s produced in the $\tau \rightarrow \rho\nu_\tau$ decay channel from simulated generic τ pair events.*

spectrum indicates these π^0s have high momentum which can reach 7 - 8GeV/c and a significant fraction have momentum greater than 1.5GeV/c. The high momentum of π^0s has an effect on the efficiency for π^0 reconstruction since the π^0 decays into a pair of photons before reaching the calorimeter and the opening angle of these photons is momentum dependent. Figure 4-15 shows how the opening angle of the daughter photons from the π^0 decay decreases as the π^0 momentum increases. For π^0s with momentum above about 1.5GeV/c, indicated by the dashed line in the figure, the small opening angle usually results in the corresponding neutral energy deposits in the calorimeter being so close together that they merge to form a single neutral cluster with either one or two local maxima corresponding to the point of entry of the incident photons. Only one local maxima is produced in the case where both photons directly overlap, entering the

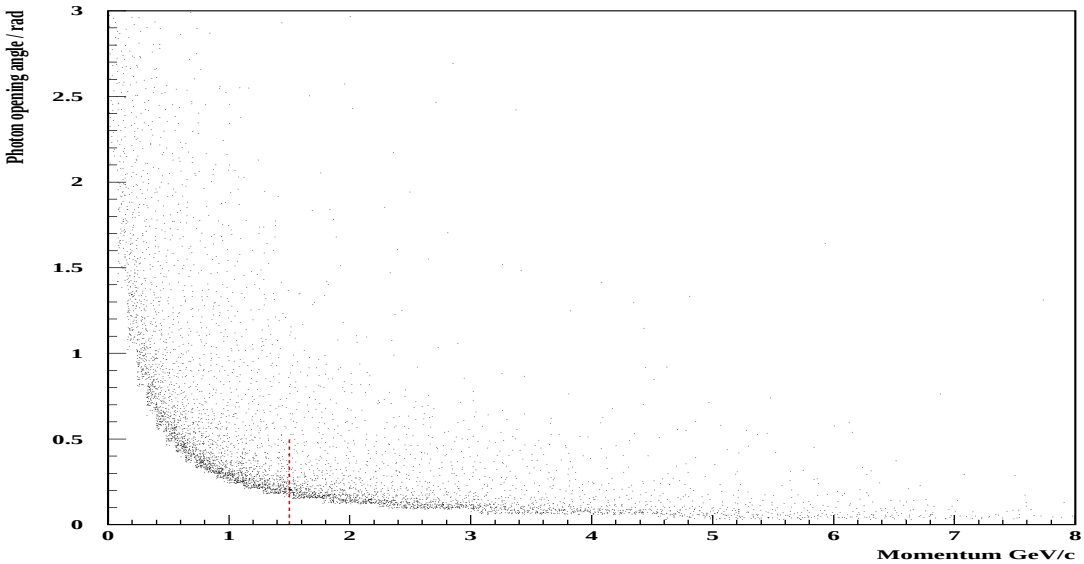

Figure 4-15. *Opening angle of photons produced in the decay $\pi^0 \rightarrow \gamma\gamma$ for π^0s produced in $\tau \rightarrow \rho\nu_\tau$ decays as a function of π^0 momentum. The dashed line indicates the momentum above which the photons may produce merged clusters in the calorimeter.*

calorimeter at the same point. The fraction of π^0s from $\tau \rightarrow \rho\nu_\tau$ decays producing merged clusters is estimated from simulated generic τ pair events to be $\sim$23% consisting of $\sim$6% of π^0s producing clusters with a single maxima and $\sim$17% of π^0s producing clusters with two maxima.

Only one π^0 candidate is constructed in the tagging hemisphere for each event by combining the four-vectors of all neutrals with energy greater than 60MeV. For those neutral clusters which contain more than one local maxima, each region of maxima is treated as a separate neutral candidate when combining four-vectors. In this way most merged π^0s may be reconstructed. Only those where both photons overlap to form a single local maxima inside the cluster will be rejected.

Figure 4-16 shows the distribution for the invariant mass of neutral calorimeter clusters in the tagging hemisphere from data events (points) and simulated events (histogram). The

normalisation for the simulated events has been determined from the ρ mass normalisation described in section 4.3.3. The distribution shows a peak at the π^0 mass. The shaded regions indicate the background contributions from τ pair events and non-τ events. The dark shaded region shows the contribution from τ pair events in which the τ in the tagging hemisphere decays via $\tau \rightarrow \rho\nu_\tau$ in which the π^0 has not been correctly reconstructed. This is primarily due to the existence of additional neutral clusters known as 'splitoffs' produced by the interaction of the charged pion from the ρ decay in the calorimeter. Additional neutral clusters may also be caused by initial state radiation photons. The lighter shaded region above shows the contribution from τ pair events in which the τ in the tagging hemisphere decays via any channel other than $\tau \rightarrow \rho\nu_\tau$. Some of these channels contain π^0s (see Appendix A) which results in the peak at the π^0 mass in this distribution. The lightest shaded region shows the contribution from non-τ events. This distribution also exhibits a peak at the π^0 mass due to π^0s produced in continuum events. The figure also shows a clear tail on the low mass side of the signal π^0 peak. This is attributed to incomplete energy deposits in the calorimeter due to energy leakage from the calorimeter crystals and photon conversions in the detector material in front of the calorimeter [18, 40]. There is some disagreement between the data and simulation distributions on either side of the peak, particularly on the high mass side. This disagreement is not currently understood. A cut is applied on the neutral invariant mass of $0.11 < M_{neut} < 0.155$ GeV/c^2 about the π^0 peak. There is relatively good agreement between the data and simulation in this region.

4.3.2.1 π^0 Reconstruction Efficiency

The efficiency for the reconstruction of π^0s produced in $\tau \rightarrow \rho\nu_\tau$ decays has been measured using simulated generic τ pair events and is defined as:

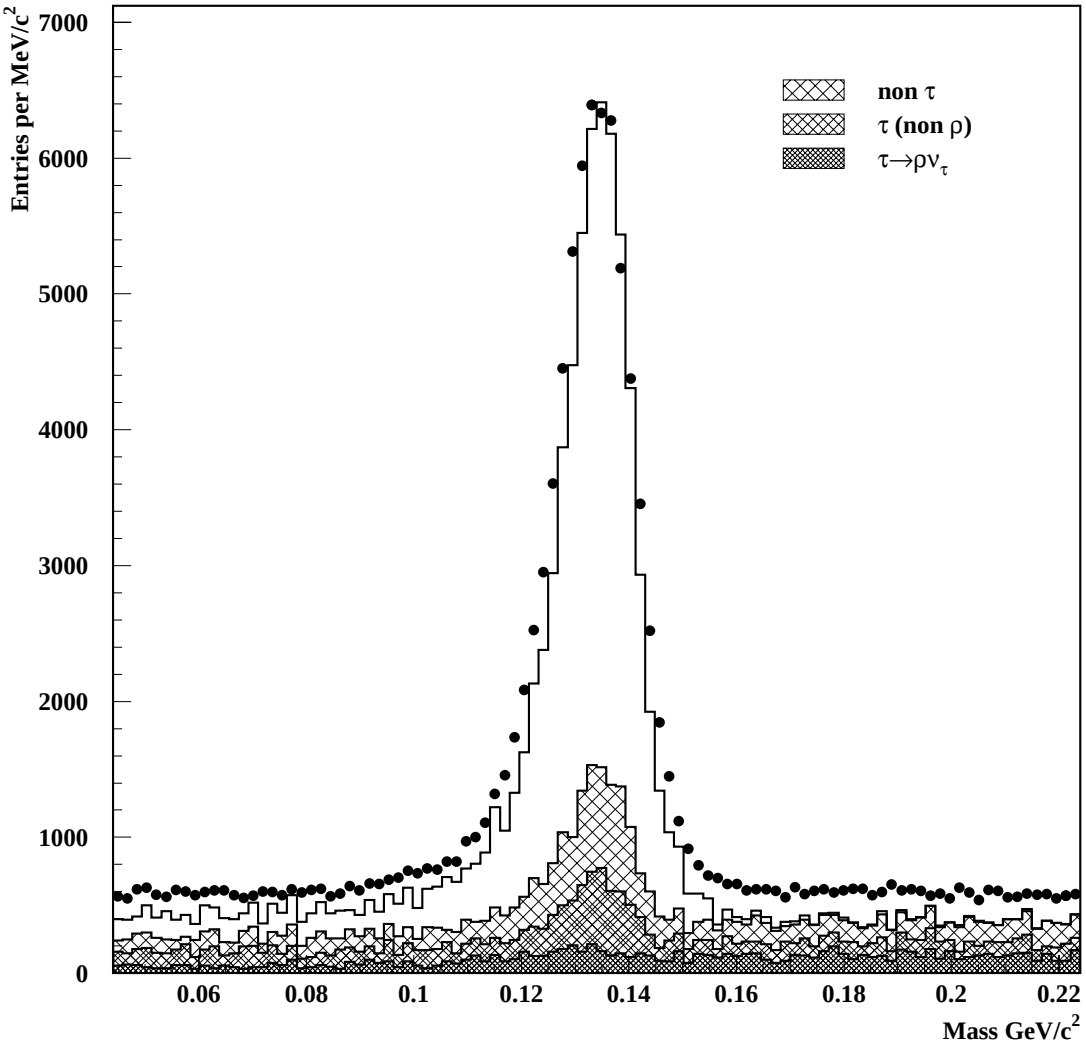

Figure 4-16. *Invariant mass distribution of neutral calorimeter clusters in the tagging hemisphere from data (points) and from simulated events (histogram). The shaded regions indicate different background contributions.*

$$\epsilon_{\pi^0} = \frac{N_{\pi^0}}{N_{\pi^0}^{true}} \tag{4.1}$$

where N_{π^0} is the number of π^0s correctly reconstructed from $\tau \to \rho\nu_\tau$ decays and $N_{\pi^0}^{true}$ is the number of π^0s from $\tau \to \rho\nu_\tau$ decays in the simulation sample. A summary of the signal π^0 efficiency is shown in table 4-1.

Selection Cut	**% π^0s from $\tau \to \rho\nu_\tau$ decays passing cut**	**Cut Efficiency %**
-	100	-
Acceptance cuts	80.9	80.9
Tagging hemisphere N_{trk} = 1, $N_{neutrals} \geq 1$	58.0	71.7
Opposite hemisphere $N_{trk} \geq 1$	47.9	82.6
Background rejection cuts	43.6	91.0
$0.11 < M_{neut} < 0.155$ GeV/c^2	20.3	46.6

Table 4-1. *Summary of signal π^0 efficiency for selection cuts.*

Approximately 19% of signal π^0s fall outside the acceptance cuts defined for the analysis or outside of the calorimeter acceptance. A large drop is then observed in the number of signal π^0s which pass the tagging hemisphere requirements. The principal reason for this is the requirement of exactly one track in the tagging hemisphere. This requirement results in losses from tracks falling outside the acceptance cuts and from the rejection of conversion events where photons produced in the π^0 decay convert into an electron-positron pair inside the detector producing additional tracks. The cut efficiency for the tagging hemisphere requirements indicates 28.3% of signal π^0s remaining before this selection cut are rejected. Events where the tagging hemisphere contains additional tracks account for the rejection of 15.7%, over half of the efficiency loss for this cut. The fraction of photons, f_γ, which convert before detection in the calorimeter is dependent on the amount of material in front of the calorimeter [18] and is given by:

$$f_\gamma = 1 - e^{-\frac{7x}{9X_0}} \tag{4.2}$$

where x is the thickness of material traversed, and X_0 is one radiation length. The amount of material in front of the barrel section of the calorimeter is approximately [18] $0.23X_0/\sin\theta$. A photon must convert inside or before the tracking devices to produce additional tracks which corresponds to a photon traversing up to $\sim$25% of the material in front of the calorimeter. Using equation (4.2) this indicates $\sim$4.4% of photons convert in the tracking devices at 90°. Two photons are produced in the π^0 decay, and this corresponds to a photon conversion in at least 8.6% of signal π^0 decays. This is in agreement with the observed loss of 15.7% due to conversions. A further large efficiency loss is observed after cutting on the invariant mass of neutrals in the tagging hemisphere. This arises because of the low mass tail in the signal π^0 distribution, and incorrectly reconstructed π^0s due to the presence of splitoffs, illustrated in figure 4-16. Table 4-1, indicates 20.3% of signal π^0s pass the selection cuts. Not all of these are correctly reconstructed, corresponding to the dark shaded region in figure 4-16 described in the previous section, and the final π^0 reconstruction efficiency is estimated to be (19.1 $\pm$ 0.2)%. Future analyses will benefit from improvements in the algorithms for neutral reconstruction in the calorimeter which will lead to improvements in the π^0 reconstruction efficiency.

4.3.3 ρ Reconstruction

A ρ candidate is constructed inside the tagging hemisphere for each event by combining the four-vectors of neutrals with energy greater than 60MeV with the four-vector of the single charged track. Figure 4-17 shows the distribution for the invariant mass of reconstructed ρ candidates from data events (points) and from simulated events (histogram) after the applied cuts for background rejection and on the invariant mass of neutrals in the tagging hemisphere. At this stage in the BaBar experiment, the exact luminosities of simulated event samples are not available to determine the correct normalisation. Here,

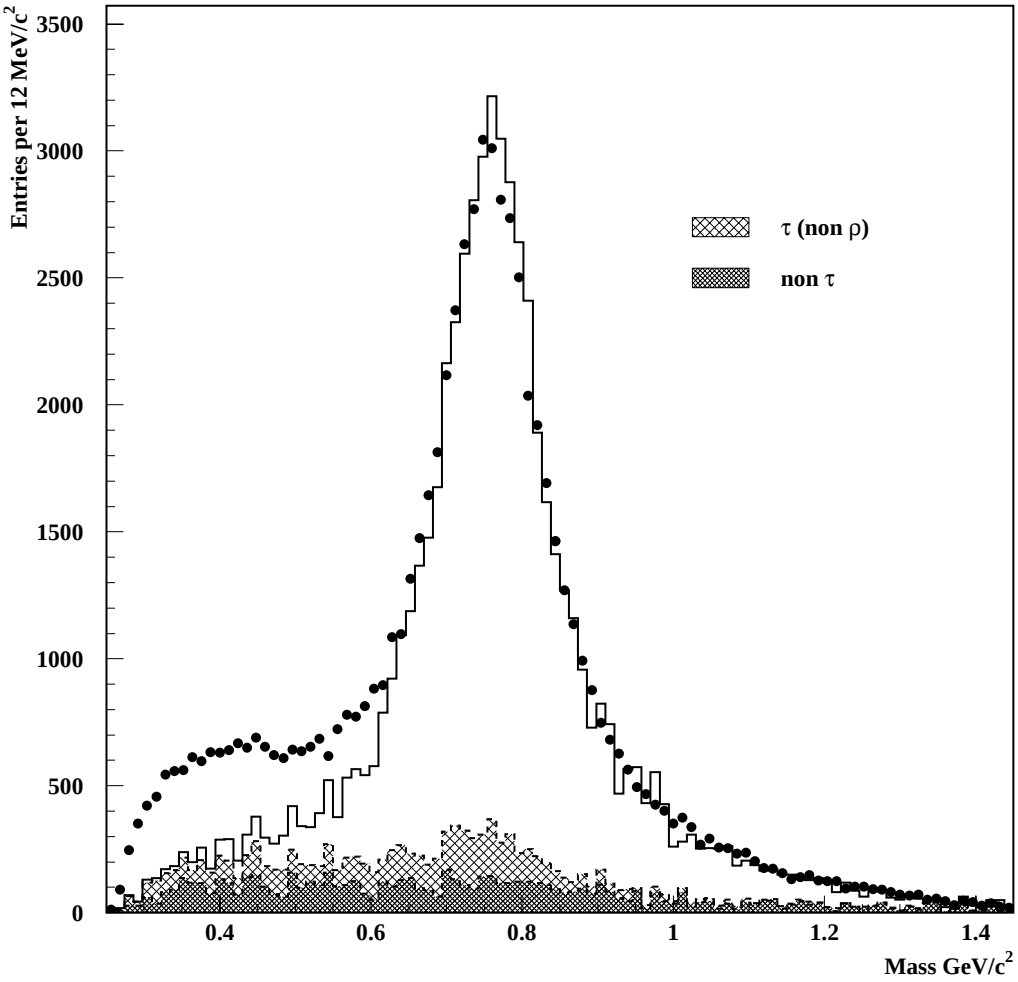

Figure 4-17. *Invariant mass distribution of reconstructed ρ candidates in the tagging hemisphere from data events (points) and from simulated events (histogram). The shaded regions indicate different background contributions predicted from simulated events. The data is not well modelled by the simulation on the low mass side of the peak.*

the simulated events have been fitted to the data distribution within the mass limits 0.65 $< M_\rho <$ 0.95 GeV/c^2 after background subtraction to provide the normalisation. The figure shows a peak at the ρ mass on top of a background distribution. The shaded regions indicate the different physics backgrounds predicted from simulated events. The dark shaded region shows the contribution from non-τ events. These are predominantly continuum events in which a π^0 has been reconstructed in the tagging hemisphere. The lighter shaded region shows the contribution from τ pair events in which the τ in the tagging hemisphere decays via any channel other than $\tau \to \rho\nu_\tau$. There is some evidence of a small number of ρ events in this distribution. These are most likely to be from τs which decay to a charged and a neutral pion through the ρ and one or more additional π^0s.

The data is not well modelled by the simulation on the low mass side of the peak. A similar discrepancy in this distribution has been observed elsewhere [41]. Figure 4-18 shows the momentum distribution of reconstructed ρ candidates in the centre of mass from data events with the momentum distribution of ρ candidates from data events in the low mass region of disagreement ($M_\rho <$ 0.5 GeV/c^2) in figure 4-17 superimposed. A comparison with ρ candidate momentum distributions from simulated events (see figures 4-5 and 4-8) indicates that a peak at low momentum is only seen in the data events. This characteristic suggests the presence of an additional background not considered in this analysis. This background is not currently understood and its contribution under the ρ mass peak is not known. In order to suppress this background an additional requirement has been introduced to reject reconstructed ρ candidates with centre of mass momentum less than 1.5 GeV/c. Figure 4-19 shows the distribution for the invariant mass of reconstructed ρ candidates from data events (points) and from simulated events (histogram) after this additional requirement has been made. The simulation is now seen to be in good agreement with the data.

A cut is applied on the ρ candidate invariant mass of 0.6 $< M_\rho <$ 0.95 GeV/c^2 about the ρ mass peak.

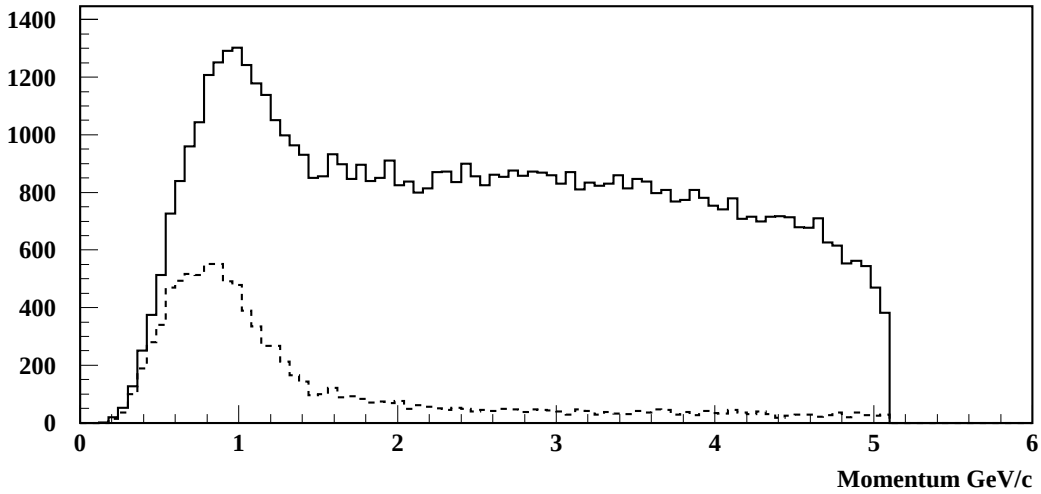

Figure 4-18. *Momentum distribution in the centre of mass of reconstructed ρ candidates from data events. The dashed line indicates ρ candidates in the low mass region ($M_\rho < 0.5$ GeV/c^2) of figure 4-17. The distributions show a peak below about 1.5 GeV/c which is not seen in the simulated event samples.*

4.4 Performance of Event Selection Method

A sample of 38027 data events passed all of the event selection cuts. The performance of the event selection is discussed in this section in terms of the efficiency for selecting $\tau \to \rho\nu_\tau$ events, the purity of the $\tau \to \rho\nu_\tau$ sample, and the bias to the τ sample on which the branching ratio measurement is made.

4.4.1 Efficiency for Selection of $\tau \to \rho\nu_\tau$ Events

The efficiency for the selection of τ pair events through reconstruction of the $\tau \to \rho\nu_\tau$ channel has been measured using simulated generic τ pair events and is defined as

$$\epsilon_{\tau\to\rho\nu_\tau} = \frac{N_{\tau\to\rho\nu_\tau}}{N^{true}_{\tau\to\rho\nu_\tau}} \tag{4.3}$$

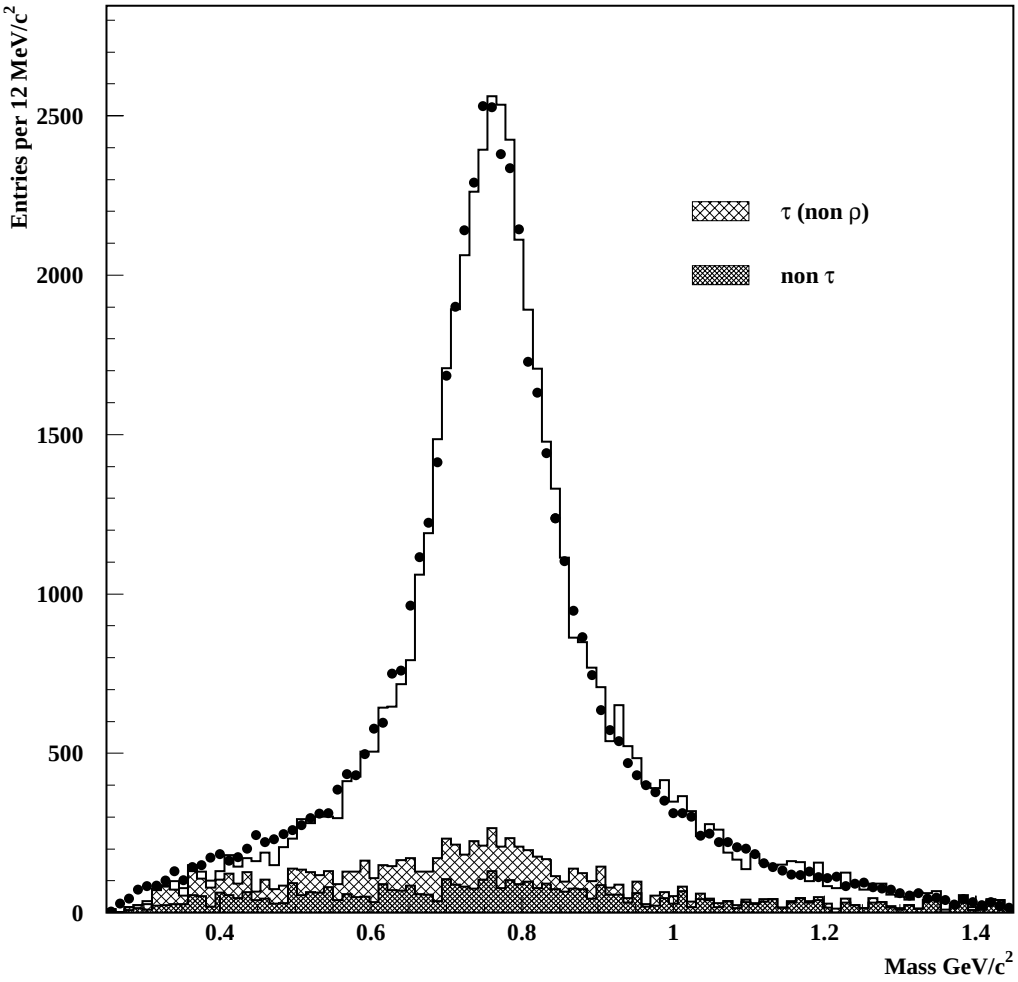

Figure 4-19. *Invariant mass distribution of reconstructed ρ candidates in the tagging hemisphere from data events (points) and from simulated events (histogram). The shaded regions indicate different background contributions predicted from simulated events. The simulation is in good agreement with the data.*

where $N_{\tau\to\rho\nu_\tau}$ is the number of $\tau \to \rho\nu_\tau$ events passing the event selection, and $N^{true}_{\tau\to\rho\nu_\tau}$ is the number of $\tau \to \rho\nu_\tau$ events in the simulation sample. A summary of the efficiency for selection of $\tau \to \rho\nu_\tau$ events is given in table 4-2. The large drops in efficiency

Selection Cut	**% $\tau \to \rho\nu_\tau$ Events Passing Cut**	**Cut Efficiency %**
-	100	-
Acceptance cuts	82.2	82.2
Tagging hemisphere N_{trk} = 1, $N_{neutrals} \geq 1$	64.1	78.0
Opposite hemisphere $N_{trk} \geq 1$	51.3	80.0
Background rejection cuts	45.1	87.9
$0.11 < M_{neut} < 0.155$ GeV/c^2	20.4	45.3
$0.6 < M_\rho < 0.95$ GeV/c^2	17.0	83.3

Table 4-2. *Summary of efficiency for selection of $\tau \to \rho\nu_\tau$ events.*

resulting from the tagging hemisphere requirements and neutral invariant mass cut are due to the issues relating to the π^0 reconstruction efficiency discussed in section 4.3.2.1. The final efficiency for selecting $\tau \to \rho\nu_\tau$ events is $(17.0 \pm 0.2)\%$ where the error shown is statistical.

4.4.2 Bias to the τ Sample

The aim of the event selection is to produce as far as possible an unbiased sample of τs on which to make the leptonic branching ratio measurement. A bias factor has been defined to measure the extent to which the event selection preferentially selects leptonic decays in the hemisphere on which the measurement is made.

$$f_{bias} = \frac{\epsilon_{\tau\to all,\tau\to\rho}}{\epsilon_{\tau\to l,\tau\to\rho}} \tag{4.4}$$

where $\epsilon_{\tau\to all,\tau\to\rho}$ is the efficiency for selecting $\tau \to \rho\nu_\tau$ events where the remaining τ is in the opposite hemisphere and may decay to any channel, and $\epsilon_{\tau\to l,\tau\to\rho}$ is the efficiency for

selecting $\tau \to \rho\nu_\tau$ events in which the other τ is in the opposite hemisphere and decays leptonically. These efficiencies have been measured using simulated τ pair events. The efficiency $\epsilon_{\tau\to l,\tau\to\rho}$ has been measured to be $\epsilon_{\tau\to e,\tau\to\rho}$ = (26.5 $\pm$ 0.6)% where the leptonic decay is via the $\tau \to e\nu_e\nu_\tau$ channel, and $\epsilon_{\tau\to\mu,\tau\to\rho}$ = (26.6 $\pm$ 0.6)% where the leptonic decay is via the $\tau \to \mu\nu_\mu\nu_\tau$ channel. The efficiency $\epsilon_{\tau\to all,\tau\to\rho}$ has been measured to be (26.1% $\pm$ 0.3)%. The errors quoted on the efficiencies are the statistical uncertainties. Inserting these values into equation (4.4), the bias factor is found to be 0.99 $\pm$ 0.02 for the $\tau \to e\nu_e\nu_\tau$ channel, and 0.98 $\pm$ 0.02 for the $\tau \to \mu\nu_\mu\nu_\tau$ channel. The measured values indicate that the event selection may introduce a small bias to the τ sample by preferentially selecting leptonic decays. However, both results are also consistent with a bias factor of zero, and greater precision is required before a firm statement can be made. If a bias has been introduced, this is likely to be due to the kinematic differences between the leptonic modes which are three-body decays, and two-body modes such as $\tau \to \pi\nu_\tau$. The event selection relies on cleanly dividing the event into hemispheres in the centre of mass. The higher momentum of charged particles produced in two-body τ decays compared with three-body decays could make them more likely to stray into the opposite side of the event, increasing the chances of the event being rejected. A correction for the measured bias is made in extracting the branching ratio measurements.

4.4.3 Check of Background Contamination to the τ Sample

The selected sample of ρ tagged τ pair events in the data has some contamination from both non-τ events and from τ events in which neither τ decays via $\tau \to \rho\nu_\tau$, illustrated in figure 4-19. The background contamination has initially been estimated from the number of simulated background events normalised to the data based on the approximate luminosity of the simulation sample passing the event selection. The simulation predictions have been checked using background enhanced samples of data events following a similar

procedure described in [50]. For each type of background, the ratio of the number of background enhanced data events passing the event selection to the number of events predicted by the simulation N_{data}/N_{sim} has been taken. This ratio provided a scale factor with which to correct the original simulation prediction. The cuts applied to select the background enhanced samples of data events are summarised in table 4-3. The cut values have been chosen arbitrarily and are described below. The momentum distributions of

Selection Cut	**Enhanced Background**		
	Bhabhas	**μ pairs**	**$q\overline{q}$**
ρ candidate momentum GeV/c	> 4.5	> 4.8	< 4.8
E/p	$0.8 <...< 1.2$	< 0.1	$0.1 <...< 0.8$
mass of non-tagging hemisphere GeV/c^2	-	-	> 2.3

Table 4-3. *Applied cuts for selecting background enhanced samples of data events.*

reconstructed ρ candidates in the centre of mass shown in figures 4-5 and 4-8 are strongly peaked at ≈5.3 GeV/c for Bhabha and μ pair events. These events have been enhanced relative to $q\overline{q}$ and τ pair events by requiring the ρ candidate momentum to be $>$ 4.5 GeV/c for Bhabha events and $>$ 4.8 GeV/c for μ pair events. The E/p distributions for Bhabha events (figure 4-2(b)) and μ pair events (figure 4-3(c)) are well separated and the requirement of $0.8 <$ E/p < 1.2 has been applied to select an enhanced sample of Bhabha events. A requirement of E/p < 0.1 has been applied to select an enhanced sample of μ pair events. In these Bhabha and μ pair enhanced data samples, the estimated contamination from non-Bhabha or non-μ pair events respectively has been subtracted. The remaining events provide an estimate of the number of Bhabha or μ pair events in the corresponding sample. Figure 4-20 shows the momentum distribution of reconstructed ρ candidates in the centre of mass from the enhanced sample of Bhabha events in the data after background subtraction (histogram) and from simulated Bhabha events passing the same set of cuts and with the corrected normalisation (points). The correction factor has

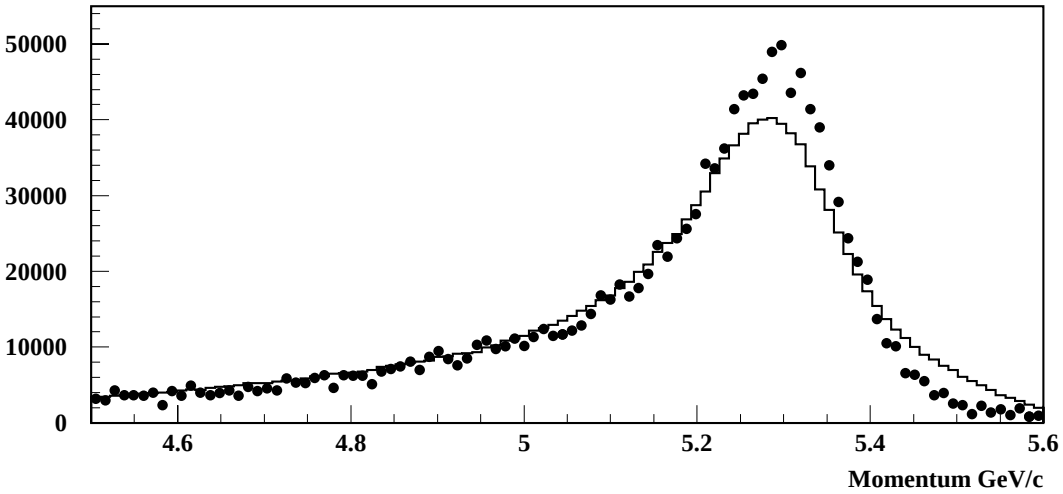

Figure 4-20. *Momentum distribution of reconstructed ρ candidates in the centre of mass from the enhanced sample of Bhabha events in the data after background subtraction (histogram) and from simulated Bhabha events with corrected normalisation (points).*

been determined from the momentum distributions between 5.6 GeV/c and 4.5 GeV/c. The figure shows a difference in shape between the simulation and data distributions which leads to a systematic variation in the correction factor depending on which region of the momentum distribution is used. To assess this variation, correction factors have also been determined from the momentum distributions between 5.6 GeV/c and several different momentum values from 4.6 GeV/c to 5.1 GeV/c. The variation in the correction factors has been found to be 0.02 which is used as the systematic error on the measured value of the correction factor of 0.72 based on the momentum region shown in the figure. A similar method has been used to determine the systematic errors on the scale factors for μ pair events, $q\overline{q}$ events, and τ pair events quoted below. The scale factor used to correct the simulation prediction for μ pair events has been measured to be 0.73 ± 0.04. Applying these correction factors to the predicted background fractions for Bhabha and μ pair events, the corrected background estimates are $(0.60 \pm 0.23) \times (0.72 \pm 0.02)$ = (0.43

$\pm$ 0.16)% for Bhabha events, and (0.09 $\pm$ 0.06)$\times$(0.73 $\pm$ 0.04) = (0.07 $\pm$ 0.05)% for μ pair events.

An enhanced sample of $q\overline{q}$ events in the data has been selected using events in which the invariant mass of the hemisphere opposite to the hemisphere used to tag the event is greater than the mass of the τ (see figure 4-11). Further requirements on the ρ candidate momentum in the centre of mass to be $<$ 4.8 GeV/c and on E/p to be in the range 0.1 $<$ E/p $<$ 0.8 have been applied to reject Bhabha and μ pair events. After subtracting the estimated contamination from non-$q\overline{q}$ events from this data sample the ratio $N^{qq}_{data}/N^{qq}_{sim}$ has been found to be 0.78 $\pm$ 0.06. The predicted $q\overline{q}$ background has been scaled by this factor giving a corrected background estimate of (4.52 $\pm$ 0.42)%. To check the simulation prediction for τ pair events, the corrected non-τ backgrounds have been subtracted from the number of data events passing the event selection. The scale factor determined from the remaining data events and the number of τ pair events predicted by the simulation to pass the event selection has been measured to be 0.71 $\pm$ 0.01 . Applying this factor to the predicted non-ρ τ background gives a corrected background estimate of (5.44 $\pm$ 0.30)$\times$(0.71 $\pm$ 0.01) = (3.86 $\pm$ 0.22)%.

The estimated background fractions of different physics processes in the sample of data events remaining after the event selection predicted from simulated event samples and their corrected values are summarised in table 4-4. The large errors on the estimated background fractions of Bhabha and μ pair events are due to the limited number of simulation events for these processes. Both of these backgrounds are measured to be small however so these errors do not significantly increase the error on the total background. The total contribution from physics backgrounds in the sample of data events passing the event selection, after corrections to the simulated event sample predictions, is estimated to be (8.88 $\pm$ 0.50)%. The largest contribution to the total background is from $q\overline{q}$ events and there is also a significant contribution from τ events in which neither τ decays via $\tau \rightarrow \rho\nu_{\tau}$. For the branching ratio measurement, the correction applied is that for the

Data Set	**Background Fraction %**	
	Simulation Prediction	**Corrected Value**
Bhabhas	0.60 ± 0.23	0.43 ± 0.16
μ pairs	0.09 ± 0.06	0.07 ± 0.05
$q\overline{q}$	5.79 ± 0.31	4.52 ± 0.42
Total (non-τ)	6.48 ± 0.39	5.02 ± 0.45
τ pairs (non-ρ)	5.44 ± 0.30	3.86 ± 0.22
Total	11.9 ± 0.5	8.88 ± 0.50

Table 4-4. *Background fractions of different physics processes in the sample of data events passing the event selection predicted from simulated event samples.*

non-τ background only which is estimated to be $(5.02 \pm 0.45)\%$, since the decay mode of the tagged τ is not expected to bias the τ sample on which the measurement is made.

5

Measurement of the τ Leptonic Branching Ratios

5.1 Introduction

This chapter describes the identification of leptonic decays in the sample of 38027 data events which passed the $e^+e^- \rightarrow \tau^+\tau^-$ event selection process described in chapter 4. For each event the lepton identification has been performed on the τ decay which was not used to tag the event. The performance of the lepton identification is discussed and the results are used to extract a measurement of the τ leptonic branching ratios.

5.2 Lepton Identification

Lepton identification has been carried out only on hemispheres containing exactly one well reconstructed charged track originating near the interaction point and defined by the criteria described in section 4.3. The criteria for the identification of electrons and muons are defined by standard sets of cuts for the BaBar experiment and are described in detail elsewhere [43, 45]. A summary of these criteria is given below.

For the particle producing the charged track to be classified as an electron E/p is required to be in the range $0.75 < \text{E/p} < 1.3$ with a dE/dx measurement from the drift chamber of $500 < \text{dE/dx} < 1000$. In addition, the calorimeter cluster associated with the charged track is required to cover at least 3 crystals, and have a lateral energy distribution consistent

with that of an electromagnetic shower from an electron. Strongly interacting particles such as pions can produce both hadronic and electromagnetic showers in the calorimeter producing clusters with different energy distributions than the purely electromagnetic showers from electrons. The discriminating variable used to distinguish between the two types of shower is the lateral moment, LAT, which is defined as [15, 42]

$$LAT = \frac{\sum_{i=3}^{N} E_i r_i^2}{\sum_{i=3}^{N} E_i r_i^2 + E_1 r_0^2 + E_2 r_0^2} \tag{5.1}$$

where E_i is the energy deposit in the ith crystal (the crystals are numbered from 1 to N in order of decreasing energy); r_i is the lateral distance from the centre of the ith crystal to the shower centre; r_0 is the average distance between two crystals. Electron showers produce low values of LAT because most of the energy is contained in only a couple of crystals and the sum over energy in the numerator does not include the two highest energy crystals. LAT is required to be in the range $0 <$ LAT < 0.6.

The muon identification is based primarily on information from the instrumented flux return with additional criteria based on information from the electromagnetic calorimeter. If the charged track falls within the calorimeter acceptance then the energy measured by the calorimeter is required to be in the range $0.05 < E_{cal} < 0.4\text{GeV}/c^2$. The number of interaction lengths traversed by the track inside the BaBar detector is required to be > 2.2 and the difference between this number and the number of interaction lengths expected assuming the track to be a muon is required to be <0.8. A muon which traverses the instrumented flux return will characteristically produce a single hit in each layer. The charged track is required to traverse more than one layer and a measure of the track continuity is defined [45]:

$$T_c = \frac{N_L}{L_h - F_h(+1)} \tag{5.2}$$

where N_L is the number of hit layers, L_h is the last hit layer, and F_h is the first hit layer. The term in brackets is only included if there is no hit in the inner layer[1]. For tracks in the forward endcap T_c is required to be > 0.3. In addition, the average number of hit strips per layer is required to be <8, and its standard deviation < 4. The χ^2 of the hits measured in the instrumented flux return with the expected hits from extrapolation of the charged track from the drift chamber into the instrumented flux return is required to be <5, and the χ^2 of the measured hits with respect to a 3rd-order polynomial fit of those hits is required to be <3.

5.3 Performance of Lepton Identification

A sample of 6185 data events were identified to contain $\tau \rightarrow e\nu_e\nu_\tau$ decays and 5166 data events were identified to contain $\tau \rightarrow \mu\nu_\mu\nu_\tau$ decays. In this section the performance of the lepton identification is discussed in terms of the efficiency for electron and muon identification, and the purity of the selected samples of leptonic τ decays.

5.3.1 Lepton Selection Efficiency

The efficiency for the identification of leptonic decays in the selected τ sample has been measured using simulated generic τ pair events and is defined as:

$$\epsilon_l^{id} = \frac{N_l^{id}}{N_l^{true}} \tag{5.3}$$

where N_l^{id} is the number of correctly identified leptons, and N_l^{true} is the number of true $\tau \rightarrow l\nu_l\nu_\tau$ decays in the selected τ events from the simulation sample. In making

[1]This is due to the way the layers are numbered. The inner layer has the number -1 with the rest of the layers numbered sequentially 1,2,3,...N, where N is the outermost layer. There is no layer 0.

the efficiency estimation it is important to consider that the simulated events may not accurately model the data, particularly at this relatively early stage in the life of the BaBar detector. An estimate of the efficiency from simulated events may therefore be incorrect. The efficiency determined from the simulation has been checked using the efficiencies determined from identified samples of leptons in data events. Tables of efficiencies from data events binned into momentum, polar angle and azimuthal angle have been used so that the efficiency measurement takes into account the shape of these spectra for the channel under consideration.

5.3.1.1 Electron Identification Efficiency

The electron identification efficiency has been determined from $\tau \rightarrow e\nu_e\nu_\tau$ decays in simulated τ pair events to be $(91.4 \pm 0.7)\%$. The efficiencies determined from identified samples of electrons in the data do not cover the full momentum spectrum of electrons produced in $\tau \rightarrow e\nu_e\nu_\tau$ decays. Comparisons between simulation and data have therefore been restricted to the momentum range covered by the data events. The efficiency determined from a sample of identified electrons with momentum $<$ 4.0 GeV/c from Bhabha and $\gamma\gamma$ $\rightarrow$eeee events in the data[2] has been measured to be $(92.8 \pm 0.7)\%$. The systematic error on this efficiency has been estimated, applying the current standard procedure, from a comparison with the efficiency determined from a sample of data events containing only Bhabha electrons. Table 5-1 compares the electron identification efficiency, ϵ_e^{id}, for electrons with momentum $<$ 4.0 GeV/c estimated from the different samples of electrons in the data and from $\tau \rightarrow e\nu_e\nu_\tau$ decays in simulated τ pair events. The efficiency determined from the sample of Bhabha electrons in the data shows a variation of 1.6% from the value determined using the Bhabha + $\gamma\gamma$ $\rightarrow$eeee electron sample. This value has been added in quadrature with the statistical error on the measured

[2] A description of the samples of identified electrons in the data may be found elsewhere [43].

Events	Electron Sample	ϵ_e^{id} %
Simulation	$\tau \to e\nu_e\nu_\tau$	91.7 ± 0.8
Data	Bhabha + $\gamma\gamma \to$eeee	92.8 ± 0.7
	Bhabhas	91.2 ± 0.8

Table 5-1. *Comparison of the electron identification efficiency measured from different samples of electrons with p < 4.0 GeV/c in the data and from $\tau \to e\nu_e\nu_\tau$ decays in simulated τ pair events.*

efficiency from the Bhabha + $\gamma\gamma \to$eeee sample[3] so that ϵ_{data} = $(92.8 \pm 1.8)\%$ which reflects the systematic variation. The efficiency determined from the simulation over the same momentum range covered by the data samples has been measured to be $(91.7 \pm 0.8)\%$. The ratio $\epsilon_{data}/\epsilon_{sim}$ yields a correction factor of 1.01 ± 0.02. Applying this correction factor to the simulation efficiency estimate over the full electron momentum range, the corrected electron identification efficiency is $(91.4 \pm 0.7)\times(1.01 \pm 0.02)$ = $(92.3 \pm 2.0)\%$.

5.3.1.2 Muon Identification Efficiency

The muon identification efficiency has been determined from $\tau \to \mu\nu_\mu\nu_\tau$ decays in simulated τ pair events to be $(67.4 \pm 1.2)\%$. The efficiency determined from a sample of identified muons from ee$\mu\mu$ events in the data[4] over the full momentum spectrum of muons produced in $\tau \to \mu\nu_\mu\nu_\tau$ decays has been measured to be $(63.8 \pm 1.4)\%$ showing an overestimate in the simulation prediction. The sample of ee$\mu\mu$ events used is currently the only sample of muons in the data for which efficiency information is available for analyses, hence no comparison with other muon samples in the data can be made. An additional sample of identified muons from $\mu\mu\gamma$ events in the data has recently been developed and efficiency information should be available for future analyses. An initial study comparing the performance of the muon identification on the two muon samples has

[3]The method for evaluating the systematic error follows that described in [44].

[4]A description of the samples of identified muons in the data may be found elsewhere [46, 47].

shown there is some evidence of possible contamination to the ee$\mu\mu$ sample [48]. Any contamination would bias the measured efficiency towards lower values. To account for this, the error shown on the efficiency measurement from the ee$\mu\mu$ sample is composed of a statistical error and an error of 1% of the measured value[5] due to sample contamination added in quadrature. A further systematic is applied from the statistical error on the comparison $\epsilon_{data}/\epsilon_{sim}$, so that the muon identification efficiency is $(63.8 \pm 2.3)\%$. It can be seen that the muon identification efficiency in both the simulation and the data is significantly worse than the efficiency for electron identification. This is a reflection of the poor performance of the Instrumented Flux Return.

5.3.2 Background Contamination in the Lepton Sample

The selected samples of leptonic τ decays in the data have some contamination from non-τ events, from leptonic τ decays in which the tagged τ did not decay via $\tau \to \rho\nu_\tau$, and from non-leptonic τ decays which have been mis-identified. The background contamination has been estimated from the number of simulated background events passing the lepton identification and normalised to the data. The estimated background fractions of different physics processes remaining in the sample of data events passing the lepton identification predicted from simulated event samples is shown in table 5-2. It can be seen that while the backgrounds from Bhabha and μ-pair events were measured to be small in the sample of events passing the initial event selection (see table 4-4) they become more significant in the respective samples of selected leptonic τ decays. As a consequence, the large error on the background fraction of Bhabha events due to the limited statistics in the simulation now also becomes significant in contributing to the error on the total background fraction in the $\tau \to e\nu_e\nu_\tau$ sample. The contamination to the $\tau \to \mu\nu_\mu\nu_\tau$

[5]The systematic error due to contamination of the ee$\mu\mu$ sample is described in more detail in [45] and assumes a 1% contamination.

Data Set	Background Fraction %	
	$\tau \to e\nu_e\nu_\tau$	$\tau \to \mu\nu_\mu\nu_\tau$
Bhabhas	3.71 ± 1.40	< 0.7 at 68% CL
μ pairs	< 0.4 at 90% CL	0.88 ± 0.44
$q\overline{q}$	0.05 ± 0.03	0.28 ± 0.18
τ (mis-identified)	2.88 ± 0.54	15.5 ± 1.4
Total	6.64 ± 1.55	16.6 ± 1.6

Table 5-2. *Background fractions remaining in the sample of data events passing the lepton identification predicted from simulated event samples.*

sample is dominated by mis-identified non-μ τ decays and this is the dominant source of the error on the total background fraction in this sample. The total contribution from physics backgrounds in the selected samples of $\tau \to l\nu_l\nu_\tau$ events has been estimated from the simulated event samples to be $(6.64 \pm 1.55)\%$ in the $\tau \to e\nu_e\nu_\tau$ sample and $(16.6 \pm 1.6)\%$ in the $\tau \to \mu\nu_\mu\nu_\tau$ sample. In both lepton samples, there is also a significant contribution from leptonic τ decays in which the tagged τ did not decay via $\tau \to \rho\nu_\tau$, of $(6.75 \pm 0.82)\%$ in the $\tau \to e\nu_e\nu_\tau$ sample and $(6.30 \pm 0.87)\%$ in the $\tau \to \mu\nu_\mu\nu_\tau$ sample. However, for the branching ratio measurement, these decays may be included with the correctly tagged leptonic decays as signal events since (as mentioned in section 4.4.3) the decay mode of the tagged τ is not expected to bias the sample of leptonic τ decays.

5.4 Extraction of Leptonic Branching Ratios

The τ leptonic branching fraction can be defined for a sample of τs as the ratio of the number of leptonic τ decays to the total number of τs in the sample. For this analysis, the leptonic branching fraction can be written as:

$$\mathcal{B}(\tau \to l\nu_l\nu_\tau) = \frac{N_{\tau\to l,\tau\to\rho}}{N_{\tau\to all,\tau\to\rho}} \tag{5.4}$$

where $N_{\tau\to l,\tau\to\rho}$ is the number of τ pair events in the data in which one τ decays leptonically, with the other τ decaying via the $\tau \to \rho\nu_\tau$ channel; $N_{\tau\to all,\tau\to\rho}$ is the number of τ pair events in the data in which one τ decays via $\tau \to \rho\nu_\tau$ with the other τ decaying via any allowed channel. The sample of τ pair events in the data, $N_{\tau\to all,\tau\to\rho}$, can be determined from the event selection efficiency:

$$N_{\tau\to all,\tau\to\rho} = \frac{N^{selected}_{\tau\to all,\tau\to\rho}}{\epsilon_{\tau\to all,\tau\to\rho}} \tag{5.5}$$

where $N^{selected}_{\tau\to all,\tau\to\rho}$ is the number of τ pair events in the data which pass the event selection in which one τ decays via $\tau \to \rho\nu_\tau$ with the other τ decaying via any allowed channel, $\epsilon_{\tau\to all,\tau\to\rho}$ is the efficiency for selecting these events.

A small number of background events also pass the event selection as discussed in section 4.4.3. To determine $N^{selected}_{\tau\to all,\tau\to\rho}$ from the sample of all events which pass the event selection, $N^{selected}_{all}$, a correction must be made by subtracting the background events giving

$$N^{selected}_{\tau\to all,\tau\to\rho} = N^{selected}_{all}(1 - bf_{\tau\to all,\tau\to\rho}) \tag{5.6}$$

where $bf_{\tau\to all,\tau\to\rho}$ is the background fraction in $N^{selected}_{all}$. From equations (5.5) and (5.6) we obtain an expression for $N_{\tau\to all,\tau\to\rho}$ from observed quantities:

$$N_{\tau\to all,\tau\to\rho} = \frac{N^{selected}_{all}(1 - bf_{\tau\to all,\tau\to\rho})}{\epsilon_{\tau\to all,\tau\to\rho}}. \tag{5.7}$$

The number of leptonic τ decays, $N_{\tau\to l,\tau\to\rho}$ from this sample of τ events in the data is given by a similar expression to equation 5.5:

$$N_{\tau\to l,\tau\to\rho} = \frac{N^{selected}_{\tau\to l,\tau\to\rho}}{\epsilon_{\tau\to l,\tau\to\rho}} \tag{5.8}$$

where $N^{selected}_{\tau\to l,\tau\to\rho}$ is the number of τ pair events in the data which pass the event selection in which one τ decays leptonically with the other τ decaying via $\tau \to \rho\nu_\tau$, $\epsilon_{\tau\to l,\tau\to\rho}$ is the efficiency for selecting these events. $N^{selected}_{\tau\to l,\tau\to\rho}$ is not directly observed but can be determined from the efficiency for lepton identification:

$$N^{selected}_{\tau\to l,\tau\to\rho} = \frac{N^{id}_l}{\epsilon^{id}_l}. \tag{5.9}$$

where N^{id}_l is the number of correctly identified τ leptonic decays, ϵ^{id}_l is the lepton identification efficiency. Some background events also pass the lepton identification as discussed in section 5.4. To determine N^{id}_l from the sample of all events which pass the lepton identification, N^{id}_{all}, a correction must be made by subtracting the background events giving:

$$N^{id}_l = N^{id}_{all}(1 - bf_l) \tag{5.10}$$

where bf_l is the fraction of background events in N^{id}_{all}. From equations (5.8), (5.9), and (5.10) we can now obtain an expression for the number of leptonic τ decays

$$N_{\tau\to l,\tau\to\rho} = \frac{N^{id}_{all}(1 - bf_l)}{\epsilon_{\tau\to l,\tau\to\rho}\epsilon^{id}_l}. \tag{5.11}$$

Substituting the expressions for $N_{\tau\to l,\tau\to\rho}$ and $N_{\tau\to all,\tau\to\rho}$ into equation (5.4) gives an expression for the τ leptonic branching ratio:

$$\mathcal{B}(\tau \to l\nu_l\nu_\tau) = \frac{N^{id}_{all}(1 - bf_l)}{N^{selected}_{all}(1 - bf_{\tau\to all,\tau\to\rho})} \frac{\epsilon_{\tau\to all,\tau\to\rho}}{\epsilon_{\tau\to l,\tau\to\rho}} \frac{1}{\epsilon^{id}_l}. \tag{5.12}$$

If the event selection produced a completely unbiased sample of τs then the two efficiency terms $\epsilon_{\tau\to all,\tau\to\rho}$ and $\epsilon_{\tau\to l,\tau\to\rho}$ would be identical and would cancel. The ratio of these terms is the definition of the bias factor described in section 4.4.2. This indicated that the event selection may introduce a bias which must be included. The branching ratio expression is written below in terms of the bias factor:

$$\mathcal{B}(\tau \to l\nu_l\nu_\tau) = \frac{N_{all}^{id}(1 - bf_l)}{N_{all}^{selected}(1 - bf_{\tau\to all,\tau\to\rho})} f_{bias} \frac{1}{\epsilon_l^{id}}. \tag{5.13}$$

Using the results of the event selection described in chapter 4 and the lepton identification described in this chapter, from equation (5.13) the measured τ leptonic branching ratios are

$$\mathcal{B}(\tau \to e\nu_e\nu_\tau) = 17.1 \pm 0.2(stat) \pm 0.6(syst)\% \tag{5.14}$$

$$\mathcal{B}(\tau \to \mu\nu_\mu\nu_\tau) = 18.3 \pm 0.3(stat) \pm 0.9(syst)\%. \tag{5.15}$$

5.4.1 Estimation of Statistical and Systematic Errors

The estimated error on each branching ratio measurement is made up of a statistical error, which has been calculated from the statistical error on the number of events in the selected lepton sample, and a systematic error described in more detail below.

The systematic error on each branching ratio measurement includes contributions from the bias factor, f_{bias}, described in section 4.4.2; from $bf_{\tau\to all,\tau\to\rho}$, the estimated background fraction in the data events passing the initial event selection; from bf_l, the estimated background fraction in the selected sample of leptonic τ decays; and from ϵ_l^{id}, the estimated efficiency for the identification of leptonic τ decays. The estimated errors associated with each of these terms have been discussed in the relevant sections of this chapter and chapter 4. The contributions from each term to the estimate of the absolute systematic error on each branching ratio measurement are summarised in table 5-3. The largest contributions to the systematic error on both measurements are from f_{bias}, bf_l, and ϵ_l^{id}. For the $\mathcal{B}(\tau \to e\nu_e\nu_\tau)$ measurement these are each of comparable size. The contribution from the bias factor has been determined from the statistical error quoted in section 4.4.2, and is due to the limited statistics used in the simulation sample. The uncertainty in the

Source	$\mathcal{B}(\tau \to e\nu_e\nu_\tau)$	$\mathcal{B}(\tau \to \mu\nu_\mu\nu_\tau)$
f_{bias}	0.35	0.37
$bf_{\tau\to all,\tau\to\rho}$	0.08	0.09
ϵ_l^{id}	0.37	0.67
bf_l	0.28	0.35
Total	0.59	0.85

Table 5-3. *Contributions to the absolute systematic error of the measured τ leptonic branching ratios.*

background contamination to the $\tau \to e\nu_e\nu_\tau$ sample is dominated by the large error on the estimated Bhabha background and is again due to the limited statistics in the simulation for this process. There is also a large contribution from the uncertainty in the efficiency for electron identification from the spread in the efficiency measurements from the different samples of electrons in the data. The largest contribution to the systematic error on the $\mathcal{B}(\tau \to \mu\nu_\mu\nu_\tau)$ measurement is from the uncertainty in the efficiency for muon identification. This is due to the limited statistics in the simulation events used to calculate this value and may itself be underestimated as it has not been possible to perform systematic comparisons of efficiencies from different samples of identified muons in the data. The uncertainty in the background contamination to the $\tau \to \mu\nu_\mu\nu_\tau$ sample is dominated by the error on the high background from mis-identified τ decays.

5.4.2 Comparison of Experimental Results

The τ leptonic branching ratios have already been measured elsewhere with great precision. Recent measurements have come from the LEP experiments and the CLEO collaboration at the CESR. A summary of recent measurements of the τ leptonic branching ratios from these experiments is given in table 5-4. Where two errors are shown, the first error is statistical and the second systematic. The ALEPH measurement shows the greatest precision for both leptonic modes as a result of the small systematics achieved by

this experiment. The CLEO measurement is based on a dataset which contains the largest

Experiment	$\mathcal{B}(\tau \to e\nu_\tau\overline{\nu}_e)\%$	$\mathcal{B}(\tau \to \mu\nu_\tau\nu_\mu)\%$
DELPHI (1998) [49]	$17.92 \pm 0.11 \pm 0.10$	$17.32 \pm 0.10 \pm 0.07$
OPAL (1995) [50]	18.04 ± 0.33	17.36 ± 0.27
CLEO (1997) [51]	$17.76 \pm 0.06 \pm 0.17$	$17.37 \pm 0.08 \pm 0.18$
ALEPH (1996) [52]	$17.79 \pm 0.12 \pm 0.06$	$17.31 \pm 0.11 \pm 0.05$
PDG World Average [5]	17.81 ± 0.07	17.33 ± 0.07

Table 5-4. *Recent measurements of the τ leptonic branching ratios*

sample of τ pair events ($N_\tau = 3.25 \times 10^6$) and has a correspondingly small statistical error. The measurements of $\mathcal{B}(\tau \to e\nu_e\nu_\tau)$ and $\mathcal{B}(\tau \to \mu\nu_\mu\nu_\tau)$ presented here are consistent to within $\sim 1\sigma$ with the world average value.

5.5 Lepton Universality

The universality of the electron and muon couplings to the W can be measured from the ratio of the τ leptonic branching fractions. From equation (1.2), the ratio of the τ leptonic branching fractions is equivalent to the ratio of the τ leptonic decay rates

$$\frac{\mathcal{B}(\tau \to \mu\nu_\tau\nu_\mu)}{\mathcal{B}(\tau \to e\nu_\tau\nu_e)} = \frac{\Gamma(\tau \to \mu\nu_\tau\nu_\mu)}{\Gamma(\tau \to e\nu_\tau\nu_e)}. \tag{5.16}$$

Using equation (1.5) this ratio may be written in terms of g_μ and g_e, the muon and electron weak coupling strengths:

$$\frac{\mathcal{B}(\tau \to \mu\nu_\tau\overline{\nu}_\mu)}{\mathcal{B}(\tau \to e\nu_\tau\overline{\nu}_e)} = \frac{g_\mu^2}{g_e^2}\left[\frac{f\left(\frac{m_\mu^2}{m_\tau^2}\right)}{f\left(\frac{m_e^2}{m_\tau^2}\right)}\right] \tag{5.17}$$

where $f(m_\mu^2/m_\tau^2)$ = 0.973, and $f(m_e^2/m_\tau^2)$ = 1 as described in section 1.2 of chapter 1.

A summary of recent measurements of the ratio g_μ/g_e based on the τ leptonic branching ratio measurements shown in table 5-4 from the LEP experiments and the CLEO collaboration is given in table 5-5. Inserting the measured τ leptonic branching fractions

Experiment	g_μ/g_e
DELPHI (1998) [49]	0.9971 ± 0.0052
OPAL (1995) [50]	0.994 ± 0.012
CLEO (1997) [51]	1.0026 ± 0.0055
ALEPH (1996) [52]	1.0002 ± 0.0051

Table 5-5. *Recent measurements of g_μ/g_e from measurements of the τ leptonic branching ratios.*

presented here into equation (5.17) the ratio of the muon and electron weak coupling strengths is found to be:

$$\frac{g_\mu}{g_e} = 1.05 \pm 0.03. \tag{5.18}$$

The error on this measurement is currently an order of magnitude higher than recent results.

6

Conclusions

6.1 Introduction

A description of an analysis of data from the BaBar experiment resulting in a preliminary measurement of the leptonic branching ratios of the τ lepton has been presented in this thesis. In addition, an outline of part of the online software written for the calorimeter trigger has been described. In this chapter the main results presented in the thesis are summarised and concluding remarks are made.

6.2 Online Software for the Calorimeter Trigger

Software has been developed for the operation of the calorimeter trigger. The structure allows the calorimeter trigger to go through the sequence of stages necessary for taking data or performing calibrations. The implementation is in C++ and object oriented techniques have been applied to the software design. In addition software has been written to determine a suitable value used to control the timing of data sent between the calorimeter and calorimeter trigger. The software written for the calorimeter trigger plays an essential role in the operation of the BaBar detector.

6.3 Analysis of τ Decays

The analysis of τ decays presented in this thesis has provided a clean environment in which to test the performance of the BaBar detector for e, μ, and π identification. The analysis has demonstrated the successful reconstruction of π^0s and ρs in the data. The π^0 reconstruction efficiency has been estimated to be $19.1 \pm 0.2\%$. Fake neutral showers in the electromagnetic calorimeter, and detector effects causing a low mass tail in the π^0 mass distribution have both been observed to be significant sources of efficiency loss. There is scope for future improvement in the π^0 reconstruction efficiency from inclusion of single maxima merged π^0s, and recovery of π^0s whose daughter photons convert inside the detector before reaching the calorimeter. Future analyses will also benefit from improvements to the algorithms used for the reconstruction of neutral clusters in the calorimeter. Events containing the tagging mode, $\tau \to \rho\nu_\tau$, were selected with an efficiency of $17.0 \pm 0.2\%$, the major efficiency losses being largely due to the issues relating to π^0 reconstruction outlined above. The analysis incorporated a study of discriminating variables for the rejection of non-τ background events. It was found that while Bhabha and μ-pair events can be well controlled, the $q\overline{q}$ background is less easy to contain without sacrificing signal efficiency.

The lepton identification performed on the selected τ sample showed good agreement between simulation and data for electron identification. For the muon identification, the difference in performance between simulation and data was observed to be more significant. In addition, the efficiency for muon identification was observed to be significantly worse than the efficiency for electron identification and is a reflection of the performance of the Instrumented Flux Return for muon identification. The estimated background fractions in the selected $\tau \to e\nu_e\nu_\tau$ and $\tau \to \mu\nu_\mu\nu_\tau$ samples indicated that the Bhabha and μ pair backgrounds are enhanced in the respective samples of leptonic τ decays. Since the error on the Bhabha background in the $\tau \to e\nu_e\nu_\tau$ sample is significant, further

optimisation of rejection cuts should be investigated to increase the level of Bhabha rejection. The background from mis-identified τ decays was estimated to be much higher in the $\tau \to \mu\nu_\mu\nu_\tau$ sample than in the $\tau \to e\nu_e\nu_\tau$ sample.

The analysis of data has been used to make a preliminary measurement of the τ leptonic branching ratios. These have been measured to be:

$$\mathcal{B}(\tau \to e\nu_\tau\nu_e) = 17.1 \pm 0.2(stat) \pm 0.6(syst)(\%) \tag{6.1}$$

$$\mathcal{B}(\tau \to \mu\nu_\tau\nu_\mu) = 18.3 \pm 0.3(stat) \pm 0.9(syst)(\%). \tag{6.2}$$

A comparison with recent measurements of the τ leptonic branching ratios from other high energy physics experiments indicated that branching ratio measurements from BaBar can become statistically competitive based on only a fraction of the data set. Measurements based on the current full BaBar data set of $20fb^{-1}$ integrated luminosity (which contains $\sim 19 \times 10^6$ τ pairs) would improve on the statistical precision of current measurements. The future will bring even greater statistical precision as BaBar will produce $\sim$30 million τ events per year. However, the precision of the τ leptonic branching ratio measurements presented here is dominated by systematics.

The measurements of $\mathcal{B}(\tau \to e\nu_e\nu_\tau)$ and $\mathcal{B}(\tau \to \mu\nu_\mu\nu_\tau)$ were found to be consistent to within $\sim 1\sigma$ with recent results from other high energy physics experiments shown in table 5-4 and with the current world average values.

6.3.1 Improving on the Precision

The contributions to the systematic error have been described in section 5.4.1 and the values given in table 5-3 are reproduced in table 6-1 for ease of reference. It can be seen that at least a factor five improvement on the systematic error is required to achieve the

Source	$\mathcal{B}(\tau \to e\nu_e\nu_\tau)$	$\mathcal{B}(\tau \to \mu\nu_\mu\nu_\tau)$
f_{bias}	0.35	0.37
$bf_{\tau\to all,\tau\to\rho}$	0.08	0.09
ϵ_l^{id}	0.37	0.67
bf_l	0.28	0.35
Total	0.59	0.85

Table 6-1. *Contributions to the absolute systematic error of the measured τ leptonic branching ratios (reproduced from table 5-3).*

precision necessary to make a competitive measurement of the τ leptonic branching ratios. It is expected that greater control of systematics will be achieved and future analyses will be able to improve on the precision presented here. Ways in which improved precision can be achieved are discussed below.

The contributions from the bias factor, f_{bias}, to the systematic errors on both measurements are of comparable size. The source of this error is the statistical precision of the selection efficiencies described in section 4.4.2. The precision depends upon the efficiencies achieved and on the size of the simulation sample used to make the efficiency measurements. The simplest method of reducing this systematic therefore is to increase the size of the simulation sample. The alternative is to increase the event selection efficiency. The principal way that this could be achieved is through investigating methods of improving the π^0 reconstruction efficiency discussed above.

The efficiency for the identification of leptonic τ decays, ϵ_l^{id}, is the largest contribution to the systematic error on the $\mathcal{B}(\tau \to \mu\nu_\mu\nu_\tau)$ measurement and is a significant contribution to the systematic error on the $\mathcal{B}(\tau \to e\nu_e\nu_\tau)$ measurement. For the electron identification this error is dominated by the spread of the measured efficiencies from electrons in data events. The statistical errors on these efficiencies however are quite large and depend on the number of simulation events[1]. With an increased sample of simulated events, the

[1]The efficiency measurements were made using simulated τ pair events and look-up tables of efficiencies from data events.

statistical errors would be reduced and the measured efficiencies would be expected to converge. The larger contribution to the error on the $\mathcal{B}(\tau \rightarrow \mu\nu_\mu\nu_\tau)$ measurement is principally due to the lower efficiency for muon identification. The muon identification depends on the Instrumented Flux Return, which has suffered from problems with many of its active detector modules, the Resistive Plate Chambers, described in chapter 2. The cause of the poor performance of the Instrumented Flux Return is currently being investigated.

The final significant contribution to the systematic error on both measurements is the estimated background fraction in the selected samples of leptonic τ decays, bf_l. The uncertainty in the background to the $\tau \rightarrow e\nu_e\nu_\tau$ sample arises from the large statistical error on the estimated Bhabha background. This error could be reduced by using a larger sample of simulated Bhabha events, or by modifying the event selection cuts to increase the level of Bhabha rejection, as suggested above. The uncertainty in the background to the $\tau \rightarrow \mu\nu_\mu\nu_\tau$ sample is dominated by the statistical error on the background from mis-identified τ decays. Methods for reducing this background should be investigated in future analyses.

References

[1] P.W.Higgs, Phys.Lett **12**, 132 (1964)

[2] The ALEPH Collaboration, Phys.Lett **B495**, 1-17 (2000)

[3] The LEP Higgs Working Group, hep-ex/0107029 (2001)

[4] M.L.Perl, Phys.Rev.Lett **35**, 1489 (1975)

[5] D.E.Groom *et al*, Particle Data Group, Eur.Phys.Jour. **C15**, 1 (2000)

[6] M.L.Perl, Rep.Prog.Phys **55**, 653 (1992)

[7] Proceedings of the 20th Annual SLAC Summer Institute on Particle Physics, SLAC-R-412 (1992)

[8] W.Marciano and A.Sirlin, Phys.Rev.Lett **61** (1988) 1815

[9] F.Halzen and A.Martin, 'Quarks and Leptons', Wiley (1984)

[10] Y.S.Tsai, Phys.Rev **D4**, 2821 (1971)

[11] The ALEPH Collaboration, CERN-OPEN-99-258, (1999)

[12] D.H.Perkins, 'Introduction to High Energy Physics', Addison-Wesley (1982)

[13] Proceedings of the 27th Annual SLAC Summer Institute on Particle Physics, http://www.slac.stanford.edu/gen/meeting/ssi/1999/

[14] The BaBar Collaboration, 'Observation of CP violation in the B^0 meson system', SLAC-PUB-8904, submitted to Phys.Rev.Lett (2001)

[15] The BaBar Collaboration, P.F.Harrison and H.E.Quinn, Report of the BaBar Physics Workshop (1998)

[16] E.Campagna *et al*, 'Measurement of the Tau Lepton Lifetime with the Decay Length Method', BaBar Analysis Document #55 (2000)

[17] The BaBar Collaboration, 'Measurement of the Tau Lepton Lifetime with the Decay Length Method', BaBar Analysis Document #83 (2000)

[18] The BaBar Collaboration, 'BaBar Technical Design Report', SLAC-R-0457 (1995)

[19] The BaBar Collaboration, 'The BaBar Detector at the PEP-II B Factory', SLAC-PUB-8569, to appear in Nucl.Inst.Methods

[20] A.Snyder, 'The Effect of Vertex Cuts on CP reach', BaBar Note #177 (1994)

[21] C.Bozzi *et al*, 'The BaBar Silicon Vertex Tracker', Nucl.Inst.Methods **A435**, 25 (1999)

[22] S.Kluth, 'SVT Hit Resolution', internal document.

[23] The BaBar Collaboration, 'The BaBar Experiment at PEP-II' BaBar Analysis Document #45 (2000)

[24] A.Hocker, Nucl.Inst.Methods **A446**, 310 (2000)

[25] F.Anulli *et al*, Nucl.Inst.Methods **A409**, 542 (1998)

[26] The Trigger Group, 'BaBar Trigger System Design Requirements', internal document (1997)

[27] S.Gehrig, 'Design and Simulated Performance of the Level 1 Trigger System', BaBar Note #380 (1997)

[28] P.D.Dauncey *et al* 'Design and Performance of the Level 1 Calorimeter Trigger for the BaBar Detector', hep-ex/0107062, submitted to IEEE Trans.Nucl.Sci. (2001)

[29] A. Berenyi *et al* 'Design and Implementation of the Level 1 Charged Particle Trigger for the BaBar Detector' IEEE Trans.Nucl.Sci. **46**, 2006-2010 (1998)

[30] R.C.Martin, 'Designing Object Oriented C++ Applications using the Booch Method', Prentice Hall (1995)

[31] G.Booch, 'Object Oriented Analysis and Design' (2nd ed), Addison-Wesley (1994)

[32] R.T.Hamilton *et al*, 'DAQ Programmer's Guide', BaBar Note #386 (1997)

[33] J.Izen & E.Varnes, 'Plain English Introduction to BaBar DAQ', BaBar Note #502 (1999)

[34] J.C.Andress *et al*, 'BaBar Calorimeter Level 1 Trigger Design', internal document (1998)

[35] A.Mass, 'Fast Control Xilinx Users Manual', internal document (1998)

[36] J.C.Andress, 'Level 1 Calorimeter Trigger Energy Selection Processor Algorithm', BaBar Note #508 (1999)

[37] 'GEANT, Detector Description and Simulation Tool', CERN Program Library Long Writeup W5013 (1994)

[38] T.Wenaus *et al*, 'The BBSIM Geant Simulation for BaBar', http://www.slac.stanford.edu/BFROOT/www/Computing/Offline/Simulation/web/bbsim-guide.html

[39] R.Ammer *et al*, 'The Electronic Branching Ratio of the Tau Lepton', Phys.Rev, **D45**, 3976-3985 (1992)

[40] Neutral Identification and Reconstruction Analysis Working Group, BaBar Analysis Document #20 V3 (2000)

[41] J.Olsen, 'Study of high energy π^0s in τ 1-on-1 decays', BaBar Analysis Document #62 V1 (2000)

[42] A.Drescher *et al*, Nucl.Inst.Methods **A237**, 464 (1985)

[43] Electron Identification Analysis Working Group, 'Cut-Based Electron Identification', BaBar Analysis Document #90 V3 (2000)

[44] M.Milek & C.Hearty, 'Lepton Identification Efficiencies and Systematic Errors', BaBar Analysis Document #126 V3 (2001)

[45] D.Azzopardi *et al*, 'Muon Identification in the BaBar Experiment', BaBar Analysis Document #60 V1 (2000)

[46] C.Hearty, 'Initial Analysis of the Performance of the BtamumuSample Muon Control Sample Selector, http://www.slac.stanford.edu/BFROOT/www/Physics/Tools/Pid/Control/Muons/documentation/BtamumuSample.ps.gz

[47] G.De Nardo 'Selection of a Pure Sample of Muons from Radiative Muon Pairs', http://www.slac.stanford.edu/BFROOT/www/Organization/CollabMtgs/1999/physDec99/Thu3/denardo.pdf

[48] D.Thiessen, 'A New MuMuGamma Control Sample', BaBar Analysis Document #268 V1 (2001)

[49] DELPHI Collaboration, 'Measurements of the Tau Leptonic Branching Ratios', CERN-OPEN-2000-030 (1998)

[50] OPAL Collaboration, Z.Phys, **C66**, 543-554 (1995)

[51] CLEO Collaboration, Phys.Rev **D55**, 2559-2576 (1997)

[52] ALEPH Collaboration, Z.Phys, **C70**, 561-578 (1996)

A

Branching Fractions of the τ Lepton

A summary of the measured τ decay branching fractions quoted in [5] of most relevance to the work presented in this thesis is given in table A-1. In the table, h stands for either π or K.

Mode	**Branching Fraction** $\%$
$\tau \to \rho\nu_\tau$	25.40 ± 0.14
$\tau \to e\nu_\tau\nu_e$	17.81 ± 0.06
$\tau \to \mu\nu_\tau\nu_\mu$	17.36 ± 0.06
$\tau \to h \geq 2\pi^0\nu_\tau$	10.73 ± 0.16
$\tau \to h\, 2\pi^0\nu_\tau$	9.36 ± 0.14
$\tau \to h\nu_\tau$	11.79 ± 0.12

Table A-1. *Branching fractions of the τ lepton.*

τ leptons decay directly to either 1 or 3 charged particles in over 99% of τ decays. The topological branching fractions, $\mathcal{B}_n$, where n is the number of charged particles produced directly in the τ decay, are given in table A-2 and are quoted from those listed in [5].

Mode	**Branching Fraction** $\%$
$\mathcal{B}_1$	84.71 ± 0.13
$\mathcal{B}_3$	15.18 ± 0.13
$\mathcal{B}_5$	$(9.9 \pm 0.7) \times 10^{-4}$

Table A-2. *Topological branching fractions of the τ lepton.*

B

Class Diagrams

A description of the application of object oriented software design to software written for the calorimeter trigger was given in chapter 3. The diagrams presented in this chapter to represent the relationships between classes written to implement the calorimeter trigger software design are based on the Unified Modelling Langauge (UML). This is the most common notation used for representing class relationships. An example is shown in figure B-1. In this notation a class is represented by a rectangular box containing the class name

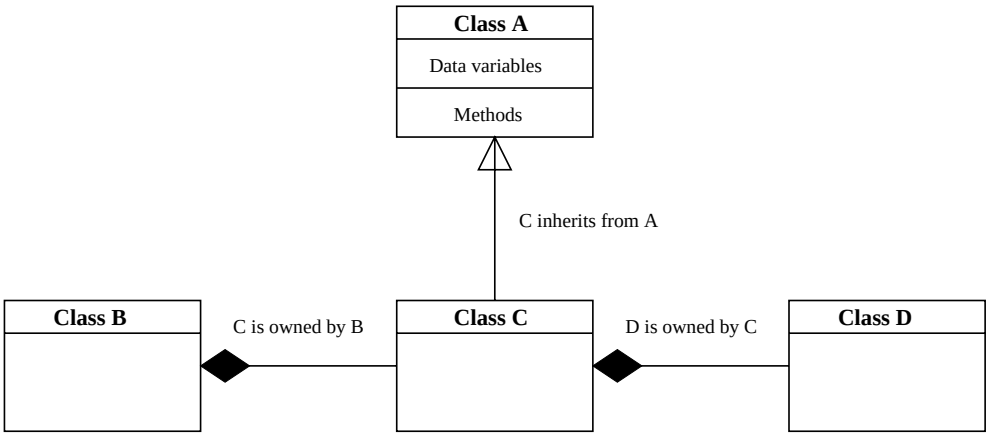

Figure B-1. *Class diagram illustrating the 'inheritance' and 'use' relationships.*

seprated by a line. Often also included in the class box are the class data variables and method names. The relationships between classes are represented by lines connecting the class boxes.

The two types of relationship used by the diagrams presented in this thesis are the ‘inheritance’ relationship and the ‘use’ relationship. Inheritance is a relationship between classes and ’use’ is a relationship between objects defined by the classes. Inheritance is represented by an unfilled arrow, hence class A in the figure is the parent or base class of class C. The use relationship is represented by a filled arrrow in the diagram and represents ownership. In the diagram, the object defined by class B contains, and therefore owns, an object of class C which in turn owns an object of class D.